



**HAL**  
open science

# Effects of thermal cycling and mechanical characterization of an asteroid regolith simulant material

Sébastien Cohoner

► **To cite this version:**

Sébastien Cohoner. Effects of thermal cycling and mechanical characterization of an asteroid regolith simulant material. Mechanics of materials [physics.class-ph]. Université Grenoble Alpes [2020-..], 2023. English. NNT: 2023GRALI099 . tel-04524407

**HAL Id: tel-04524407**

**<https://theses.hal.science/tel-04524407v1>**

Submitted on 28 Mar 2024

**HAL** is a multi-disciplinary open access archive for the deposit and dissemination of scientific research documents, whether they are published or not. The documents may come from teaching and research institutions in France or abroad, or from public or private research centers.

L'archive ouverte pluridisciplinaire **HAL**, est destinée au dépôt et à la diffusion de documents scientifiques de niveau recherche, publiés ou non, émanant des établissements d'enseignement et de recherche français ou étrangers, des laboratoires publics ou privés.

THÈSE

Pour obtenir le grade de

**DOCTEUR DE L'UNIVERSITÉ GRENOBLE ALPES**

École doctorale : I-MEP2 - Ingénierie - Matériaux, Mécanique, Environnement, Energétique, Procédés, Production

Spécialité : 2MGE - Matériaux, Mécanique, Génie civil, Electrochimie

Unité de recherche : Laboratoire Sols, Solides, Structures et Risques

**Effets du cyclage thermique et caractérisation mécanique d'un matériau simulant de régolithe d'astéroïde**

**Effects of thermal cycling and mechanical characterization of an asteroid regolith simulant material**

Présentée par :

**Sébastien COHONER**

Direction de thèse :

**Robert PEYROUX**

CHARGE DE RECHERCHE HDR, Université Grenoble Alpes

Directeur de thèse

**Daniel BRITT**

Co-directeur de thèse

**Barthélémy HARTHONG**

MAITRE DE CONFERENCES, Grenoble INP

Co-encadrant de thèse

**Alice DI DONNA**

MAITRESSE DE CONFERENCES, UNIVERSITE GRENOBLE ALPES

Co-encadrante de thèse

Rapporteurs :

**Thierry CUTARD**

PROFESSEUR, Ecole Nationale Supérieure des Mines d'Albi-Carmaux

**Bertrand WATTRISSE**

PROFESSEUR DES UNIVERSITES, Université de Montpellier

Thèse soutenue publiquement le **11 décembre 2023**, devant le jury composé de :

**Robert PEYROUX**

CHARGE DE RECHERCHE HDR, Université Grenoble Alpes

Directeur de thèse

**Thierry CUTARD**

PROFESSEUR, Ecole Nationale Supérieure des Mines d'Albi-Carmaux

Rapporteur

**Bertrand WATTRISSE**

PROFESSEUR DES UNIVERSITES, Université de Montpellier

Rapporteur

**Pierre BECK**

PROFESSEUR DES UNIVERSITES, Université Grenoble Alpes

Président

Invités :

**Chrysa Avdellidou**

**Britt Daniel**







# Acknowledgments

It's finally time to write this last chapter and put an end to this thesis. It wasn't easy and I would have encountered many twists and turns along the way but I'm happy to say that it's now behind me !

First of all, I would like to thank the members of my jury for agreeing to review my work and for taking the time to guide me to make the last small changes to my PhD thesis, and more particularly Pierre Beck who followed me throughout my PhD and who was kind enough to lend me a superb nitrogen tank after the laboratory fire.

Then, I want to thank my supervisors, Robert Peyroux, for allowing me to sign my contract (which was not easy), and to bring this project to fruition, Alice DiDonna who trained me in the use of the wire saw, and finally Barthélémy Harthong for these hours of coffee breaks to remake the world and especially for his unfailing support, even when I was doing pignouf work !

I would also like to thank Dan and Judith Britt for this great international experience, as well as Karl, with whom we explored Florida and the great smoky mountains, and without whom this American trip would not have been the same.

I was also lucky to have a great intern, who helped me a lot so thank you very much Salman for all this work.

I don't forget to thank Jérôme, Pascal and all those without whom I would not have been able to carry out this work.

Obviously, this experience would have been very different without all my colleagues who have often helped me, put up with me and listened to me complain all this time. You have made these

---

4 long years unforgettable! Thank you to all of you, Clara, Emilie, Josselin, Camille, Quentin, Nils, Antoine, Sophie, Stéphane, François, Bart (I know I've already mentioned you above but I'm also giving you back here), Romain, Pauline, Marilyn, Julia, Thanos... And I hope I haven't forgotten anyone, but if I have, thank you also to those I forgot !

Finally, I can't conclude without thanking Laurie, who became my wife during this adventure and who followed me during my stay in Orlando. Thank you for being there for me all this time. I couldn't have done it without you.

And never forget !

*"Il ne faut jamais oublier de prendre du plaisir dans tout ce qu'on fait !"*

Lilifan, Peepodo Season 1 : episode 2 : Basketball



# Contents

<b>Acknowledgments</b> . . . . .	4
<b>Introduction</b> . . . . .	11
<b>1 State of the art</b> . . . . .	<b>15</b>
<b>1.1 Solar system formation</b> . . . . .	17
<b>1.1.1 Early processes of the Solar System</b> . . . . .	17
<b>1.1.2 Birth of asteroids, comets and planets</b> . . . . .	19
<b>1.2 Comets and asteroids : witnesses of the early solar system</b> . . . . .	21
<b>1.2.1 Comets</b> . . . . .	21
<b>1.2.2 Asteroids</b> . . . . .	22
<b>1.3 Regolith</b> . . . . .	24
<b>1.4 Meteorites</b> . . . . .	26
<b>1.4.1 Classification</b> . . . . .	26
<b>1.4.2 Composition of CM chondrite</b> . . . . .	29
<b>1.4.3 Physical properties of CM chondrite</b> . . . . .	29
<b>1.4.3.1 Thermal properties</b> . . . . .	30
<b>1.4.3.2 Mechanical properties</b> . . . . .	34
<b>1.5 Simulant</b> . . . . .	40
<b>1.6 Physical properties of the regolith</b> . . . . .	44
<b>1.6.1 Thermal behavior</b> . . . . .	44



1.6.2	Mechanical behavior	45
1.7	Outlines and goals of the thesis	49
<b>2</b>	<b>Mechanical tests</b>	<b>50</b>
2.1	Samples preparation	52
2.1.1	Preparation of the material	52
2.1.2	Preparation of the samples	56
	Samples for Young's modulus characterization	57
	Samples for tensile strength characterization	57
	Additional methods tested to shape samples	60
2.2	Young's modulus characterization	62
2.2.1	Methods	62
	Experiment	62
	Samples	64
2.2.2	Results	65
2.3	Measurement of the uniaxial tensile strength	71
2.3.1	Methods	71
	Experiment	71
	Samples	72
2.3.2	Results	73
2.4	Compression tests	75
2.4.1	Methods	75
	Experiment	75
	Samples	76
2.4.2	Results	78
2.5	Conclusion	82

---

<b>3 Thermal cycling</b>	<b>85</b>
<b>3.1 Methods</b>	87
<b>3.1.1 Thermal cycles on asteroids</b>	87
<b>3.1.2 Experimental set up</b>	89
<b>3.1.3 Experimental design</b>	93
<b>3.1.4 Samples preparation</b>	95
<b>3.1.5 Image analysis</b>	97
<b>3.2 Results</b>	103
<b>3.3 Conclusion</b>	115
<b>4 General conclusion</b>	<b>116</b>
<b>Recommendations</b>	<b>118</b>
<b>Bibliography</b>	<b>124</b>
<b>Appendices</b>	<b>126</b>
<b>4.1 Appendix to Chapter 2</b>	127
<b>4.1.1 Drawing of the different molds used</b>	127
<b>4.1.2 History of the various tests carried out</b>	127
<b>4.2 Appendix to Chapter 3</b>	132
<b>4.2.1 Thermal simulation parameters</b>	132
<b>4.2.2 SPAM code and parameters</b>	132
<b>Abstract for the Lunar and Planetary Science Conference (LPSC) 2022</b>	133
<b>4.3 Abstract</b>	136

---



# Introduction

Asteroids are small celestial bodies often of irregular shapes orbiting around the sun. They are mainly found in the asteroid belt which lies between Mars and Jupiter. It is believed that these asteroids are the remnants of a planet that could not finalize its formation following the birth of Jupiter. Unlike planets, some asteroids have suffered little alteration due to volcanic or geochemical activities and have therefore retained their pristine nature since the beginning of the formation of the solar system. The study of these so-called primitive asteroids could therefore provide a wealth of information on the origins of the solar system 4.6 billion years ago. In recent years, the flybys of various space probes, as well as dedicated missions such as Hayabusa 2 of the Japan Aerospace Exploration Agency ([JAXA](#)) on the asteroid (162173) Ryugu, which brought back some dust from Ryugu's surface or OSIRIS-REx from NASA on (101955) Bennu which is expected to be back on Earth with a similar sample of asteroidal rock in 2024, have been completed. These missions made it possible to obtain images and samples showing that the surface of these asteroids was cratered and covered with rocks of various sizes as well as a layer of dust known as regolith. Impacts of micrometeorites ([Hogan et al., 2015](#); [Yamada et al., 2016](#); [Avdellidou et al., 2019b](#)) and thermal fracturing triggered by day/night temperature variations ([Delbo et al., 2014](#); [Hazeli et al., 2018](#); [Mir et al., 2019](#); [Molaro et al., 2020](#)) are the two hypotheses put forward to explain the formation of the regolith.

Among all the asteroids, the so-called near-Earth asteroids are those which were deflected from their orbit following an impact. They therefore pass closer to Earth's orbit and are potentially dangerous.

The materials that constitute most of the near-Earth asteroids are believed to be very weak, common in space but almost nonexistent on Earth (Walsh, 2018; Grott et al., 2019; Popova et al., 2011).

The study of these materials represents important issues on several levels:

- The better understanding of the early stages of our solar system in particular the nature of primitive materials and the processes they passed through;
- A better interpretation of the data collected by space probes using optical / imaging techniques;
- The design of rovers aimed at navigating on this material;
- The protection of the planet in the event of a possible impact or the redirection of an asteroid as for the NASA's mission DART (Double Asteroid Redirection Test);
- The possible use of this material for different purposes (industrial, building material, etc.).

In order to answer these questions, various laboratories have embarked on the manufacture of simulant materials. The Exolith laboratory at university of central Florida (UCF) has developed similar regoliths for different types of asteroids (Britt et al., 2019). An international collaboration between the Exolith laboratory and the 3SR laboratory in Grenoble, France has therefore been launched with several objectives:

- Evaluate the possibility of regolith formation through progressive fracture of rock caused by day/night temperature variations;
- Characterize and control the mechanical behavior of the simulant material;
- Develop methods to improve the reliability of tests on this material.

It is in this context that this PhD thesis was born. To achieve these objectives, original experiments had to be developed in order to best adapt to this particularly weak and fragile material.

To meet these objectives, this manuscript will be divided into 3 chapters :

- Chapter 1: The state of the art presents a summary of the main known phenomena from the creation of the solar system to the present day that have had an impact on the creation and life of asteroids. The differences between asteroids and meteorites are discussed with a focus on their main characteristics and classifications. Finally, the motivations and challenges of this study are detailed.
- Chapter 2: The mechanical study of the material begins with the presentation of the sample shaping process. The methods used for the various tensile and compression tests are then presented as well as their results.
- Chapter 3: The thermo-mechanical study focuses on thermal cycling and monitoring the evolution of the material during these cycles by X-ray tomography. A study of these images by digital image correlation is then presented.

The manuscript ends with a discussion of the results obtained and a conclusion, followed by an opening for possible future projects.



# Chapter 1

## State of the art

*The study presented in this document focuses on CM-type asteroids which are so-called "primitive" asteroids. In order to study asteroids, it is first important to understand how they were formed and the processes they went through from their birth to the present day. For that, we have to go back to the first hours of our solar system.*

*In this chapter, the major steps in the creation of our solar system will be discussed. The major differences between asteroids and comets, which are two primitive bodies, will be presented. The differences between asteroids and meteorites, as well as classification methods and studies on the physical characteristics of the latter will be detailed. Finally, the study of the regolith, as well as its stakes will be discussed.*



Contents

---

<b>1.1 Solar system formation</b>	17
1.1.1 Early processes of the Solar System	17
1.1.2 Birth of asteroids, comets and planets	19
<b>1.2 Comets and asteroids : witnesses of the early solar system</b>	21
1.2.1 Comets	21
1.2.2 Asteroids	22
<b>1.3 Regolith</b>	24
<b>1.4 Meteorites</b>	26
1.4.1 Classification	26
1.4.2 Composition of CM chondrite	29
1.4.3 Physical properties of CM chondrite	29
1.4.3.1 Thermal properties	30
1.4.3.2 Mechanical properties	34
<b>1.5 Simulant</b>	40
<b>1.6 Physical properties of the regolith</b>	44
1.6.1 Thermal behavior	44
1.6.2 Mechanical behavior	45
<b>1.7 Outlines and goals of the thesis</b>	49

---

## 1.1 Solar system formation

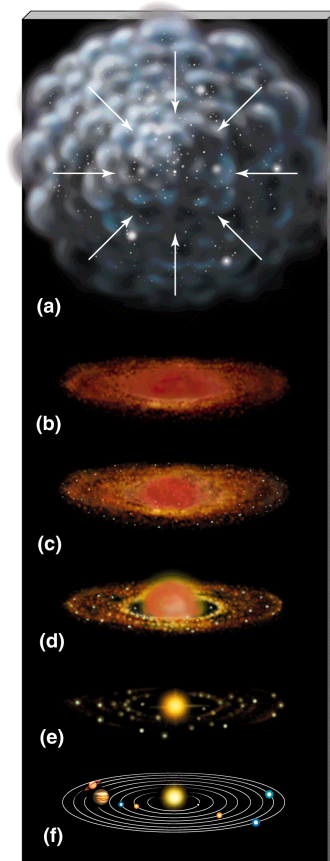
### 1.1.1 Early processes of the Solar System

It all started 4.6 billion years ago (Bouvier and Wadhwa, 2010). At this stage, the solar system as we know it did not exist. Several theories try to explain how it was formed (Woolfson, 2000). Although many questions remain unanswered, the most commonly accepted model is the Solar Nebular Disk Model (Figure 1.1) (SNDM). A giant cloud of gas and dust known as a solar nebula collapsed under its own gravity (Figure 1.1 (a)) (Cameron, 1962). It is likely that the shock wave produced by a nearby super nova is the phenomenon that triggered this collapse (Cameron and Truran, 1977). As a result of the collapse, the solar nebula spun faster and faster and flattened into a protoplanetary disk (Figure 1.1 (b)). Most of the materials was then attracted toward the center of this disk of gas and started to warm up and create a protostar (Williams and Cieza, 2011) (Figure 1.1 (c)). During the next 50 million years, the protostar evolved into a pre-star called T Tauri star, the temperature and the pressure in its core rised, until the conditions to start the fusion of hydrogen were reached (Caffe et al., 1987). The Sun was born.

That was during this warm and hectic period that the first materials of the solar System started to form primordial aggregates inside the disk plane such as Interplanetary Dust Particles (IDPs). These are small particles of less than a hundred micrometers. Different materials can be found in these IDPs like for example silicate minerals, metal, sulfides and carbonaceous material. Due to the action of various heat sources, those particles were melted and finally solidified later becoming the firsts surviving solar solids. These solids are still present today and can be found on Earth in the form of meteorite. It is on the latter that a large number of studies have focused on the dating of these primitive materials using different methods (U235/Pb207system, the Pb-Pb ages, Al chronometer,...) (MacPherson and Russell, 1997; Amelin et al., 2002; MacPherson, 2003). In 2010, a Ca and Al-rich refractory inclusion (CAI) has been dated at least 4,568.2 million years ago (Bouvier and Wadhwa, 2010) which makes it the oldest processed material

conserved from the creation of the Solar System.

Figure 1.1: Stages of Star System Formation : (a) The nebula cloud starts to collapse due to gravity, (b) the nebula begins to rotate and flattens into a disk, (c) creation of a protostar, (d) planetesimal appears, (e) planets begin to form, (f) our solar system (Lifeng, [2021](#))



Other solid materials have been melted down from the gas phase such as chondrules which are small, almost round sub-millimeter Mg-Fe silicate beads, and which are one of the main components found in most primitive meteorites. The composition of [CAIs](#) ( $^{16}\text{O}$ -rich) and chondrules ( $^{16}\text{O}$ -poor) tends to suggest that [CAIs](#) have been formed before chondrules, according to the generally accepted hypothesis that the nebula became more  $^{16}\text{O}$ -poor as the time went by (Krot et al., [2005](#)). It has been computed that the chondrule formation started 1 to 5 million

years after CAIs formation, in a time when the protosun was accreting at a slower rate (Kita et al., 2005; Krot et al., 2005).

Chondrules and refractory inclusions were then compacted together with fine-grained dust available within the protoplanetary disk, including ancient interstellar grains, to become the precursors of larger bodies (Jones et al., 2000; Brownlee et al., 2006). Some authors assume that these materials could have reached distances far enough to be included in the formation of comets (Ogliore et al., 2012). This combination of crystalline components (CAIs and chondrules), grains of metal and chromite, sulfides, and a fine-grained amorphous material (usually forming the matrix), is what can be found today in undifferentiated primitive meteorites such as chondrites (Moyano-Camero et al., 2017).

### 1.1.2 Birth of asteroids, comets and planets

Planetary formation begins with the accretion of these primordial materials. Experimental studies have demonstrated that this process took place in a relatively short timescale (Blum et al., 2006). These bodies were formed by the relatively fast agglomeration of dust and ice through low speed inelastic collisions below 1 m/s, combined with adhesive surface forces (Weidenschilling, 1993) forming larger particles (on the order of a centimeter) in a few thousand years. As the bodies grew in size and mass, the velocities and impact energies increased too which resulted in compaction of the dust aggregates (Blum and Wurm, 2000).

Slowly, these aggregates evolved into bigger ones until they reached a kilometric size. We call them planetesimals (Figure 1.1 (d)). They continued to grow by accreting all the material on their way. At the end of this process, they could reach thousands of kilometers of diameter and become planets (Figure 1.1 (e)). Some other objects stopped their growth sooner. Their ultimate sizes reached between a few meters and hundreds of kilometers. These are the small bodies of our solar system, asteroids and comets.

These small bodies, as well as the bigger ones like planets, have suffered more or less modifications since their formation. Planets, and also the bigger asteroids, underwent structural

changes forming layers of different densities. This phenomenon called differentiation was caused by energy sources like impacts or gravitational pressure leading to temperature increase until the materials melt. The heaviest materials (iron, nickel,...) tended to sink toward the center of the body while the lightest ones (organic components, silicates,...) were more likely to migrate toward the surface like on Earth.

For asteroids, the gravitational pressure was too weak to activate this process. The main sources of energy were then coming from impacts and short-lived radioactive nuclei decay. The differentiation process led to a modification of the overall structure and materials constituting bodies. Therefore, differentiated asteroids cannot be considered as primitive asteroids.

However, the major part of the small bodies of the solar system are not differentiated. The study of these primitive bodies provides information on the first solid materials, which makes it possible to date and better understand the first stages of the evolution of the primitive solar system, and the formation of the first constitutive elements of the planets. They are witnesses of the early solar system (Moyano-Camero et al., 2017).

## 1.2 Comets and asteroids : witnesses of the early solar system

### 1.2.1 Comets

Comets are part of the most primitive bodies of the solar system. They were formed in the outer part of the solar system where the temperature was below 30 K. Their small size added to the low temperature resulted in a limited thermal alteration.

There are two main reservoirs where comets come from. The first is the Kuiper Belt which lies just beyond Neptune's orbit between 30 and 60 AU. This is where the so-called periodic or short-period comets come from. Their revolution period is approximately 20 years for comets of the Jupiter family and between 20 to 200 years for comets of the Halley family. Sometimes gravitational interactions due to the surrounding giant planets can deviate these comets from their path and direct them towards the inner Solar System. They then take a tighter elliptical path with a shorter orbital period bringing them closer to the sun. Among the best-known short-period comets, we can cite comet Wild 2 from which some samples were returned during the Stardust space mission in 2006, as well as comet 67P / CG visited by the Rosetta probe in 2007.

The second reservoir is the Oort cloud which has never been observed directly. It is by studying the trajectory described by long-period comets that Oort predicted its existence in 1950. It ranges approximately from 30,000 AU up to over 100,000 AU and is considered to be the outer limit of the external Solar System.

Comets are small bodies of a few kilometers in diameter. They are made up of dust and ice, mainly water. When passing close to the sun (1 to 3 AU), comets are heated by solar radiation. This has the effect of sublimating the ice and liberating grains of dust thus forming what is called a coma (or hair), a tail of dust and ions. This is called cometary activity. During these multiple passages, the presence of volatile elements decreases until they are too few. The comet then becomes inactive (Battandier, [2018](#)).

### 1.2.2 Asteroids

Asteroids are also small celestial bodies. Their shape can vary from a few meters of diameter to hundreds of kilometers. Most known asteroids orbit in the main belt between Mars and Jupiter, between approximately 2 and 5 AU. The birth of Jupiter, which is the biggest planet of our solar system, prevented any planetary bodies from forming in the gap between Mars and Jupiter. This explains why the small objects that were there started to collide with each other and fragmented into the asteroid belt that we can see nowadays. A second group is found between the Sun and Mars, they are called "Near-Earth Asteroids". This group is most likely formed by asteroid debris ejected from the main belt because of collisions. They are potentially dangerous because their proximity to the Earth makes the risk of impact not unlikely. There are also two other types of asteroids. The group of Centaurs which is located between Jupiter and Neptune and the Trojans which are located at the Lagrange points of Jupiter.

Contrary to comets, asteroids are inactive due to the fact that they are less rich in volatile elements and ice. However this distinction is more and more questioned with the discovery of several asteroids showing cometary activity like Bennu visited by the OSIRIS-REX mission of the NASA (Lauretta et al., [2019](#)).

The composition of asteroids can vary a lot. A first taxonomy was created by Chapman in 1975, using different optical criteria such as albedo, color or spectral slope, which is a curve showing the evolution of the reflectance in function of the wave length, in order to classify asteroids into different categories. However, this classification takes little account of their composition. This taxonomy consists in a classification of asteroids into 3 different major families as following :

C : Also called carbonaceous, they are dark asteroids with low albedo (0.03 to 0.10) and are mainly composed of carbon and silicate. This is the most common variety, forming around 75% of known asteroids (ex : 1 Ceres, 10 Hygiea).

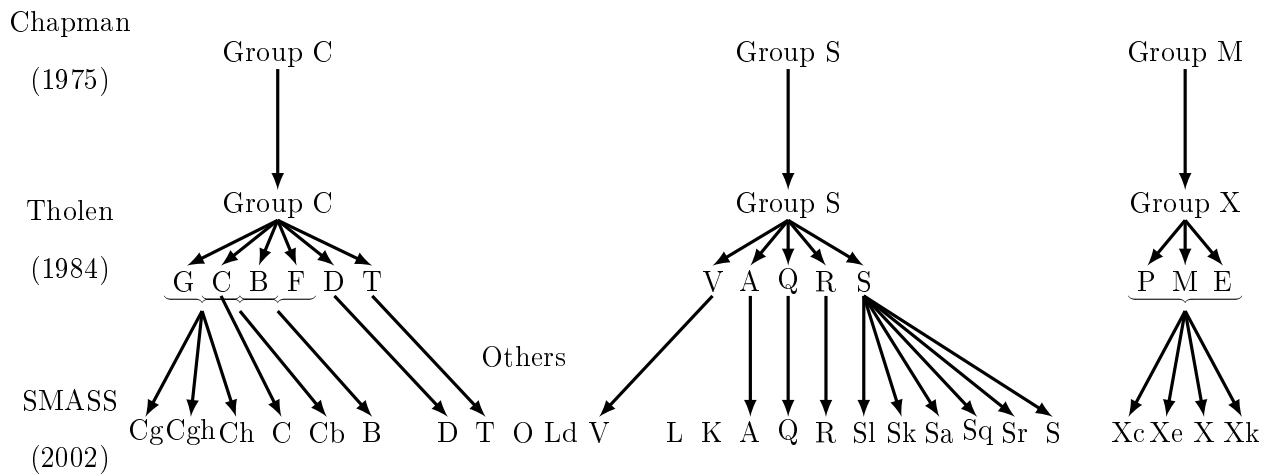
S : Also called stony, are also composed of silicate but without carbon, which explains why they are brighter with an albedo of 0.2. Approximately 17% of asteroids are of this type (ex : 3

Juno, 15 Eunomia).

M : They are metallic asteroids and are the less studied. They represent only 8% of asteroids with an albedo between 0.1 and 0.2 (ex : 16 Psyche, 21 Lutetia).

With scientific advances, more accurate measurement lead to new classifications. The most commonly used taxonomies are the one proposed by Tholen in 1984 with 14 categories and the one proposed by Bus & Binzel in 2002 (SMASS) with 26. However, most of these categories are subgroups of those of Chapman's classification.

Figure 1.2: Comparison of the Chapman, Tholen and SMASS taxonomies

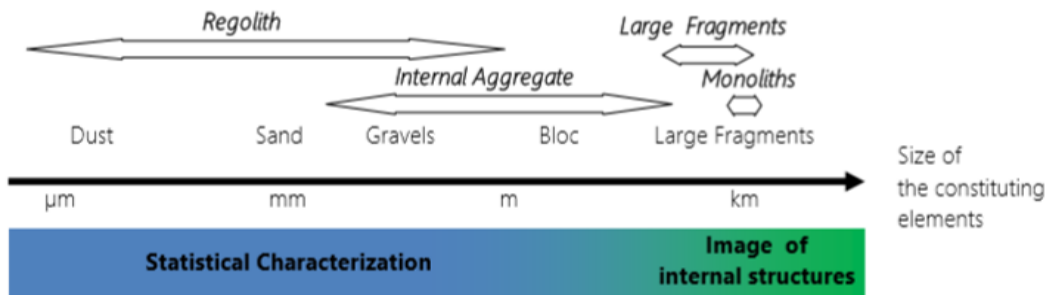




### 1.3 Regolith

The center of an asteroid can either be a monolith, or an assembly of large fragments (Figure 1.3) (Britt et al., 2010). Those large fragments come from collisions between two asteroids. They grouped together as an effect of gravitational forces and created what we call a Rubble Pile Asteroid (Walsh, 2018). Between this central section and the surface, diverse internal aggregates can be found. A layer of dust and gravels, more or less homogeneous depending on the asteroid, covers the surface of the asteroid. This layer is called regolith (see Figure 1.4).

Figure 1.3: Asteroid structures and size distribution (Hérique et al., 2018)

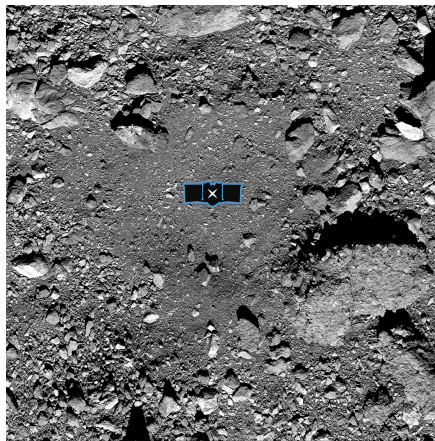


The mechanisms responsible for the creation of regolith are not yet fully understood. Indeed we still do not know how the rocks composing the asteroid turned into thin dust. To explain this phenomena, two hypotheses are put forward. The first and oldest one says that the regolith would be created by hyper-velocity impacts from micrometeorite bombardment (Marcus, 1973; Ashworth, 1978; Yamada et al., 2016; Campbell-Brown, 2019) but this assumption is increasingly questioned (Hazeli et al., 2018). Indeed the typical impact speed in the Main Belt is around  $5 \text{ km.s}^{-1}$  (Bottke Jr et al., 1994). At this speed, the ejecta produced during the impact are projected and only a small quantity of this material falls back to the surface of the asteroid because of its weak gravitational force. The second hypothesis states that space weathering could have a major impact on the regolith formation. Indeed, the strong temperature variations suffered by the asteroid during the day / night cycle can go up to  $\Delta T = 200 \text{ K}$ . (Delbo et al., 2014;

Hazeli et al., [2018](#))

Understanding the surface of asteroids is very important since most of the knowledge that we have on asteroids come from optical measurement of the solar light reflected by the surface of the asteroid. In addition, this knowledge is greatly useful for rover design. Finally we could also add the Earth defense against asteroids impacts and the asteroid mining, which is more and more studied (Ursul and Ursul, [2019](#); Dallas et al., [2020](#)), as well as the idea to use regolith as a building material for the project of the Moonbase, (Meurisse et al., [2018](#)).

Figure 1.4: Image of the regolith on the sample-collection site ‘Nightingale’ with a silhouette of the OSIRIS-REx spacecraft (Image Credit: NASA/Goddard/University of Arizona)

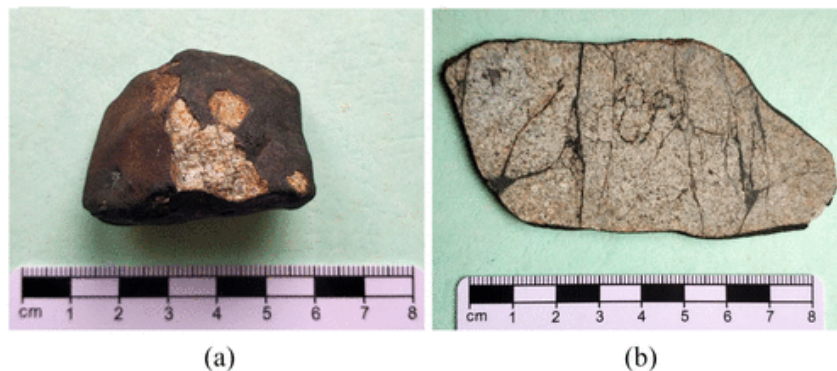


Due to the lack of material at our disposal on Earth, most studies on regolith are based on experiments and observations on meteorites.

## 1.4 Meteorites

Meteorites are natural objects of extraterrestrial origin reaching the Earth's surface. They can be of various sizes ranging from millimeters to tens of meters. The majority of them come from asteroids but meteorites can also be fragments coming from the Moon or even Mars. They were detached from the surface by an impact big enough to project them out of the gravitational field of the body they belonged to. Most of collected meteorites are "finds", which means that the time they spent on Earth is unknown. However, some meteorites are found after the observation of their fall. These meteorites are very interesting because although they have undergone alterations due to their entry into the atmosphere, they have not been impacted by prolonged exposure to terrestrial conditions. Meteorites are easy to identify. Their dark color due to the high temperature reached when they entered the atmosphere (Figure 1.5) as well as their high density are characteristic.

Figure 1.5: (a) The Viñales specimen (L6 chondrite) has a black fusion crust and the interior lithology show gray color. b) A piece of Viñales meteorite is interspersed by many black shock veins. (Yin and Dai, 2021)

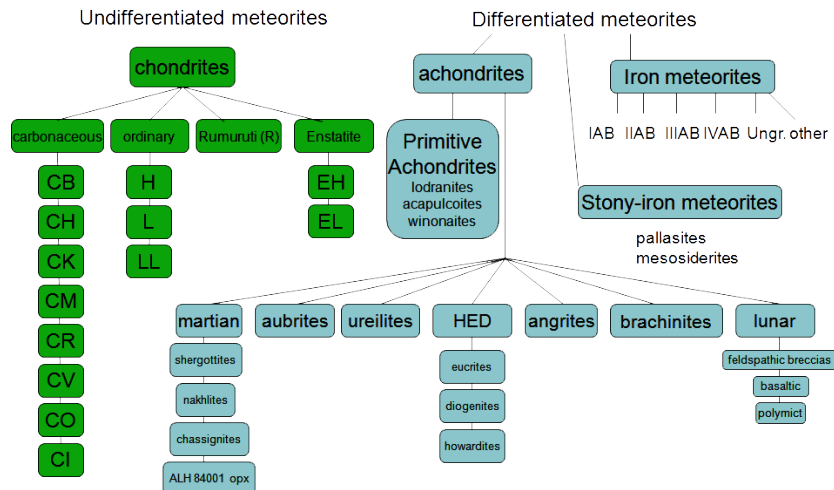


### 1.4.1 Classification

Meteorites can be very different from one to another. For this reason, the following classification was made in order to distinguish each type (Figure 1.6). We can see that meteorites are separated

into two large families : the differentiated meteorites, coming from differentiated bodies like planets or some meteorites, and the undifferentiated ones called chondrites.

Figure 1.6: Primary classification of meteorites (NASA, 2021)



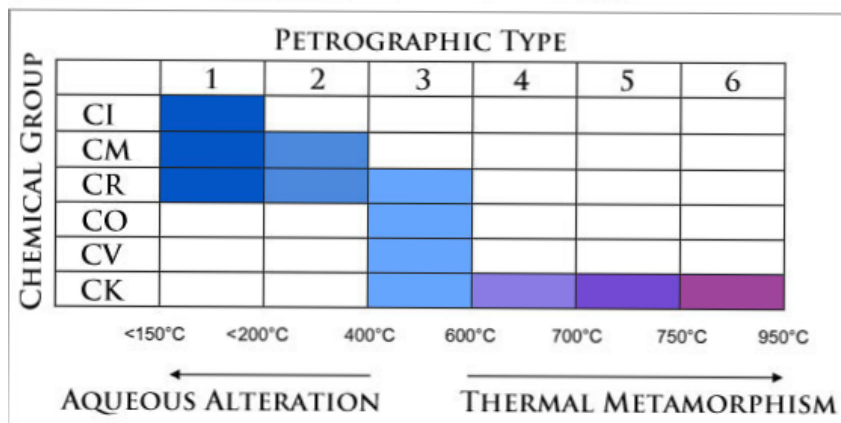
Meteorites originating from differentiated parent bodies are divided into three subgroups. The first one is the achondrite group which can be divided in two categories : the primitive achondrites, which are meteorites partially differentiated and achondrites which come from the crust of differentiated parent bodies. The second one is the iron meteorites, coming from the core of differentiated parent bodies and the third one is that of the Stony-iron meteorites.

From now on, we will focus on the most primitive (undifferentiated) meteorites: the chondrites.

The chondrites family can be divided into four groups which will again be separated into several sub-groups. Contrary to the existing classification for asteroids, based on optical criteria, this one is based on petrographic and mineralogical criteria. This is called the primary classification. We therefore find the ordinary chondrites which are the most common ones, the enstatite chondrites, the Rumuruti (R) chondrites and finally the carbonaceous chondrites. The latter are considered to be the most primitive. This is why they are largely studied, even if few samples are available because the carbon chondrites represent only 5% of the chondrites found.

Even if little asteroids did not undergo the phenomenon of differentiation but their original state has still more or less changed due to thermal metamorphism and aqueous alteration (Battandier, 2018). A second classification is based on the degree of alteration of the chondrites (Schmus and Wood, 1967). This classification is said to be secondary. Chondrites are separated into groups ranging from 1 to 6 (Figure 1.7). The third group is the less altered and the further away from 3, the greater the alteration. From 3 to 1, the aqueous alteration increases. It typically leads to the formation of phyllosilicates in greater or lesser abundance possibly associated with carbonates, sulfates and oxides (Zolensky and Jr, 1988). From 3 to 6, the thermal metamorphism increases. It is due to high temperature rise up to 950°C (McSween Jr and Patchen, 1989). This has the effect of homogenizing the different phases present in the chondrite (Schmus and Wood, 1967).

Figure 1.7: Secondary classification of chondrites taking into account the processes on meteorites: from types 3 to types 1, the intensity of the aqueous deterioration increases, from types 3 to types 6, the intensity of thermal metamorphism increases (Taylor, 2011).



As can be seen on Figure 1.7, the two classifications are related since not all the chondrites families suffered the same type and the same degree of alteration.

In what follows, we will mainly focus on carbonaceous chondrites, and more particularly on CM-type carbon chondrites.

### 1.4.2 Composition of CM chondrite

Carbonaceous chondrites are made up of different inclusions embedded into a matrix containing carbon.

The first inclusions that we find are the chondrules which represent 20% by volume, (Jones and Scott, 1996) previously mentioned. These are spheroidal mineral inclusions generally composed of ferromagnesium silicates (olivines and pyroxenes) having formed in the protoplanetary disc, at the very beginning of the formation of the Solar System. They are found in all carbon chondrites except CIs. Their diameter is about 300  $\mu\text{m}$  (Scott and Krot, 2003) in CMs. In CMs carbonaceous chondrites, we also find two kinds of refractory inclusions. The first one is a calcium and aluminum-rich inclusion (CAIs) largely composed of minerals such as spinel, melilite, hibonite, perovskite and Al-Ti-diopside. The second one is an amoeboid olivine aggregate (AOA) made of fine grains of olivine, Fe-Ni and refractory component like aluminum-diopside, anorthite, spinel and rare melilite. The size of these inclusions can go from tens of micrometers to centimeters and the volume percentage is between 0.01 to 10% (Scott and Krot, 2003). The third type of inclusion is Metallic Fe-Ni.

CM carbonaceous chondrites are characterized by an abundant matrix of 70% by volume, (Jones and Scott, 1996). It is mostly composed of phyllosilicates like Fe<sup>3+</sup>-rich serpentine, also called cronstedite. Small olivine grains of 0.1  $\mu\text{m}$ , (Scott and Krot, 2003) rich in magnesium with a composition close to forsterite can also be observed as well as amorphous silicate which represent 15% of the matrix. Presolar components such as olivines and pyroxenes manganese rich called LIME silicate are nebular condensate. Finally, at the matrix rims, aluminum, magnesium, iron and oxygen as well as metallic Fe-Ni and small grains of iron-rich olivine have been observed (Scott and Krot, 2003).

### 1.4.3 Physical properties of CM chondrite

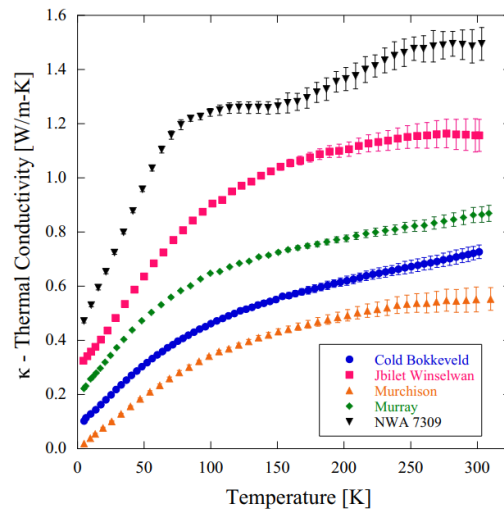
The physical characterization of the material is essential to understand and be able to predict how it will behave under a certain mechanical / thermomechanical loading and to inform numerical

models. Therefore the thermal and mechanical properties of CM chondrites are summarized.

### 1.4.3.1 Thermal properties

The thermal characterization of CM2 carbonaceous chondrites at low temperature (between 5 K and 300 K) have been done in a vacuum environment by Opeil et al. (2020). They measured various thermal characteristics such as the thermal conductivity (Figure 1.8) and thermal expansion coefficient (Figure 1.9) of five different CM2 carbonaceous chondrites. The results vary significantly from one meteorite to another, even from the same family, although we can notice some similarities among three out of the five tested samples. This is the case for the thermal conductivity (Figure 1.8) and for the thermal expansion coefficient (Figure 1.9). The dissimilar behavior of the two other meteorites can be explained by the degrees of alteration suffered on Earth which is different from the three others.

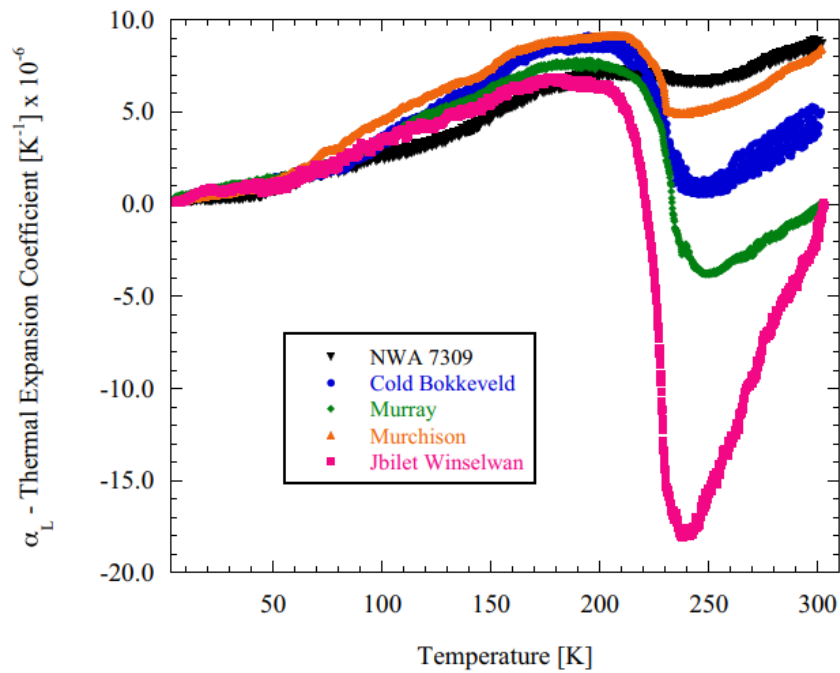
Figure 1.8: Thermal conductivity versus temperature for five CM chondrite samples. Sample dimensions were  $2 \times 3 \times 10$  mm and measured with a cooling rate of  $0.5 \text{ K min}^{-1}$  (Opeil et al., 2020).



During these experiments, Opeil et al. (2020) noticed an unexpected behavior of the thermal expansion coefficient (CTE) of CM2 carbonaceous chondrites (Figure 1.9). From 5 K to about

200 K, we observe monotonic behavior consistent with a composite solid material. However, between 200 K and 240 K, all the samples exhibited a sudden drop of the CTE leading to a negative thermal expansion (NTE) on some samples, followed by a sudden increase between 240 K and 300 K (Opeil et al., 2020).

Figure 1.9: Linear thermal expansion ( $\alpha$ ) versus T measurements indicate a drop of the CTE across a broad T range which occurs for different samples at approximately the same temperature  $235 \pm 1$  K. Measurements shown were taken at a cooling rate of  $0.25 \text{ K min}^{-1}$  on a capacitive dilatometer with a resolution of  $0.8 \text{ \AA}$  ( $8 \times 10^{-11} \text{ m}$ ). Error bars are included and are smaller than the symbols (Opeil et al., 2020).

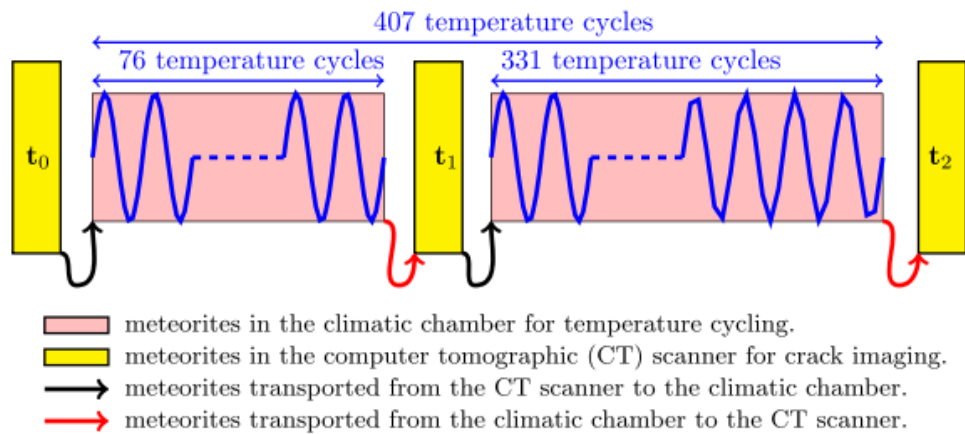


The unusual CTE behavior is most likely due to the huge amount of phyllosilicates present in the CM2 carbonaceous chondrites, created by the aqueous alteration reactions of anhydrous precursor materials. In the case of CM2 chondrites, these phyllosilicates are dominated by serpentine which is a layered silicate mineral. The contraction of such layers is responsible for this behavior of the CM2 meteorites.



These different thermal characteristics between the different phases within asteroids play an important role in the thermal fracturing phenomenon which has been identified as the potential origin of regolith formation on asteroids (Delbo et al., 2014). Indeed, an asteroid can face huge variation of temperature during day/light cycles. The meteorite being made up of different compounds, the mismatch of thermal expansion coefficient between these compounds creates stress concentrations that may lead to the creation and the propagation of cracks through the material. An experiment has been carried out by Delbo et al. (2014) in order to investigate the thermo-mechanical behavior of meteorites (Figure 1.10). These tests were carried out on two different meteorites : Murchison and Sahara 97210, of about 1 cm in size. The samples were CT-scanned before the beginning of the thermal cycling to have the initial state ( $t_0$ ) of the material. Then cycles were performed in a climatic chamber where the air was anhydrous and at a pressure of 1 bar. The air temperature was forced to follow cycles between 250 K and 440 K to have a  $\Delta T = 190$  K which is typical for a C-type NEAs at 0.7 AU from the Sun, with a period of 2.2 h. For this range of temperature, the evolution of the thermal expansion coefficient stays monotonic (1.9).

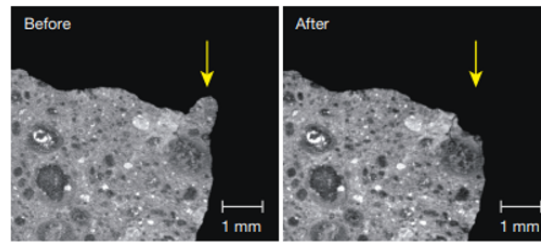
Figure 1.10: Protocol of the thermal fatigue experiments made by Delbo et al. (2014).



The samples were scanned by X-ray tomography again after 76 ( $t_1$ ) and 407 ( $t_2$ ) cycles to see the evolution of the cracks. Cracks were observed after only 407 cycles (Figure 1.11) which

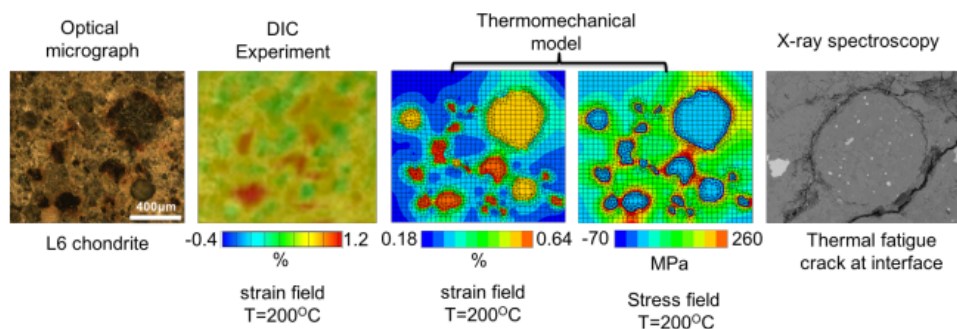
tends to prove that the thermal fatigue can affect CM2 carbonaceous chondrites.

Figure 1.11: Regolith formation from Murchison in the laboratory. Tomographic slices of regions of the same sample of Murchison before and after temperature cycling. The arrows indicate fragments that broke off from Murchison sample (Delbo et al., 2014).



In order to predict and better understand the phenomena playing a role in the thermal fracture of meteorites, a study was carried out, combining experimental work and numerical simulation (Hazeli et al., 2018). The aim of this study was to set up a numerical model capable of predicting the distribution of strains and stresses within the microstructure. To do this an ordinary L6 chondrite was considered. Thermal cycling then took place both numerically and experimentally. The results show that the zones most likely to host a crack start were located around the various inclusions (Figure 1.12).

Figure 1.12: Comparison of experimental results and numerical calculations after the thermal cycling of an L6 meteorite (Hazeli et al., 2018).



This result tends to show the importance of the difference in coefficient of thermal expansion

between the different phases present within the material in the phenomenon of thermal rupture.

### 1.4.3.2 Mechanical properties

The first studies on the mechanical characteristics of meteorites focused on the determination of the density and the porosity of the material.

Bulk density is a measure of the mass of the meteorite divided by its apparent volume which means that the volume of pore spaces inside the rock is included (Equation [1.1](#)). Grain density is the ratio between the mass and the volume of only the solid material (Equation [1.2](#)). Although grain density is more representative of body composition, it is the bulk density that is determined by spacecraft data. Dividing the difference between these two densities by the grain density, provides the porosity (Equation [1.3](#)) as the ratio between the volume of pores and the apparent volume.

$$\rho_{Bulk} = Mass/V_{App} \quad (1.1)$$

$$\rho_{Grain} = Mass/V_{Solid} \quad (1.2)$$

$$Porosity = V_{voids}/V_{App} = (\rho_{Grain} - \rho_{Bulk})/\rho_{Grain} \quad (1.3)$$

In order to determine the porosity of a sample, the measurement of both its bulk and its grain densities are needed. The grain density can be determined using ideal gas pycnometry, which is a technique consisting in measuring a pressure difference in a cell filled with inert gases such as helium, which do not damage the material.

For the bulk density, due to the irregular shape of meteorites, the geometric measurement of the outside volume is more difficult to obtain. In addition, the conventional techniques consisting of immersing a sample in a liquid and measuring the variation in volume is not suitable because this leads to contamination of the material. The Archimedean glass bead method, developed by

Britt and Consolmagno (2000) allows determination of the external volume without damaging or contaminating the sample. This made it possible to carry out a large measurement campaign. The method consists of immersing the sample in small spherical glass beads of 700–800 micrometers diameter. The whole behaving like a fluid, the volume of the material is determined by measuring the volume of the glass beads displaced.

Macke et al. (2011) used the same technique but applied a volume correction in order to reduce a systematic error on the bulk volume due to the method (Macke et al., 2010). Data on 195 carbonaceous chondrites were collected during this survey.

Table 1.1: Bulk density, grain density and porosity of carbonaceous chondrite by meteorite type (Macke et al., 2011).

	Bulk Density ( $\text{g.cm}^{-3}$ )	Grain Density ( $\text{g.cm}^{-3}$ )	Porosity (%)
CI	1.58	2.43	35
CM	2.20	2.92	24.7
CO	3.06	3.48	11.6
CR	3.11	3.42	9.5
CV	3.03	3.54	14.6

Table 1.2: Bulk density, grain density and porosity of carbonaceous chondrite by petrographic type (Macke et al., 2011).

	Bulk Density ( $\text{g.cm}^{-3}$ )	Grain Density ( $\text{g.cm}^{-3}$ )	Porosity (%)
1	1.57	2.42	34.9
2	2.26	2.93	23.1
3	2.9	3.63	21.0
4	3.04	3.58	15.0

The results of this study show a higher porosity of CI and CM type meteorite with respect

to the others kinds. In addition to the type to which the meteorite belongs, its level of metamorphism also plays a role with regard to its porosity. Indeed, Macke et al. (2011) showed that the higher the aqueous metamorphism, the larger the porosity.

The modulus of elasticity, also called Young's modulus is traditionally determined through a tensile test. It is the slope of the linear part of the stress/strain curve (Figure 1.13) that can be computed using Equation 1.4 with  $E$  the Young's modulus,  $\sigma$  the tensile stress and  $\epsilon$  the longitudinal strain.

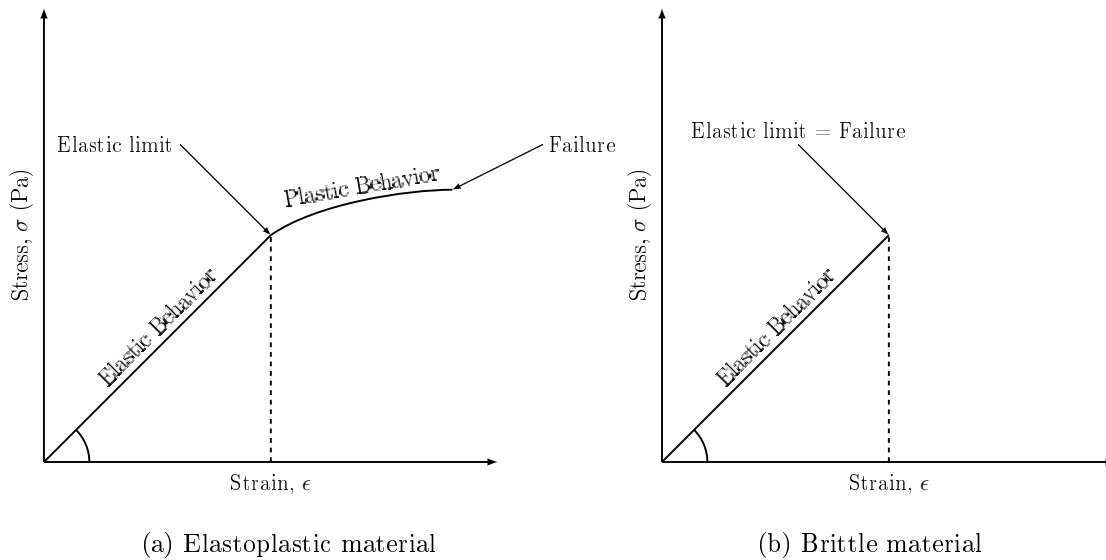


Figure 1.13: Typical schematic Stress/Strain curves of a tensile test

$$E = \sigma/\epsilon \quad (1.4)$$

This linear part represents the elastic behavior of the material, hence its modulus of elasticity. As long as a loading remains in the elastic domain, the material will deform and return to its original shape when the loading ceases, leaving no residual deformation nor damage. For certain fragile materials, there is no plastic behavior and the elastic limit is therefore equal to the failure stress. This is the case for most meteorites.

Although a tensile test is the most common method for determining Young's modulus, it is destructive and therefore difficult to implement on rare materials such as meteorites. That's why Ibrahim (2012) used elastic wave velocity and bulk density values to extract the elastic modulus value, by applying a non-destructive method.

$$E = \rho_{Bulk}/V_E \quad (1.5)$$

$$V_E = 2 \times V_s^2 \times (1 + \nu) \quad (1.6)$$

The Equations 1.5 and 1.6 were therefore used to determine the Young's modulus : where  $\rho_{Bulk}$  is the bulk density,  $V_E$  is calculated from the shear wave velocity  $V_s$ , and the Poisson' ratio  $\nu$ .

By propagating an ultrasonic wave trough a sample with a known length from one end to an other, the shear-wave velocity can be found using easy mathematics (Equation 1.7) with V the velocity, x the sample's length and  $\Delta t$  the time difference between the launch of the ultrasonic wave and its reception.

$$V = x/\Delta t \quad (1.7)$$

The results of this study (showed Table 1.3) are consistent with the results found previously by Macke et al. (2011) because they show an increase in the modulus of elasticity for the categories of meteorites having the lowest level of porosity.

Table 1.3: Poisson' ratio and Young's modulus of carbonaceous chondrite by meteorite type (Ibrahim (2012))

	$\nu$	E (GPa)
CM	0.155	11.8
CO	0.16	16.2
CR	0.165	22.0
CV	0.13	25.3

To determine the tensile strength in tension as well as in compression, there is no choice but to use destructive methods. Miura et al. (2008) performed compressive tests on Murchison meteorites (CM2). Cylindrical shaped samples in sizes of 5 mm in diameter and 10 mm in length were made and placed between two compression plates where a constant displacement of 1 micron/sec was imposed. The compressive strength was determined as the point of the maximum stress before the failure of the sample. Several tests were realized and showed highly reproducible results. The obtained compressive strength was 50 MPa.

To determine the tensile strength, meteorites were crushed to obtain small fragments of about 100 microns. Compression tests were then carried out and the tensile strength was determined with Equation 1.8.

$$\sigma_{Tension} = 0.9 \times F_{Failure} / Thickness^2 \quad (1.8)$$

This is based, like the Brazilian tests, on the fact that during a compression test, a vertical crack due to horizontal tensile stresses reaching the tensile strength appears in this zone. This method was developed by Hiramatsu and Oka (1966) in order to test the mechanical characteristics of irregularly shaped rocks. Although not very accurate, in particular because of the difficulty in determining the section on this type of irregular samples or the size of the grains being too small to be able to be considered as being homogeneous, it nevertheless allows to have

a first idea of the tensile strength of the material. An average tensile strength of  $2.0 \pm 1.5$  MPa was obtained for the CM-type meteorites (Tsuchiyama et al., 2008).



## 1.5 Simulant

The lack of asteroids samples on Earth represents a major obstacle to the study of regolith. Indeed, when entering the atmosphere, the asteroids begin to burn up. Smaller objects are not able to reach the ground. They overheat and explode in the sky. Objects of larger dimensions, or made of denser materials such as iron asteroids, manage not to burn up entirely. This remaining part land on earth and become a meteorite. The regolith being the material resting on the surface of these objects, it is also the first to burn up when entering the atmosphere. The only real asteroid's regolith samples present on Earth have therefore been brought back during space missions and are difficult to access, particularly to carry out destructive tests.

For this reason, for a long time, the mechanical data we acquired on asteroids came from tests carried out on meteorites. However, by studying asteroids during their fall, it has been shown that the first ruptures observed during the entry into the atmosphere of asteroids took place at stress levels well below what could be measured on a meteorite from this same asteroid once on earth (Popova et al., 2011). In this study, the bulk strength of the asteroid is estimated by computing the pressure applied by the atmosphere on the asteroid at the time of its fragmentation (1.9).

$$P = \rho_h V_h^2 \tag{1.9}$$

With  $P$  the pressure,  $\rho_h$  the atmospheric density at the fragmentation height  $h$  and  $V_h$  the velocity of the asteroid at that height.

These differences in mechanical characteristics between asteroids and meteorites can be explained by the fact that the meteorite only represents the hardest part of the asteroid and is therefore not necessarily representative of its overall mechanical behavior. In addition, the strong heat and the compaction undergone when entering the atmosphere probably trigger structural changes which could also explain these differences. In the same study, the stress at which the first breakup was observed has been measured between 0.1 and 1 MPa and maximal strength on

breakup as 1–10 MPa whereas measured average tensile strength of the similar meteorite classes is about 30 MPa (Popova et al., 2011).

In order to study asteroids more precisely, several laboratories have started designing materials capable of simulating the characteristics of regolith in order to overcome these limitations (Figure 1.14).

Figure 1.14: CM simulant based on the Murchison meteorite (Britt et al., 2019).



The Exolith lab from UCF developed a material simulating the characteristics of the regolith of several objects such as the moon, Mars and CM asteroids (Figure 1.14). This simulant was built up based as faithfully as possible on the mineralogy observed on CM-type meteorites (Table 1.4).

Table 1.4: Mineralogy of the Murchison meteorite (CM2) and the CM Carbonaceous Chondrite Simulant (both given as wt%). (Britt et al., 2019)

	Murchison (CM2)	CM Carbonaceous Asteroid Simulant
Mg-rich serpentine	22.8	72.5
Fe-rich serpentine	58.5	0
Magnetite	0.4	10.4
Olivine	11.6	7.8
Coal (sub-bit.)	0	3.6
Pyrite	0	2.6
Pyroxene	2.2	2.1
Siderite	0	1.0
Fe-sulfide	3.4	0
Calcite	0.1	0

Although the composition of the simulant is close to that of CM meteorites, there are a number of differences. Fe-rich serpentine (cronstedtite) is abundant in CMs but extremely rare on Earth. It does not occur in massive deposits, but is typically in small nodules in sulfide deposits. The other problem is that cronstedtite is an accessory mineral in uraninite and pitchblende (radium ore) deposits. The result is that mine sources of cronstedtite are extremely limited and highly controlled. That is the reason why cronstedtite has been replaced by Mg-rich serpentine in the simulant. As a result of this change, the simulant tend to be Fe-poor. To solve this problem, the wt% of magnetite has been sightly increased and the siderite was added to introduce a carbonate with iron. The troilite is also rare on earth, that is why it has been substituted by pyrite. Finally, coal was added to include organics similar to carbonaceous organics but without toxicity (unlike many carbonaceous organics).

The simulants are made in powder form (Figure 1.14) but it is possible to agglomerate them

into cobbles (Figure 1.15b). To do this, the simulant base powder is simply mixed up with water to create a malleable paste (Figure 1.15a). The serpentine reacts to the water and is responsible for most of the strength of the simulant. While this is enough for CIs, stronger asteroids like CMs need sodium metasilicate to be added in order to create an alkali-activated material which will increase the strength of the cobble (Britt et al., 2019). After mixing, the mixture is dried up for 24 hours in an oven at 75°C.



(a) Paste made from combining the simulant with water



(b) Dried and crushed cobbles

Figure 1.15: Cobble formation with powder simulant (Britt et al., 2019)

However, the realization of this material raises several questions. How reproducible is the process? What is the influence of atmospheric conditions? Is there residual water within the material? Several laboratories offer simulating materials, using different recipes. What is the influence of these differences?

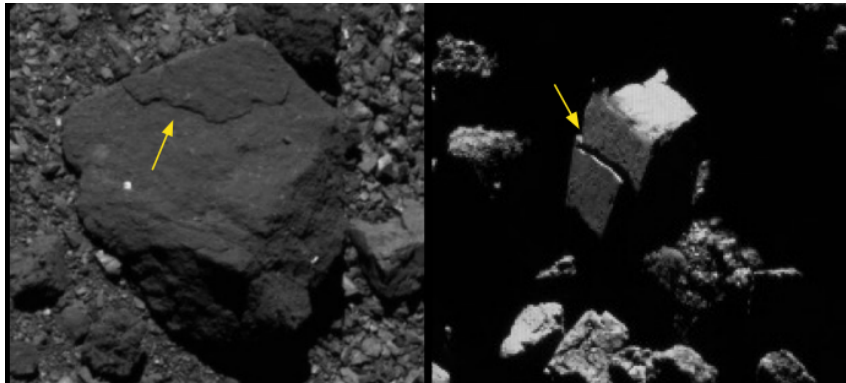
## 1.6 Physical properties of the regolith

In this section, the various studies presented are based on observations made directly on asteroids or on the simulating material discussed in the previous section.

### 1.6.1 Thermal behavior

Recently, thanks to the OSIRIS-REx mission from the NASA, photographs from the surface of the asteroids 101955 Bennu showed images of rock failure strongly resembling to thermally induced cracks (Molaro et al., 2020) for the first time (Figure 1.16). For the author, this discovery tends to confirm the hypothesis of the formation of regolith due to diurnal thermal cycling.

Figure 1.16: Exfoliation features observed on Bennu (Molaro et al., 2020)



In order to study this hypothesis, the thermal characteristics of the regolith have to be known. First tests have been carried out to determine the thermal conductivity using the hot wire technique (Avdellidou et al., 2020). To do this, the simulant of a CM-like asteroid from the Exolith Laboratory was used (section 1.5). A  $95 \times 95 \times 44$  mm sample was cut in two pieces of about  $95 \times 95 \times 20$  mm for the probe to be placed between those two pieces. During the test, a wire present in the center of the probe heats up and a sensor present on the probe measures the evolution of the temperature of the sample.

Several measurement were made and the thermal conductivity was found to be between 0.43

Figure 1.17: Determination of the thermal conductivity : hot wire method experimental set up used by Avdellidou et al., (2020).



and  $0.47 \text{ W}\cdot\text{m}^{-1}\cdot\text{K}^{-1}$  for  $T = 293 \text{ K}$  which is comparable to Murchison (1.8).

A more complete study is currently in progress in order to determine a greater number of thermal parameters such as the specific heat and the coefficient of thermal expansion. These tests will be carried out under the same conditions as those presented in the Section 1.4.3.1 on meteorites, which will make it possible to compare these results.

### 1.6.2 Mechanical behavior

Many studies have been made to understand the mechanical behavior of the CM chondrites (Hazeli et al., 2018; Avdellidou et al., 2019b; Delbo et al., 2015; Mir et al., 2019). Some are focused on the determination of a macroscopic Young's modulus, others are interested in its reaction during an impact while others study its behavior due to thermal fatigue (as seen in the Section 1.6.1).

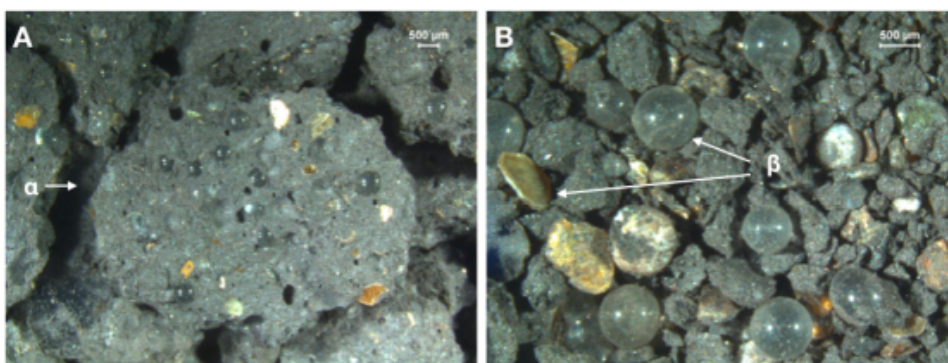
In all the studies presented below, the simulating material developed by the Exolith lab described section 1.5 was used.

In order to simulate the presence of inclusions in the material such as CAIs or more partic-

ularly chondrules, which are spheres composed mainly of silicate minerals such as olivine and pyroxene, glass beads were added to the base material described in section 1.5. The volume proportion of chondrules in a CM-type meteorite is about 20% on average with a diameter of  $300\mu\text{m}$ . Due to the great variation that may exist in the chondrules in size, microstructure or even composition, it was decided to integrate only 15% of glass beads. This allows to have enough inclusions to observe the reactions at the interface between the matrix and the beads while not disturbing the overall behavior of the material. Glass beads of  $600 - 800\mu\text{m}$  were used. This is slightly larger than the average size of chondrules measured in this type of asteroid, however, the size of the glass beads was the closest available to the desired size. This difference in size should not be large enough to have a real impact on the results of the tests carried out.

The hyper-velocity impacts with micrometeorites were studied by Avdellidou et al. (2019b). These tests were carried out using stainless steel projectiles with a diameter of 1 mm with a variable impact speed ranging from  $0.8$  to  $5 \text{ km}\cdot\text{s}^{-1}$ , which is the typical impact speed in the main belt. It has been shown that shock-wave dissipates rapidly as we could expect in this kind of weak material. However, the obtained regolith was unexpected (Figure 1.18).

Figure 1.18: Parts of collected ejecta produced during the impact experiments. In each case, multiminerale large fragments ( $\alpha$ ), monomineralic fragments ( $\beta$ ) and individual inclusions that were attached to a small amount of CM simulant matrix were found (Avdellidou et al., 2019b).

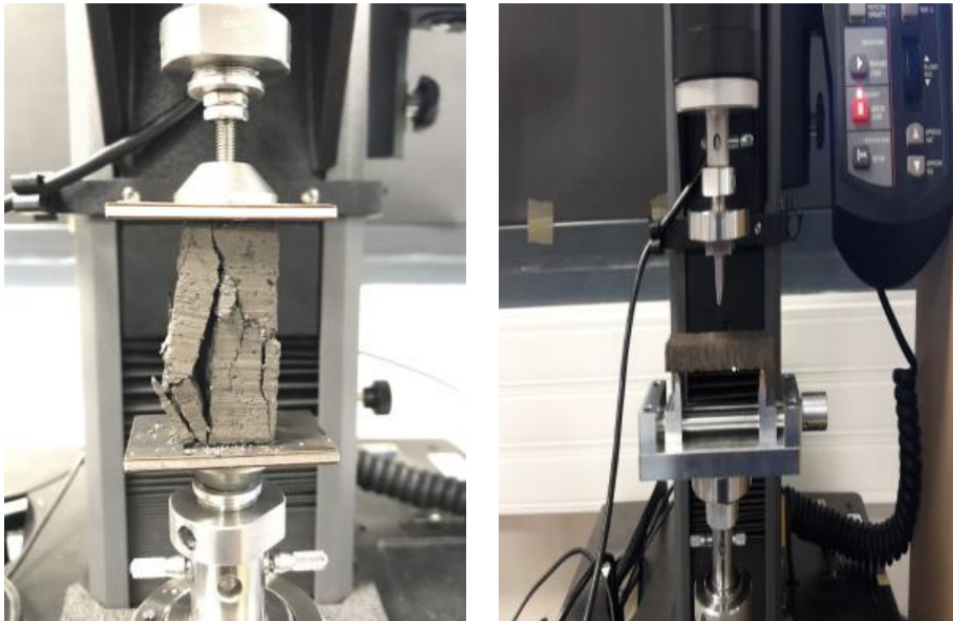


Indeed it was assumed that during an impact, the break appears quickly and the cracks

pass through the grains which gives heteromineralic fragments while those induced by space weathering were assumed to be monomineralic. Due to the slow propagation of the crack induced by thermal fatigue, the crack path is most likely to follow the easiest way which is in the grains boundaries. However, recent studies revealed that monomineralic fragment could occur during impacts. This implies that it is not possible to differentiate regolith due to impacts or space weathering only by looking at its mineralic composition (Figure 1.18).

Compression tests as well as three points bending tests were also carried out on the same simulant to determine the compression elastic modulus, the maximum compressive stress and the flexural strength (Avdellidou et al., 2019b). The experimental set up used for these experiments are shown in Figure 1.19).

Figure 1.19: Experimental set up for compressive tests on the left and three points bending on the right (Avdellidou et al., 2019b).



The samples used during these tests were prepared by cutting the simulants into parallelepipeds of about 20 x 20 x 50 mm for compression test and 10 x 25 x 75 mm for bending tests. The results of the 3-points bending test are presented in Figure 1.20, while those of the

---



compression tests in Figure 1.21.

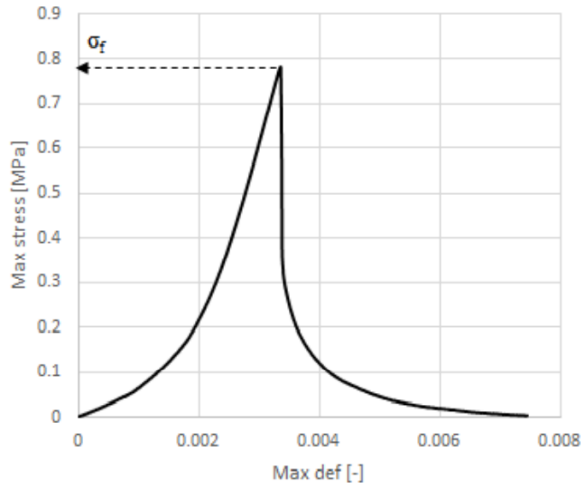


Figure 1.20: Typical stress-strain curves with indication of the flexural strength  $\sigma_f$  (Avdellidou et al., 2019b).

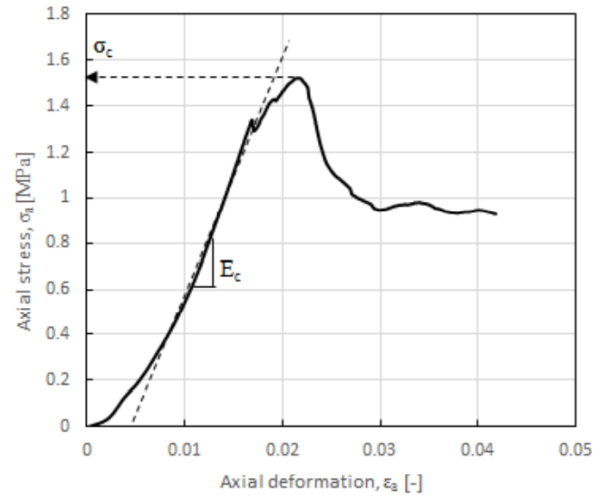


Figure 1.21: Typical stress-strain curves with indication of compression strength  $\sigma_c$  and compression modulus  $E_c$  (Avdellidou et al., 2019b).

From these curves, the compression modulus as well as the maximum compression and bending stresses were estimated (Table 1.5). The results of these mechanical experiments indicate that the compressive and flexural strengths of the CM simulants fabricated and used in this study are quite similar to those estimated from field observations on Bennu (Avdellidou et al., 2019b). To gain more information, we will have to wait for the return of the samples from OSIRIS-Rex space mission scheduled for September 24, 2023.

Table 1.5: Mechanical properties of CM Carbonaceous Chondrite Simulant (UCF/DSI-CM-2) (Avdellidou et al., 2019b)

	$E_c$ (MPa)	$\sigma_c$ (MPa)	$\sigma_f$ (MPa)
mean value	151.67	1.82	0.72
90% conf. interval	17.48	0.17	0.07

## 1.7 Outlines and goals of the thesis

The study of asteroids and their regolith allows to learn more about the first hours of our solar system and therefore to know more about the different stages of its formation. The study of regolith is also very important for the design of rovers which are sent to collect samples in order to be able to predict the interaction between the wheels and the asteroid soil. Better knowing the characteristics of regolith also allows us to better analyze the optical data that we have. It is also of interest for the security of the Earth in order to predict what would happen during the bombardment of an asteroid heading towards Earth. Finally, the basis project on the Moon also raises the question of the use of regolith as building materials.

For these different reasons, the regolith of bodies like the Moon, Mars or even asteroids have been studied. However, many studies are based on observations made of meteorites, yet it has been shown that the bulk mechanical characteristics of asteroids and meteorites can differ greatly (Popova et al., 2011). It is to get as close as possible to the real characteristics of asteroids that this study will not use meteorites but the simulant of carbonaceous meteorites with a CM-like composition with a composition based on the Murchison meteorite. The use of a simulant material available in abundance also makes it possible to carry out a large number of tests and thus to develop experimental methods which once put in place can be used on real asteroid samples which are rare and expensive. The simulant was developed in collaboration with the University of Central Florida (UCF) and Deep Space Industries (DSI) (Britt et al., 2019) and now produced by UCF's Exolith Lab. The mechanical characterization in tension, compression and bending of this material should give important information, allowing for example to integrate these data into numerical models. Finally, thermal cycling tests will be carried out on the simulant in order to observe the creation and propagation of cracks due to the thermal fatigue of the material. These tests will allow to better understand the phenomenon of thermal fracturing taking place on the surface of asteroids and which is thought to be partly responsible for the formation of regolith.

## Chapter 2

# Mechanical tests

*To study the mechanical behavior of the simulant, several kinds of tests were carried out. This chapter explains the methods put in place to carry out these tests. In the first part, the processing of the samples is detailed, from the manufacturing of the material to the machining of the final samples. Then the various tests carried out will be detailed, from the methods to the results. The first test was built to determine the modulus of elasticity in tension as well as in compression. A second test allowed to compute tensile strength of the material. Finally, a third test was ran to find the compression strength and compare the obtained values with the one found by Avdellidou et al. (2019b).*

---

Contents

---

**2.1 Samples preparation** . . . . . 52

    2.1.1 Preparation of the material . . . . . 52

    2.1.2 Preparation of the samples . . . . . 56

**2.2 Young’s modulus characterization** . . . . . 62

    2.2.1 Methods . . . . . 62

    2.2.2 Results . . . . . 65

**2.3 Measurement of the uniaxial tensile strength** . . . . . 71

    2.3.1 Methods . . . . . 71

    2.3.2 Results . . . . . 73

**2.4 Compression tests** . . . . . 75

    2.4.1 Methods . . . . . 75

    2.4.2 Results . . . . . 78

**2.5 Conclusion** . . . . . 82

---

## 2.1 Samples preparation

### 2.1.1 Preparation of the material

The samples used in this study were prepared from the simulant presented in section 1.5. Blocks produced by Exolith lab (Figure 2.1) have been delivered with an announced porosity of 27%. These blocks were identical to those used during the impact studies and the mechanical characterization carried out by Avdellidou et al. (2019b).



(a) Powder of CM2 asteroid simulant



(b) Powder of CM2 asteroid simulant mixed with glass beads



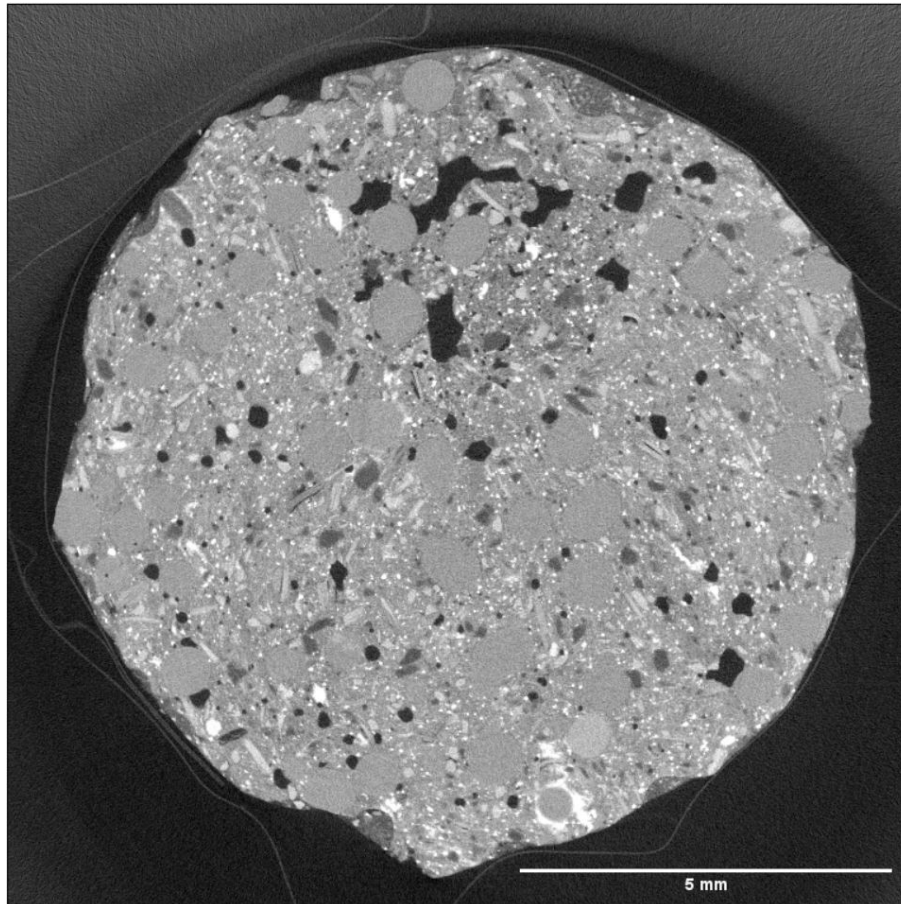
(c) Paste of CM2 asteroid simulant made with the addition of water to the mix

Figure 2.1: Steps of the creation of a block of CM2 simulant

Some blocks were also made with a porosity of 50% to investigate its influence on the me-

chanical behavior of the material. In order to obtain this porosity, methanol was added to the mixture of simulant material and water.

Figure 2.2: Image of X-ray tomography of a CM-like asteroid simulant with a resolution of  $8\mu\text{m}$  per pixel



The porosity, as well as the way it was distributed within the material, was an important factor with regard to its mechanical response to a load. For this reason, several X-ray tomography scans were carried out on the fabricated samples before doing the tests. This technique made it possible to obtain images in gray scale whose intensity depends on the density of the phase. The higher the density, the lighter the phase in the image. In the case of the studied material, some phases had a very similar density which did not allow them to be differentiated on the

images, like for example pyrite and magnetite. However, these images allowed to visualize the main phases, and the inclusions representing the chondrules and the porosities. The first scan was made with a voxel size of  $8\mu\text{m}$  on a cylindrical sample having diameter of 1 cm. (Figure 2.2).

By analyzing the images through thresholding, we realized that only 5% of porosity was visible, which was much lower than the 27% announced. This meant that around 22% of the porosity was at a scale lower than the resolution of these images. For this reason, the second scan was performed with a resolution of  $1\mu\text{m}$  per pixel (see Figure 2.3). The results of the analysis of these images showed a clear increase in the porosity visible in the material. Indeed, one can observe in Figure 2.3b many smaller porosities of only a few pixels in the matrix, as well as within the lamellar phases. These porosities were invisible on the previous scan due to their small size. This rose the porosity observed on this material to about 15%, however still lower than the porosity announced and confirmed by our calculations using the volume and the mass of the material.

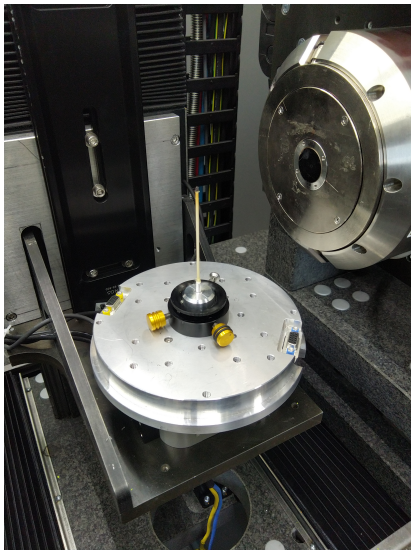
For these calculations, a solid density say  $\rho_{solid}$  was determined by taking into account the composition and the densities of each of the constituents. Then the mass  $M$  and the apparent volume  $V_{apparent}$  of the sample were measured and the bulk density  $\rho_{bulk}$  was deduced (Equation 2.1). The volume of material within the sample was then deduced by dividing the mass by the bulk density (Equation 2.2). Finally, the volume of porosities was the subtraction of the solid volume from the apparent volume (Equation 2.3).

$$\rho_{bulk} = M/V_{apparent} \quad (2.1)$$

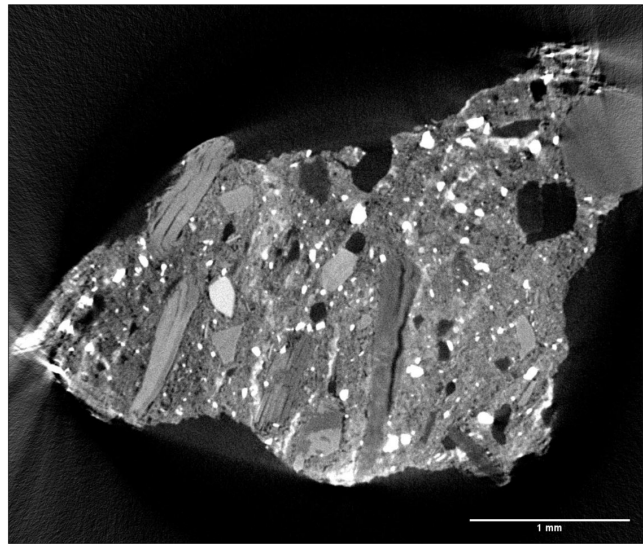
$$V_{solid} = M/\rho_{solid} \quad (2.2)$$

$$V_{porosity} = V_{apparent} - V_{solid} \quad (2.3)$$

This increase of observed porosity showed that the major part of the porosity was on a scale lower than the micron. These results were consistent with images of CM-type asteroids. It can be seen in the Figure 2.4 that the porosities of this CM type meteorite were not very visible at this scale. This verification was not done for samples with 50% porosity.



(a) Set up used to scan the sample in the nano tomograph.

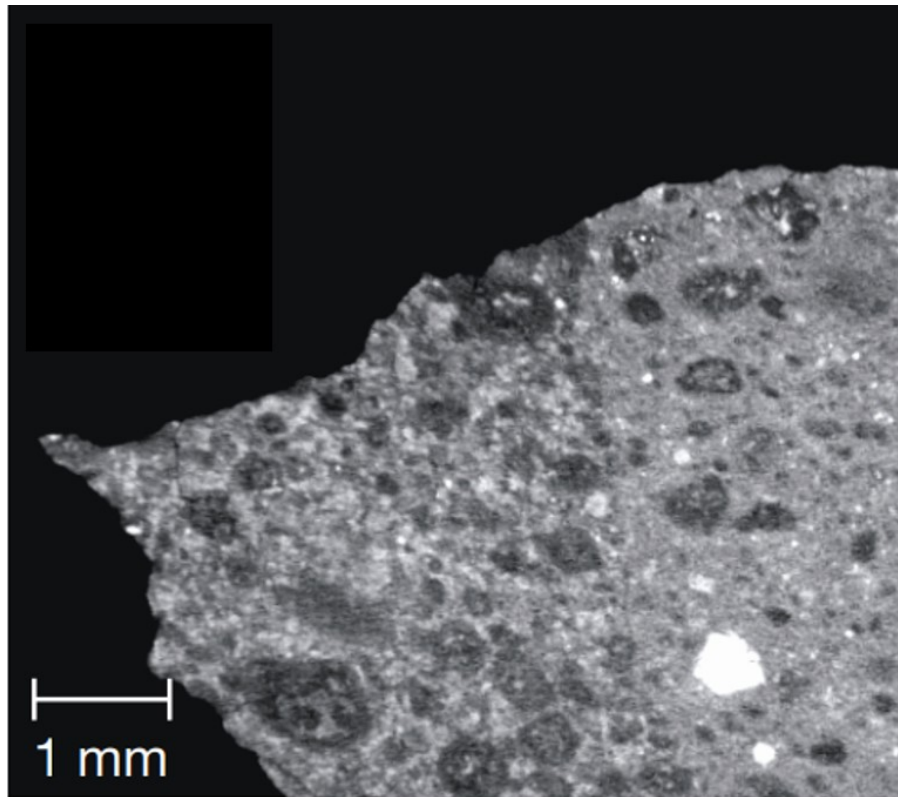


(b) Image of X-ray tomography of a CM-like asteroid simulant with a resolution of  $1\mu\text{m}$  per pixel

Figure 2.3: X-ray tomography of a CM-like asteroid simulant using a nano tomograph

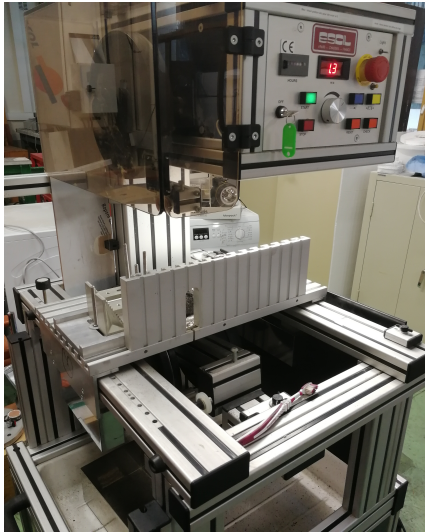


Figure 2.4: Image of microstructure of a CM-type meteorite (Delbo et al., 2014).

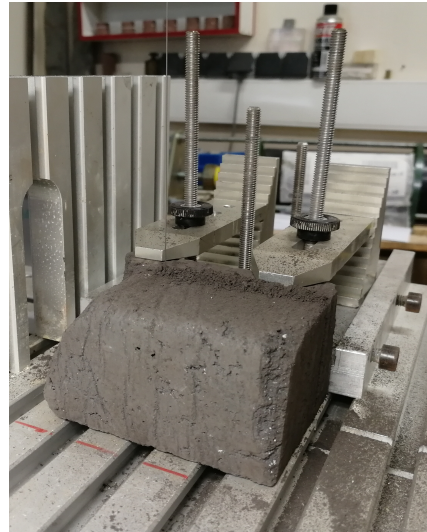


### 2.1.2 Preparation of the samples

A wire saw was used to machine the samples into the appropriate experimental shape (Figure 2.5) from the blocks received. This machining process consisted in making a cut by abrasion thanks to the passage of a wire covered with diamond flakes on the material. This allowed the shaping of the samples while inducing very little vibration in the material and therefore without damaging it. The major drawback of this machining process was the low precision with respect to dimensions (approximately 1 mm) and surface conditions. However, the material being too weak and fragile to be sanded or ground, no better process was found.



(a) Global view of the wire saw



(b) Machining of the simulant block

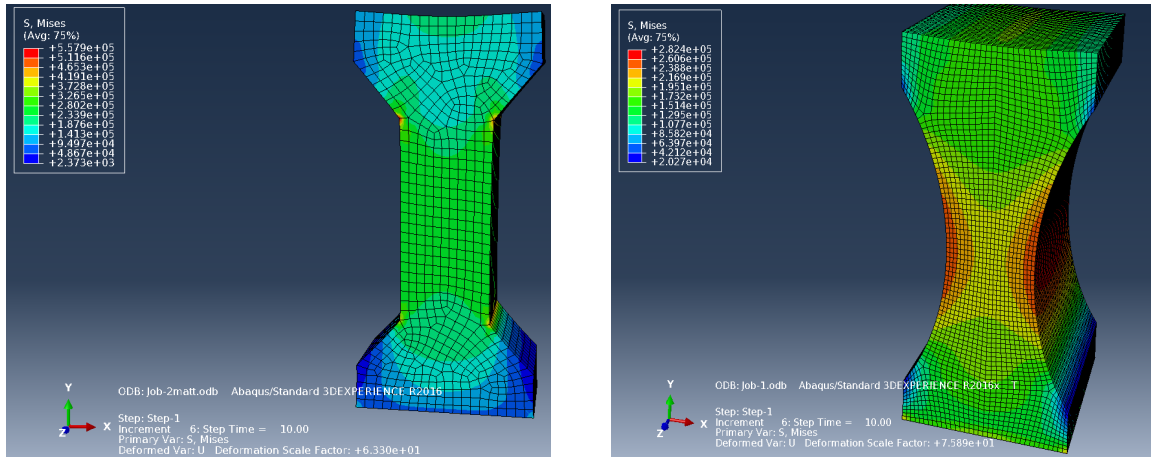
Figure 2.5: Machining of a sample for a tension/compression test using a wire saw

### Samples for Young's modulus characterization

The size of the sample had to be big enough to be representative of the material and as small as possible to facilitate its handling during its installation in the tension / compression machine. A cuboid of 11 millimeters wide by 22 millimeters high was chosen. The material being extremely weak, we chose a parallelepiped shape in order to have as little manipulation as possible during the shaping of the sample and therefore to avoid its damage before the start of the tests.

### Samples for tensile strength characterization

In the case of the tensile strength measurements, the main constraint was to ensure that the rupture would occur in the zone of interest of the sample. In order to meet this criterion, numerical finite element simulations were performed using an isotropic elastic linear constitutive law on the software Abaqus in order to compare two sample's shapes (Figure [2.6](#)).



(a) Sample shape No. 1 : Stress concentration in the corner near the section change (b) Sample shape No. 2 : Stress concentration at the center of the sample

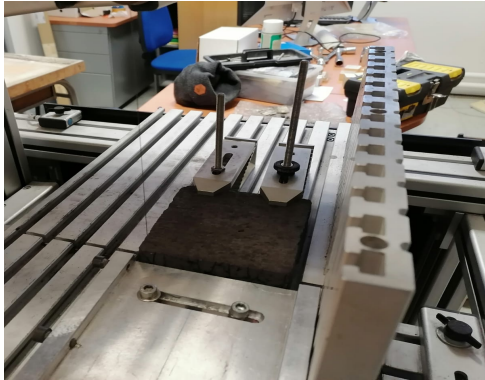
Figure 2.6: Numerical finite element simulation of two different sample shapes in tension

In these simulations, the bottom of the sample was fixed and a tensile force was applied at the top. This showed that with the sample’s shape No. 1 (Figure 2.6a), the stress concentration occurred at the corners where the section changes. The addition of a fillet did not make it possible to completely remove this effect. In the second sample shape (Figure 2.6b) the sharp angles and dramatic section changes have been removed. Although the section was not constant, it could be considered as such in the central zone of the sample which was called the zone of interest. As it can be seen in Figure 2.6b, the highest stresses occur in this zone of interest and stress varies within approximately  $\pm 20\%$  which was sufficient for the present purpose, given the high variability of the samples. The chances of breaking the sample in this area was therefore much higher than for shape No. 1, which was why this configuration was chosen during the tests.

To obtain samples of the desired shape, the same blocks of simulant material were used. They were sliced with a wire saw in order to obtain slices of the desired thickness (20 mm) (Figure 2.7a). These slices were then cut a second time to obtain a block of 20 x 20 x 50 mm.

An aluminum guide was then used to mark the contours of the latter on the simulant (Figure 2.7b). Once the block was engraved, the wire saw was used again, to follow the engraving carried

out previously and thus obtain the desired final shape (Figure 2.7d).



(a) Machining of a sample for tensile strength characterization (step 1) : cutting a slice 2 centimeters thick with a wire saw



(b) Machining of a sample for tensile strength characterization (step 2) : Use of an aluminum pattern



(c) Machining of a sample for tensile strength characterization (step 3) : Engraving the shape of the sample on the material



(d) Machining of a sample for tensile strength characterization (step 4) : Shaping of the sample by line tracking with a wire saw

Figure 2.7: Machining of a sample for tensile strength characterization

**Additional methods tested to shape samples**

In order to make the process of creating the samples simpler and more precise, tests were carried out in order to mold the samples directly into the desired dimensions. To do this, different molds have been designed and manufactured, of different sizes and shapes. As the material was particularly fragile, molds with removable walls were made to facilitate demolding and limit the risk of sample breakage during this stage. Despite the use of these special molds, several difficulties were encountered.



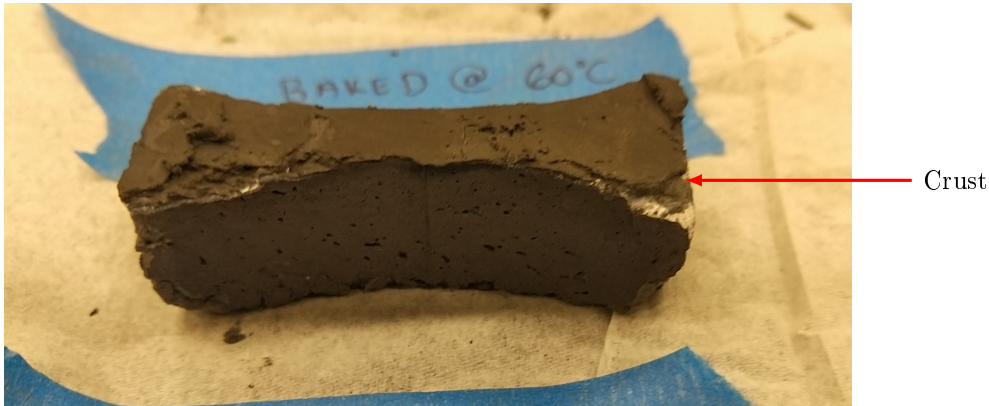
(a) Rectangular sample (40 x 40 x 80 mm)      (b) Tensile strength sample      (c) Rectangular sample (20 x 20 x 40 mm)

Figure 2.8: Different molds tested

The first obstacle was the creation of a crust forming on the surface of the sample. This phenomenon was due to the migration of the salts present in the materials during uneven drying within the oven at 350 K. Although this also occurred on larger blocks like those described in section [2.1](#), the magnitude of the phenomenon was much greater on these smaller samples. By covering the upper part of the mold until the sample was completely dry, it was possible to avoid this crust.

A second major problem was encountered during the molding of the dog bone samples. Indeed, cracks were noticed in the center of the samples during molding. These cracks are formed due to the shrinkage of the material during its drying. Tests have shown a shrinkage of 10% during this step. The shape of the mold did not allow the materials to retract, stresses

Figure 2.9: Darker crust forming on the upper part of the sample



formed in the central part, which in some cases could lead to a rupture of the sample.

The material being very weak, this problem could also be found on the molding of linear samples. Indeed, the material, sticking to the walls of the mold, could lead to the rupture of the sample. To avoid this phenomenon, the walls have been covered with parchment paper. This allowed to produce samples with the desired dimensions.

However, during the mechanical tests of these samples, the results obtained, both the modulus of elasticity and the tensile strength, were much lower than those obtained on the blocks used by Avdellidou et al. (2019b) mentioned above. Several hypotheses have been put forward to explain these variations. The first is based on minor variations in composition due to the manufacturing process of the material or to the change of the glass beads used ( 600–800  $\mu\text{m}$  vs 400-600  $\mu\text{m}$ ). The second is based on the molding process. During molding, despite all the precautions taken, edge effects (impurities / porosities present on the surface, drying too quickly) could damage the material. These defects, although also present during the manufacture of a block of larger size, were negligible when cutting a sample in the heart of the block. In addition, during the handling and machining of the material, the parts most affected by these defects came off and left only the desired material.

## 2.2 Young's modulus characterization

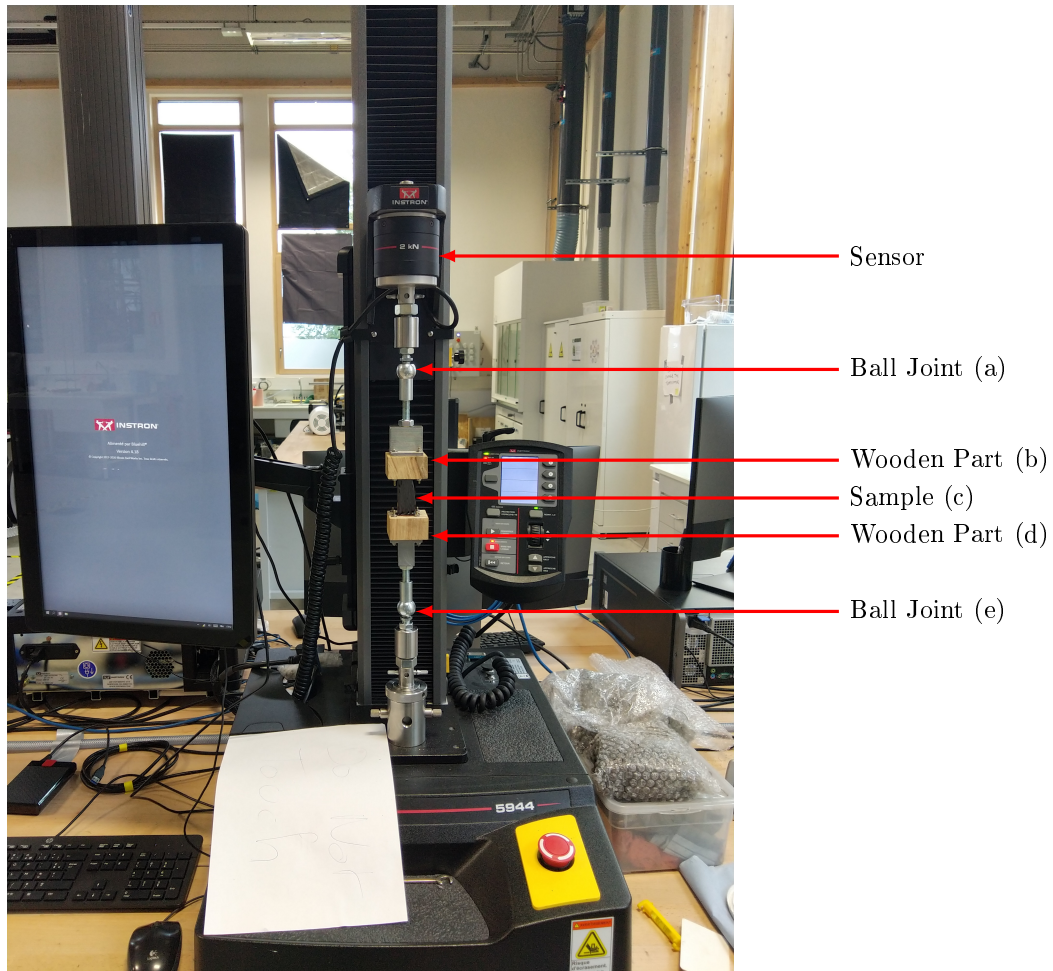
### 2.2.1 Methods

#### Experiment

The first mechanical tests that have been performed were the tensile/compression tests. These tests were carried out at the 3SR laboratory in Grenoble, France. The main goal was to evaluate the Young's modulus, both in tension and in compression. These tests were carried out at room temperature.

The material being very weak, the samples were too fragile to be clenched in the jaws of the testing machine. A system was therefore put in place to make the link between the sample and the jaws of the machine. Two ball joints were added (Figure 2.10 (a) and (e)) in order to align the forces during the test and therefore assured that the sample would only undergo traction / compression. In order attach the sample to the ball joints, two pieces of wood (Figure 2.10 (b) and (d)) previously drilled in four points were used. These wooden parts have been paired to ensure the correct alignment of the assembly. The first piece of wood (Figure 2.10 (b)) was glued with the sample with a fast drying two-component epoxy glue. After about 10 minutes of drying, the glue being strong enough to be handled, the assembly was bolted to the upper ball joint (Figure 2.10 (a)). The second piece of wood is bolted to the lower ball joint (Figure 2.10 (d) and (e)). Glue was then placed on the upper face of the wood and the machine is used to bring the sample into contact with the glue. Once in contact, a compression of 1 N is imposed for 24 hours in order to have control of the bonding pre-stress due to the retraction of the glue during drying. The control of the pre-stress is particularly important because preliminary tests have shown great variations in mechanical characteristics depending on the degree of pre-stress imposed on the sample during the reticulation of the glue.

Figure 2.10: Mechanical tensile/compression cycling experiment set up



Once the sample is in place and the glue has solidified, the test can take place. During each test, 3 cycles were carried out. The preliminary tests showed a phenomenon of damage for small loadings, thus it appeared necessary to make cyclic tests. These allow:

1. to measure the modulus in discharge
2. to quantify the damage as the cycles progress (by observing the reduction of the Young's modulus from cycle to cycle)
3. to ensure that the Young's modulus is identical in tension and in compression



4. to observe the possible appearance of plasticity.

The amplitude of the cycles in terms of displacements was determined following preliminary tests to ensure that failure would not occur. Once the 3 cycles have been carried out, a final loading step takes place in tension up to failure (Table 2.1). During this experiment, the tensile machine was displacement-driven with a velocity of 0.01 mm/s. Force control was not possible because the switch between tension and compression requires to pass through a zero value.

Table 2.1: Mechanical cycles performed

	Start	Cycle 1		Cycle 2		Cycle 3		End
Displacement in percentage of maximum deformation	0	33	-33	50	-50	66	-66	Rupture in tension

During the preliminary tests, an unexpected phenomenon was observed during the drying of the glue, leading to variations in the mechanical characteristics subsequently observed during the tests. In order to limit this phenomenon, a constant force of 1 N in compression was applied throughout the duration of the bonding.

### Samples

The samples were cut using a wire saw with dimensions of 11 x 11 x 22 mm (see Figure 2.11), as described in Section 2.1.2.

Figure 2.11: Typical tensile test samples

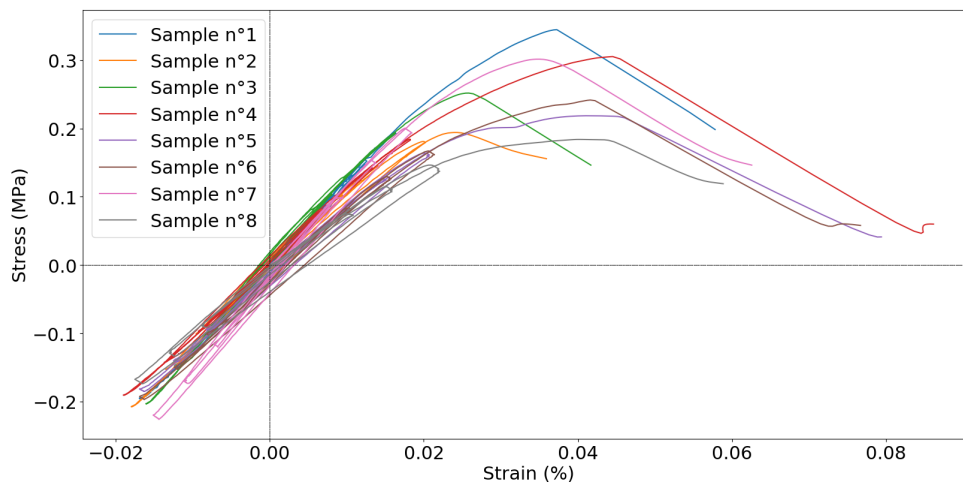


### 2.2.2 Results

The stiffness of the testing machine and the sample attachment system (wooden piece, glue, ball joints, etc.) was measured in order to have a more accurate measurement of the displacement. This correction had a non-negligible impact since there was a factor of 3 between the elastic modulus computed with and without this adjustment, which shows the need to make this correction when using this type of assembly. The results presented in the following parts are therefore the corrected results.

The curves showing the results of the mechanical traction / compression tests are presented in Figure 2.12. A brittle or quasi-brittle fracture was observed on all the tests. This was expected and is in agreement with the tests carried out previously on this material (Avdellidou et al., 2019b).

Figure 2.12: Stress/Strain curves of 8 traction/compression tests



The results also showed that the modulus of elasticity in traction and in compression was identical. Indeed one did not note any change in slope on these curves during the transition from traction to compression (transition located at the origin of the Figure 2.12).

Table 2.2: Results of the traction/compression tests : Young's modulus values for each cycle (MPa)

	Cycle n°1	Cycle n°2	Cycle n°3	Standard deviation
Sample n°1	1307.7	1245.4	1299.9	33.9
Sample n°2	1069.6	1089.7	1018.5	36.7
Sample n°3	1336.9	1256.9	1167.6	84.7
Sample n°4	1178.9	1097.1	1059.1	61.2
Sample n°5	1010.8	952.3	904.3	53.3
Sample n°6	827.6	868.3	883.2	28.8
Sample n°7	1434.8	1149.5	1135.6	168.9
Sample n°8	779.6	777.2	789.5	8.9

The values of the elastic moduli for each cycle were calculated during the unloading, i.e. the decreasing part of the curve for the reasons stated previously in section [2.2.1](#). These moduli had values close to each other and their evolution during the tests did not show any obvious signs indicating the presence of damage over this range of force ([2.2](#)).

The modulus of elasticity of each sample was calculated by averaging over the three cycles carried out. The value of the tensile strength was determined by the highest stress value reached as the samples during the test.

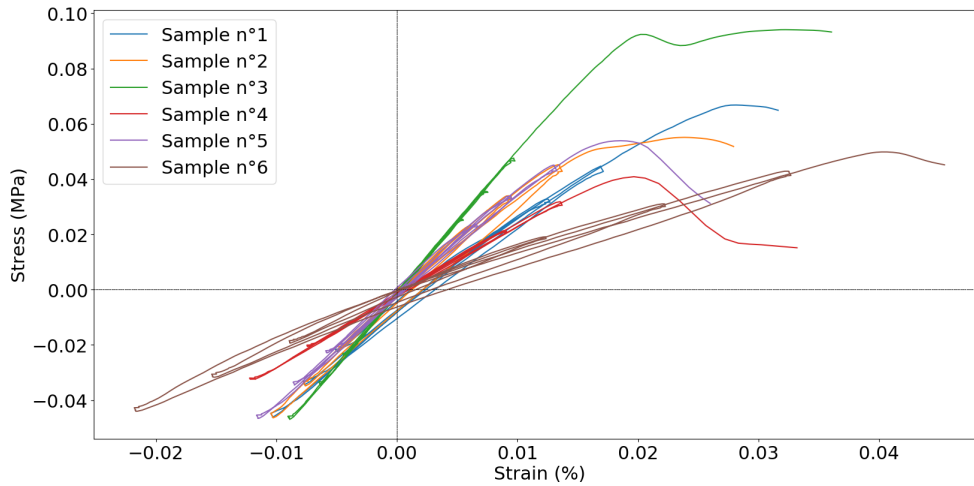
Table [2.3](#) shows all the values of Young's modulus and tensile strength measured for the various samples as well as their average value and their standard deviation on all the tests carried out.

Table 2.3: Results of the traction/compression tests : Mean Young's modulus calculated over the three cycles realized and tensile strength

	Mean Young's Modulus (MPa)	Tensile Strength (kPa)
Sample n°1	1284.3	344.8
Sample n°2	1059.3	194.2
Sample n°3	1253.8	251.9
Sample n°4	1111.7	305.4
Sample n°5	955.8	218.6
Sample n°6	859.7	241.7
Sample n°7	1239.9	301.6
Sample n°8	782.1	184.0
Mean Value	1068.0	255.3
Standard Deviation	189.7	57.3

If we compare these results to those obtained in previous tests on the same material, we can see that the Young's modulus calculated in this experiment is 7 times higher than the compression modulus measured by Avdellidou et al. (2019b). Additional tests were carried out to investigate this difference in value (Section 2.4). The tensile strength measured in tension during these tests was approximately 7 times lower than that found for the compression by Avdellidou et al. (2019b). This was not surprising taking into account the fact that this material was an agglomerate of powders. This was the type of behavior that we found in concrete, for example. The tensile strength was also lower than the one measured by Avdellidou et al. (2019b) on bending tests. However for most materials, the uniaxial tensile strength is lower than the flexural strength. This is usually explained by the fact that the tensile stress is homogeneous in the uniaxial test, and therefore failure can be triggered by any defect in the bulk. In the case of 3 points bending, failure necessarily occurs in a small region where the tensile stress is maximum, in which the probability of having defects is lower.

Figure 2.13: Stress/Strain curves of traction/compression tests on 50% porosity samples



These tests were also carried out on the material simulating 50% porosity. From the curves presented in Figure 2.13, the Young's moduli were calculated for each sample using the same method as previously employed for the 27% samples (Table 2.4).

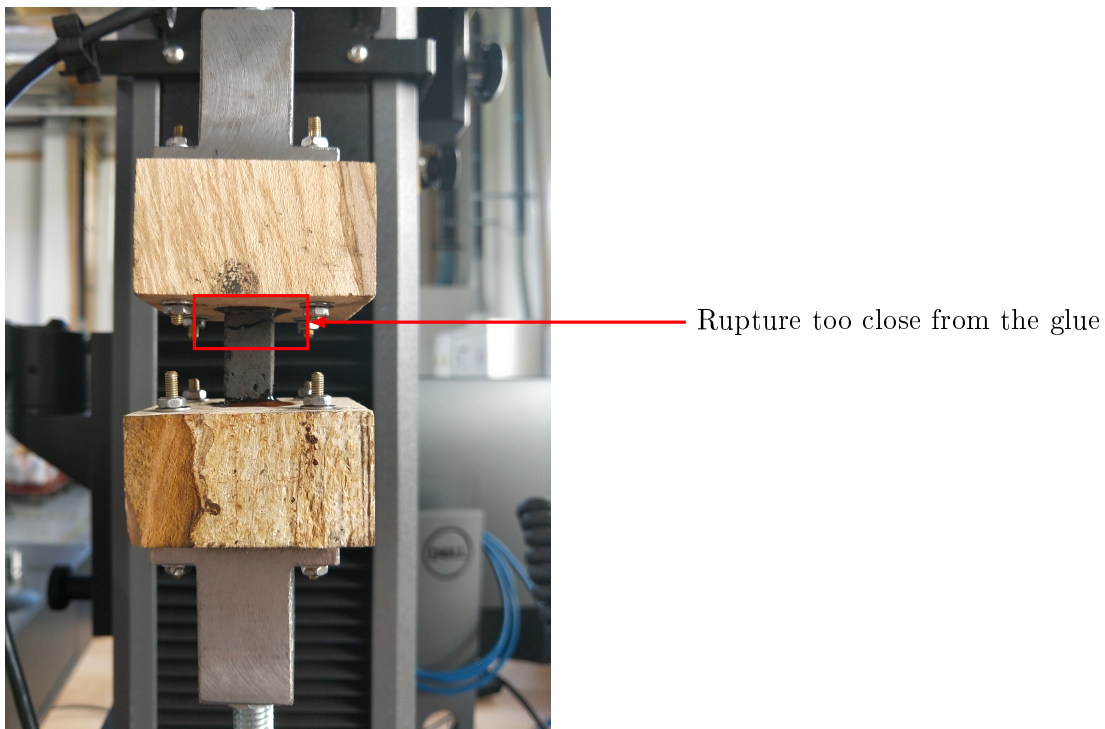
Table 2.4: Results of the traction/compression tests on 50% porosity: Mean Young's modulus calculated over the three cycles realized and tensile strength

	Mean Young's Modulus (MPa)	Tensile Strength (kPa)
Sample n°1	263	66.8
Sample n°2	329	55.1
Sample n°3	507	94.1
Sample n°4	234	40.8
Sample n°5	349	53.9
Sample n°6	160	49.8
Mean Value	307	60.1
Standard Deviation	119	18.7

The values obtained during these tests on samples with 50% porosity were lower than those obtained on samples with 27% porosity, which was expected. The 23% increase in porosity would therefore have the effect of a drop of about 75% in Young's modulus and tensile strength. These results showed the great role that porosity plays in the mechanical strength of this material.

It can be observed on Figure 2.13 that on sample 6, a hysteresis and a residual deformation increased from cycle to cycle. This behavior also appeared on samples 1 and 2, but to a lesser extent and only during the last cycle. This could be due to damage to the material from its initial state, which would explain its lower Young's modulus and tensile strength. On the other hand, it can be noticed that on sample 3, this hysteretic behavior did not appear, which seemed to indicate that the initial state was less damaged or porous, which could explain its higher Young's modulus and tensile strength.

Figure 2.14: Rupture of a sample during a mechanical traction/compression test



However, the rupture took place either directly at the interface between the glue and the

samples (Figure 2.14), or at the periphery, which makes the interpretation of these values difficult. In order to study more precisely the tensile failure of the material, additional tests were also carried out (Section 2.3).

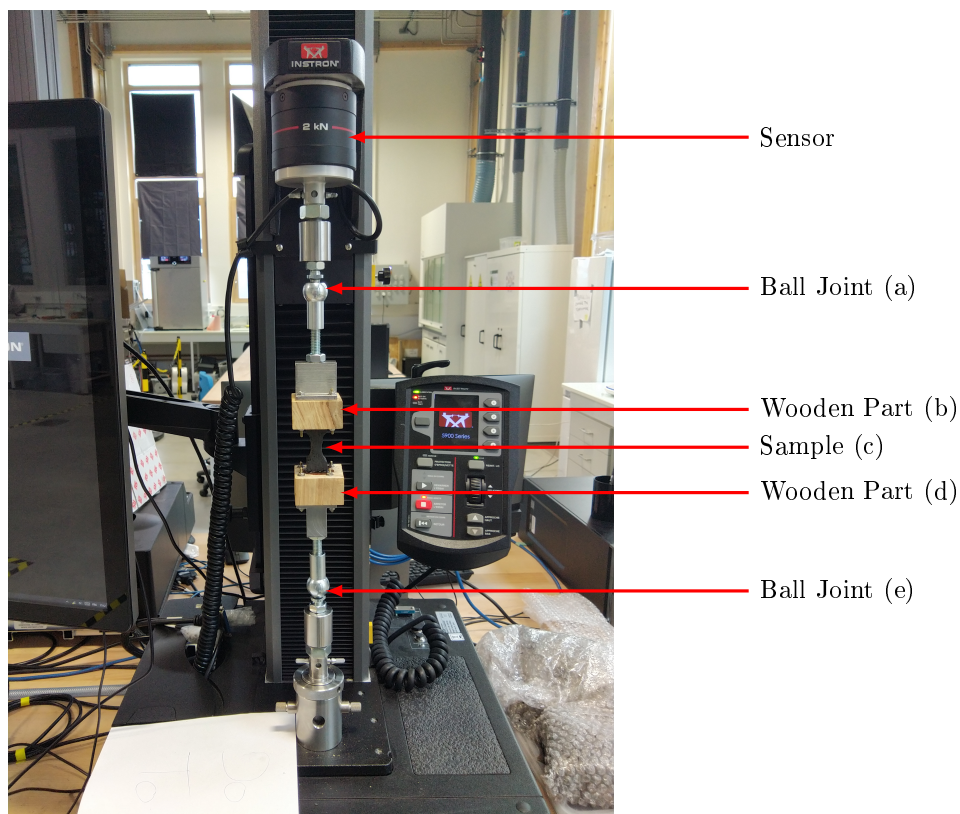
## 2.3 Measurement of the uniaxial tensile strength

### 2.3.1 Methods

#### Experiment

During the previous tests, the glue may have played a role during the breakage. In order to avoid this problem, a new experiment was set up with the aim of breaking the sample in its center, far from the glue/sample interface or from a change of section. To do so, the experimental set up used is shown Figure 2.15.

Figure 2.15: Mechanical tensile test set up



This set up was based on the one been used to performed the mechanical tension / compression cycling tests (Section 2.2.1). There were two main changes made between these two experiments.



The first was the reduction of the velocity from 0.01 mm/s to 0.002 mm/s during the tests in order to minimize dynamic effects. The second and most important change was the sample's shape.

### Samples

To ensure that the sample would not break at the glue / sample interface, numerical simulations were carried out in order to compare different shapes of specimen (Section [2.1.2](#)). Finally, the shape shown in Figure [2.16](#) that was retained. For more details on sample construction, please see Section [2.1.2](#).

Figure 2.16: Tensile test sample glued on a piece of wood

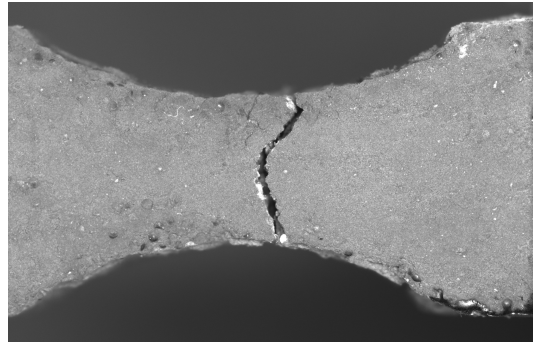


These samples had a height of 50 mm for a thickness of 20 mm and had a width of 10 mm in the center, in the area of interest, and a width of 20 mm at both ends, in the bonding area.

### 2.3.2 Results

Ten tests were carried out. For these tests, the rupture took place in the center of the sample as shown in Figure 2.17. This rupture is therefore consistent with the numerical simulations carried out beforehand.

Figure 2.17: Rupture of a sample during a mechanical traction test



The results obtained during these tests were reported in Table 2.5. Note that the average calculated value for both material was very close to the values obtained during the previous tests but that the standard deviation was smaller. This result on the 27% porosity material was also 7 times lower than the measurements made in compression by Avdellidou et al. (2019b), which is consistent for this type of material. These values are also much lower than the measurements made on meteorites, which is also consistent with the observations of Popova et al. (2011). Moreover, these results are consistent with the estimations of tensile strength of the rocks of Bennu given between 200 kPa and 280 kPa by Grott et al. (2019).

Table 2.5: Results of the tensile tests : tensile strength (given in kPa)

	Tensile Strength (kPa)	
	27% porosity material	50% porosity material
Sample n°1	255.4	58.7
Sample n°2	242.5	88.1
Sample n°3	273.7	74.8
Sample n°4	203.9	83.5
Sample n°5	268.9	58.3
Sample n°6	266.7	51.9
Sample n°7	205.4	61.0
Sample n°8	231.0	56.3
Sample n°9	223.9	67.5
Sample n°10	266.0	
Mean Value	243.7	66.7
Standard Deviation	26.5	12.7

## 2.4 Compression tests

### 2.4.1 Methods

#### Experiment

In order to understand the differences between the modulus of elasticity in compression obtained during the previous tests and those obtained by Avdellidou et al. (2019b), two additional compression tests were carried out.

The first one reproduces the procedure used by Avdellidou et al. (2019b). The sample was placed between two compression plates (Figure 2.18a).

The second one (Figure 2.18b) was very similar to the test carried out in section 2.2.1, except that a ball joint has been removed in order to limit the risk of the buckling. For this test, the sample was glued to two pieces of wood. The glue allowed to have a better distribution of the compression forces on the surface of the sample. Indeed, during a compression test, the condition of the two surfaces on which the forces will be applied is very important. The surfaces must be parallel and as flat as possible with a minimum of roughness so that the forces are correctly distributed over the whole surface. Taking into consideration the machining of the sample and the impossibility of polishing this material, it was chosen to glue the sample in order to minimize the problems at the interface. Like the tests presented in Section 2.2.1 and 2.3, the pieces of wood were then bolted to a set of steel parts connected to the machine.

The speed chosen for these tests was set to  $4 \times 10^{-5}$  mm/s.



(a) Compression Set-up No. 1 : Identical to the experiment carried out by Avdellidou et al. (2019b) (b) Compression Set-up No. 2 : Glued sample

Figure 2.18: Set up for the mechanical compression tests

## Samples

Due to the difference in size of the two experimental devices, a different sample was made for these two tests. The two samples were machined from the same material, already used during the previous mechanical tests. For the sample used during the compression tests carried out with the set up n°2, a wire saw was used to cut a block with a section of  $20 \text{ mm} \times 20 \text{ mm}$  and a height of 50 mm (Figure 2.19a). Those dimensions are the same which were used by Avdellidou et al. (2019b) in the study presented in Section 1.6.2. For set up No. 1, a sample of smaller size had to be used because of the smaller dimensions of the compression plates at our disposal. A cylindrical sample of 10 mm in diameter and 20 mm in height was therefore used (Figure 2.19b). Such shape of sample was used for the thermal cycling test (more information on the machining

of this sample in the Section [3.1.4](#)).



(a) Compression sample used for the experiment No. 2



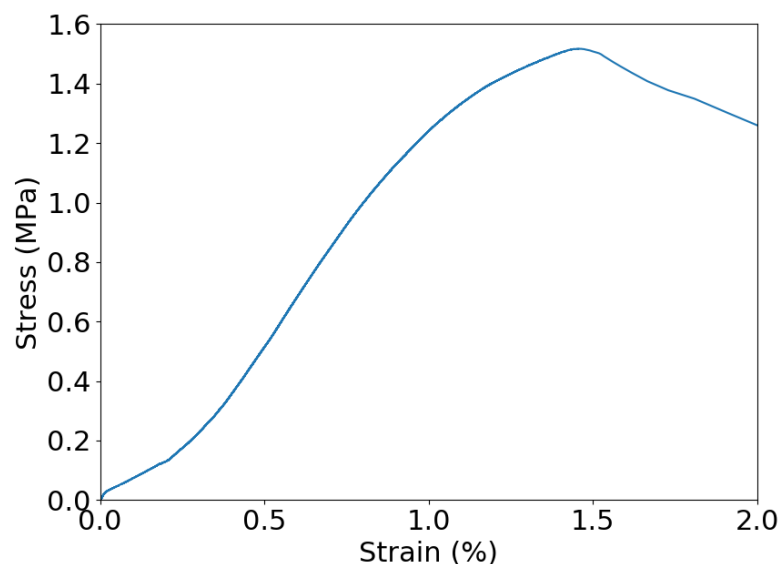
(b) Compression sample used for the experiment No. 1

Figure 2.19: Compression Samples

### 2.4.2 Results

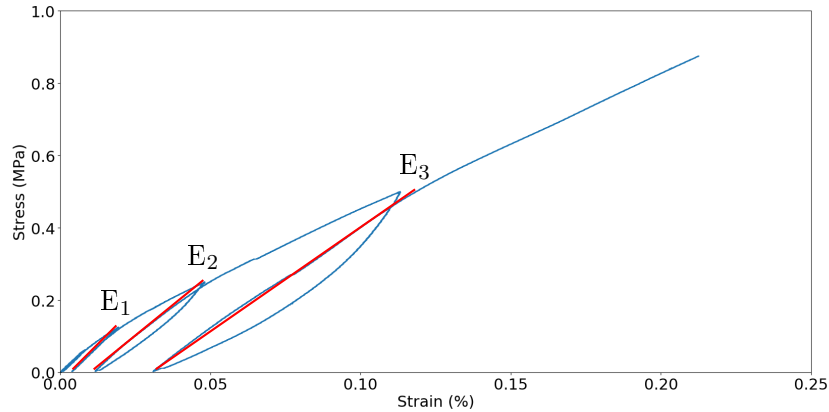
The tests carried out with the compression set-up No. 1 showed a modulus of elasticity and a compression strength close to what had been found by Avdellidou et al. (2019b) on samples of dimension  $20 \times 20 \times 50$  mm. This result suggested that the sample size did not affect the result of the compression test significantly. When we observe the stress/strain curve (Figure 2.20), we note a change in slope at the start of the test. This may be due to the poor quality of the surfaces carrying the load (asperities, ridges, poor alignment of the planes, etc.).

Figure 2.20: Typical beginning of a compression curve using the set up n°1



The tests carried out with the compression set-up No. 2 showed a modulus of elasticity close to what had been found during the first tests presented in Section 2.2.1. The curve shown below represents one of these tests (Figure 2.21). It was chosen to carry out cyclic tests in order to monitor any damage to the sample which would result in a reduction in Young's modulus and therefore a change in the slope of the curve from one cycle to another.

Figure 2.21: Typical curve of a cyclic compression test using the set up n°2



This curve provided information on various aspects of the samples' behavior. We noted that there was no longer any changes of slope at the base of the curve, unlike during the tests carried out with set up No.1. The loading / unloading sequence showed a hysteretic behavior. The hysteresis became significant during the third unloading / reloading sequence, with a strain of approximately 0.04% before unloading, which is beyond the tensile limit (Figure 2.12). This explains why this phenomenon was not observed during the previous tests. During the unloading, we also saw that the curve did not return to the origin, which indicates the presence of a permanent deformation. The presence of viscous behavior is also a possibility. We saw that the stiffness of the envelope curve cannot be considered as being the elastic modulus since it was not identical between loading and unloading and therefore the material cannot be considered as linear elastic in this range of accumulated strain. Moreover, one noted a change of slope when the loading joined the curve envelope which resembles an elastic limit as in plasticity. The Young's modulus was assimilated here to the stiffness of the reloading curve, which was approximately linear, for simplicity. A decrease in the modulus of elasticity was observed from cycle to cycle, which indicates the presence of damage (Table 2.6). The Young's modulus retained was therefore the one measured during the first cycle ( $E_1$ ), with the lowest level of damage. Besides, the value of strain in the first cycle was close to the value of strain considered in previous tests of Section



[2.2.2](#) This value, although in the low range of the values measured during the tests presented in Section [2.2.2](#), remained consistent with them.

Table 2.6: Evolution of the modulus of elasticity in cyclic compression

	Young's modulus (MPa)
E <sub>1</sub>	771.5
E <sub>2</sub>	694.2
E <sub>3</sub>	629.3

The hysteritic behavior evoked the post-peak behavior of concrete. The similarity of the loading/unloading cycle with those observed for post-peak behavior of concrete suggested that similar phenomena were at stake. The shape of the hysteresis could be explained by considering opening and closing of micro-cracks (providing the non-linearity) coupled with friction between the crack walls (providing the hysteresis). In this interpretation, the hysteresis is an indicator of damage, which is in accordance with the reduction in the reloading stiffness from cycle to cycle.

The table below highlights the differences in results obtained depending on the test performed (Table [2.7](#)).

Table 2.7: Comparison of the compression results obtained for the two types of tests

	mean Young's modulus (MPa)
Set up No.1	177.5
Set up No.2	771.5

The results confirmed that the differences between test setup No. 1 and test setup No.2 were due to the contact surface. Indeed during the first tests carried out by Avdellidou et al. [\(2019b\)](#), the sample was simply placed between two compression plates while during our tests, the sample was glued. The glue avoided interface problems and improved the homogeneity of the load applied to the sample, unlike the first method. In addition, as the surface condition of the sample was not

perfect due to the difficulties related to the machining of such a weak and crushable material, the glue allowed to compensate these defects. The absence of slope change at the beginning of the stress-strain curves (the slope change – progressive increase of the apparent stiffness – being usually due to a progressive formation of the contact surface between the samples and the compression plates) confirmed the improvement brought by the glue.

The large difference in results could therefore be explained by advanced damage of one part of the sample due to the presence of a ridge or a lack of parallelism between the lower and upper part of the sample, even before the two compression plates were in contact with the entire sample. As a result, the sample was significantly damaged before the contact surface between the sample and the compression plates was fully established, which reduced the overall modulus of elasticity of the sample.

## 2.5 Conclusion

In this study, the mechanical characteristics in tension as well as in compression were investigated on a CM asteroid simulant material manufactured by the exolith lab at UCF. This simulant is based on the petrological composition of the CM type Murchison meteorite. A series of tests had to be developed in order to carry out these tests on this very little known material.

The tensile strength and Young's modulus of the 27% porosity material, respectively around 250 kPa and 1 GPa, are much weaker than those obtained during similar tests carried out on meteorites, however, they seem consistent with the observations made by Popova et al. (2011) which show that asteroidal rocks are much weaker than meteorites present on Earth.

On the other hand, these results led to redo compression tests because of a difference in the modulus of elasticity with the study of Avdellidou et al. (2019b). This verification confirmed the Young's modulus values of 1 GPa obtained previously.

Tests on the material at 50% porosity showed a lower Young's modulus and tensile strength, respectively 307 MPa and 60 kPa. These results show the importance of porosity on the mechanical strength of this material and therefore the importance of controlling it precisely during the manufacturing process.

Beyond the experimental results obtained, this study has enabled the implementation of experimental processes that can be reused for future tests on similar materials such as lunar simulant, martian simulant, other asteroid simulant, possible samples from space missions, etc. In addition, this study also underlined the difficulty of molding a sample directly without inducing defects and thus to determine certain rules concerning the shaping of the sample from the simulant material.

However, these results, although encouraging, have certain limitations. It would be interesting to carry out these tests in an environment closer to real conditions. For this, tests carried out at different temperatures, at controlled humidity or in a vacuum, could be particularly interesting. Moreover, since this material is man-made, it would also be important to measure

the repeatability of the process.



## Chapter 3

# Thermal cycling

*The mechanism responsible for the creation of regolith on the surface of an asteroid is currently under discussion, scientists being divided between the effect of thermal cycling and the effect of mechanical impacts. In this chapter, the creation of regolith by thermal cycling is investigated. For this purpose, an innovative thermal cycling experiment has been developed and designed to allow monitoring of the evolution of the material. In the first part, the setting up of the experiment is detailed, starting from the thermal simulations serving as a basis for the study, up to the design of the experimental assembly, to finish with the obtaining of the samples. A second part presents the results and details their processing.*

Contents

---

<b>3.1 Methods</b> . . . . .	<b>87</b>
3.1.1 Thermal cycles on asteroids . . . . .	87
3.1.2 Experimental set up . . . . .	89
3.1.3 Experimental design . . . . .	93
3.1.4 Samples preparation . . . . .	95
3.1.5 Image analysis . . . . .	97
<b>3.2 Results</b> . . . . .	<b>103</b>
<b>3.3 Conclusion</b> . . . . .	<b>115</b>

---

## 3.1 Methods

An asteroid is subjected to large temperature variations during day/night cycles that can reach a difference of more than 200 K. In addition, the rotation period of asteroids is usually shorter than the Earth, typically a few hours. These strong variations and their repetitions, coupled with the great heterogeneity of the microstructure of the rock composing the asteroid, could be responsible for the creation of regolith due to thermal fracturing. This hypothesis is studied in different articles (Delbo et al., 2014; Hazeli et al., 2018; Molaro et al., 2020).

The various studies carried out until now have made it possible to establish the possibility for an already existing crack to propagate or to be created at certain places presenting high stress concentrations, on a meteorite, due to thermal cycling (Delbo et al., 2014). The study by Molaro et al. (2020) presents a number of photographic images from the OSIRIS-REX space mission which show cracks strongly resembling thermal cracking. However, although these results are very encouraging, nothing so far allows us to certify that these cracks are actually of thermal origin. Moreover, the study proposed by Delbo et al. (2014) being based on meteorites already presenting cracks and a particular geometry, it is difficult to extend their conclusions regarding the thermal cracking of the asteroidal rock.

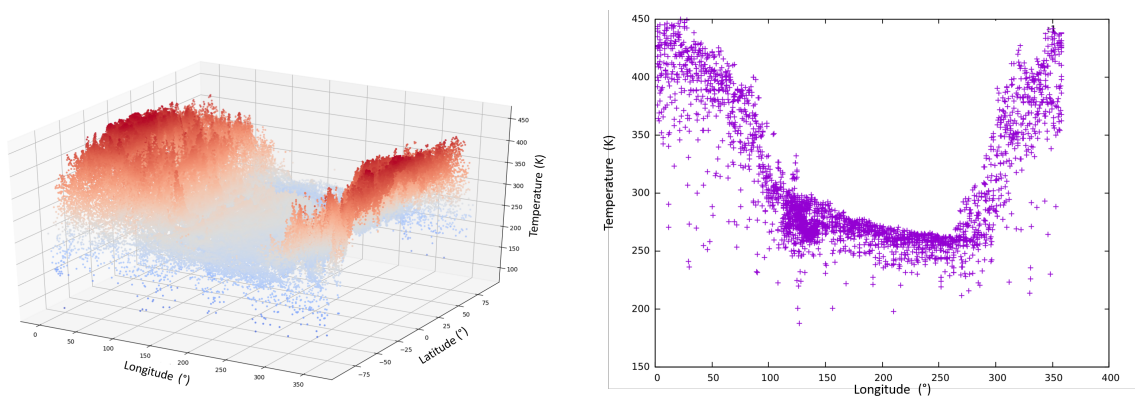
Several questions then arise. Are the results observed by Delbo et al. (2014) extrapolable to asteroids? Could thermal fatigue be responsible for the appearance of cracks without the help of stress concentrations due to the geometry? And if so, after how many cycles? How long would it take to create the thickness of regolith present on the surface of asteroids? What would be the mechanisms responsible for these possible thermal cracks?

### 3.1.1 Thermal cycles on asteroids

In order to answer these questions, the first step was to perform a numerical simulation to confirm the temperature evolution of a typical C-Type Near Earth Asteroid. The simulation was based on the asteroid 101955 Bennu because of the large number of studies carried out in



recent years on this asteroid and the ease of finding the parameters necessary for the operation of the simulation. A code created by Delbo et al. (2015) was used to make this calculation using a thermophysical modeling method. This code takes into account different factors such as the albedo, its distance from the sun, its emissivity, its thermal inertia or its rotation speed. These information were essential to solve this calculation of heat transfer by radiation which is the main source of heat exchange in space. The topology of the asteroid also matters. This code also used the surface topology of the asteroid to recreate a temperature map on its surface (Figure 3.1a).



(a) Temperature evolution (in Kelvin) in function of latitude and longitude.

(b) Evolution of the temperature (in Kelvin) in function of the longitude.

Figure 3.1: Evolution of the temperature at the surface on a typical NEA

The results of these simulations confirmed the  $\Delta T$  of approximately  $200^{\circ}\text{C}$  between the day and the night used by Delbo et al. (2014) and provided insights on the temperature evolution. The evolution of the temperature on the 3D map allowed to observe a maximum variation of the temperature at the level of the equator and the temperatures at the level of the two poles changing very little. It can be seen by moving from a 3D map to a 2D map by projecting this cartography on the Temperature / Longitude plane that the temperature increased very strongly until it reached its maximum whereas the decrease was slower (Figure 3.1b).

### 3.1.2 Experimental set up

In order to design an experiment which reproduces comparable thermal cycles in the laboratory, it was decided to use the temperature difference between the liquid nitrogen and the ambient air to obtain a  $\Delta T$  of approximately 200 K, close to the one previously calculated. The idea was therefore to immerse a sample in liquid nitrogen until its temperature was homogeneous and then to take it out and let it warm up until it reaches room temperature again, and so on.

The thermal cycling temperatures were therefore lower than those calculated at the surface of Bennu (Figure 3.1). Moreover, the evolution of the coefficient of thermal expansion on CM-type meteorites is not linear over this temperature interval (Figure 1.9). However, the choice to carry out tests on this temperature range was motivated by technical reasons and by the possibility of reducing the duration of the thermal cycle (compared to cycling in an oven for example). Moreover, the temperature calculated on the surface of Bennu was valid only at one instant of its rotation around the sun. The latter being elliptical, the distance from the sun varies and therefore the thermal cycles too. There are also a sufficient number of asteroids to be able to attest that there are asteroids passing through these temperatures.

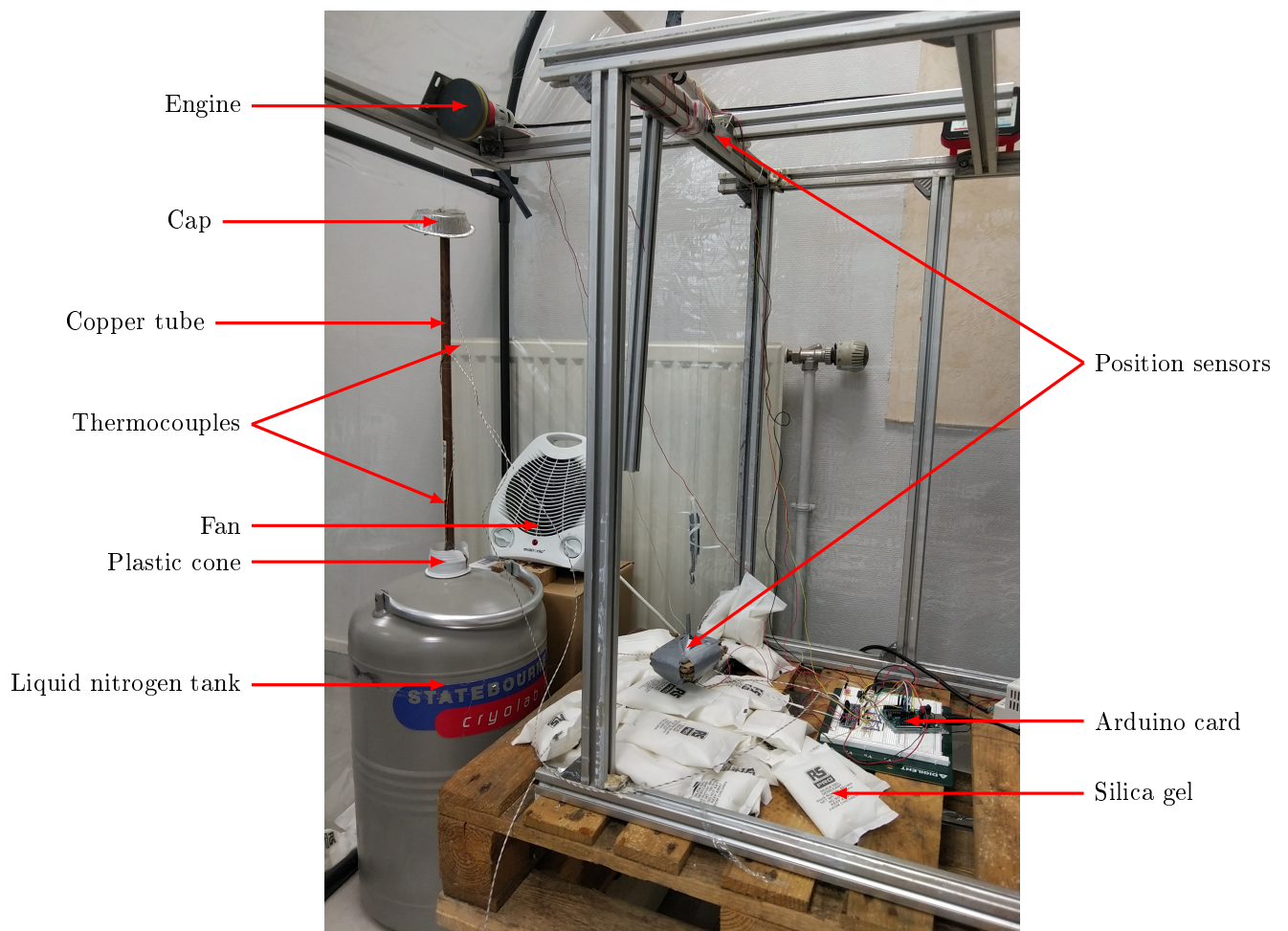
A system has therefore been designed to carry out these temperature cycles. A DC motor moved the sample up and down in a container filled with liquid nitrogen (Figure 3.2). This motor was controlled by an Arduino card (developed ad-hoc) in order to properly control the cycle times. Two contact sensors were used to detect the high and low positions of the sample.

The main problem when working at very low temperatures was related to the ambient humidity which created a layer of frost around the material and the sample. The frost then melted and damaged the sample which was very sensitive to liquid water. Once moistened, the sample softened until it became a sort of malleable paste, and the test was interrupted.

A sort of climatic chamber containing a significant quantity of silica gel was built up to try to absorb humidity. However, this solution was not efficient enough due to the size of the chamber and the necessity to frequently open it for the handling of the samples. A more practical method was the following.

In order to ensure that the sample was not in contact with water, it was placed in a hermetically closed copper tube. In addition to this, the sample was also wrapped in an aluminum foil to add moisture protection while improving the contact (and therefore the conduction of heat) between the sample and the copper tube. Copper and aluminum being both very good thermal conductors, this technique preserved the integrity of the sample without increasing the duration of the cycles significantly.

Figure 3.2: Thermal cycling experimental set up at high position (tube outside the liquid nitrogen tank)



A thermocouple was placed outside the copper tube to ensure the presence of liquid nitrogen in the tank. A second thermocouple was placed inside the tube in order to follow the evolution of the temperature inside it. For preliminary tests a thermocouple was also placed inside the sample. Further details about this third thermocouple will be given below. The values of these thermocouples were read and displayed in real time on a computer to ensure the proper development of thermal cycles. In order to improve the efficiency of thermal convection with ambient air, a fan has been added.

For the sake of saving liquid nitrogen, and thus increasing the number of cycles possible before having to fill the tank, a cap has been placed over the copper tube in order to close the tank once the tube is inside. This has the effect of retaining some of the nitrogen vapor inside the tank and therefore limiting losses. This also allowed to limit the creation of frost above the tank. To prevent this problem, a plastic cone was also placed at the entrance of the tank to prevent the air blown by the fan from entering the tank.

The evolution of cracks within the samples was followed using micro computed tomography ( $\mu$ CT). The sample was CT-scanned after different number of cycles using the 3SR and SIMAP X-ray CT-scanners both located on Grenoble campus (Table 3.1).

Table 3.1: Number of cycles carried out between each intermediate scan

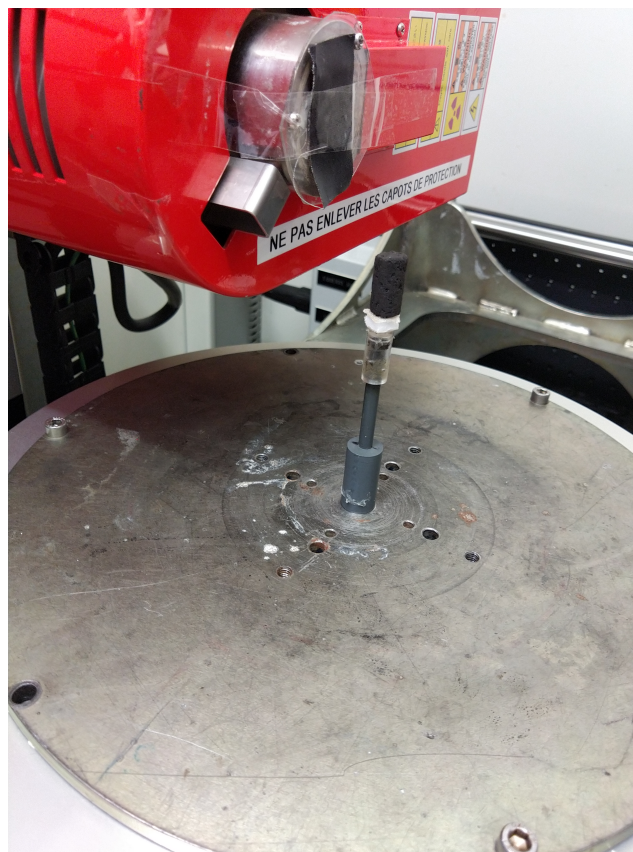
Test	Reference Scan	Scan n°1	Scan n°2	Scan n°3	Scan n°4
1	0	70	140	270	400
2	0	97	215	485	

From these data, a 3-dimensional image with a resolution of  $8 \mu m$  in gray level representing the different phases present within the sample was generated. The gray levels representing the different phases depend on their density. These images therefore made it possible to observe the microstructure of the sample and thus to detect possible departures of crack or decohesion between the different phases of the material. In order to limit the noise on the images resulting

from the X-ray tomography, the low intensity electrons were filtered thanks to the use of a copper filter placed at the level of the source. The 3D images obtained were then processed using a procedure which will be described in details in Section [3.2](#).

In the X-ray CT-scanners used throughout this study, the source as well as the sensor were fixed and the sample was placed on a rotating plate. It was essential that the sample did not move throughout the scan, which lasted several hours, in order to obtain sharp images. To this end, the sample was stuck using double-sided tape on a piece of polystyrene foam (Figure [3.3](#)) which, thanks to its low density, did not appear on the images.

Figure 3.3: Setup used for X-ray tomography scans



### 3.1.3 Experimental design

Numerical simulations were then carried out using the finite element software Abaqus in order to estimate the time necessary to complete a thermal cycle. For this, two distinct models of convection were considered. The first model simulated the cooling of the sample as it entered the liquid nitrogen and made it possible to have an estimate of the time necessary for the sample to have a homogeneous temperature. It did not take into account phenomena such as the evaporation of nitrogen in contact with the relatively warmer sample. The second model allowed to estimate the time required for the sample to return to room temperature. The parameters used during these numerical simulations are listed in Table 3.2.

Table 3.2: Parameters used for the finite element simulation of the thermal cycle by convection of a cylindrical sample of simulant of 1cm diameter and 2 cm height

Temperature range	From 290 K to 77 K	From 77 K to 290 K
Conductivity <sup>1</sup> ( $W.m^{-1}.K^{-1}$ )	0.5	0.5
Density <sup>2</sup> ( $kg.m^{-3}$ )	1720	1720
Coefficient of heat transfer ( $W.m^{-2}.K^{-1}$ )	1539	15.7
Specific heat <sup>1</sup> ( $J.kg^{-1}.K^{-1}$ )	500	500

<sup>1</sup> : Opeil et al. (2010); Mir et al. (2019)

<sup>2</sup> : Measured on the samples

A natural convection model was used to compute the heat transfer coefficient at the surface of the sample. A natural (or free) convection means that the only motions in the system are caused by density variations resulting from temperature differences within the fluid. The heat transfer coefficient,  $h$ , is computed by dividing the heat flux  $q$  by the  $\Delta T$  between the solid surface and the surrounding fluid, or by dividing the fluid thermal conductivity  $k$  by the diameter of the sample and then multiplying it by the Nusselt number in order to take into account the convection as

well as the conduction (3.1).

$$h = q/\Delta T = Nu * k/D \quad (3.1)$$

The Nusselt number, Nu, is a dimensionless number. It is a function of the Rayleigh number and the Prandtl number. The formula depends on the geometry and is determined empirically (3.2 for a cylinder). It represents the enhancement of heat transfer through a fluid layer due to convection relative to conduction across the same fluid layer.

$$Nu = \left( \frac{0.60 + (0.387Ra^{1/6})}{[1 + (0.559/Pr)^{9/16}]^{8/27}} \right)^2 \quad (3.2)$$

The Prandtl number is also a dimensionless number indicating which of thermal diffusivity or thermal conduction is dominant (Equation 3.3). It is a thermal characteristic of the fluid.

$$Pr = \mu.C_p/k \quad (3.3)$$

Pr = Prandtl number

$\mu$  = Fluid viscosity

$C_p$  = Fluid specific heat

k = Fluid thermal conductivity

The Rayleigh number, Ra, is used to express heat transfer in natural convection (Equation 3.4). It is defined as the product of the Prandtl number and the Grashof number making also a dimensionless number. The magnitude of the Rayleigh number indicates whether the natural convection boundary layer is laminar or turbulent.

$$Ra = Gr.Pr = \frac{g.\beta.\rho^2.C_p.\Delta T.D^3}{k.\mu} \quad (3.4)$$

D = Diameter

$\rho$  = Fluid density

g = gravitational acceleration

$\Delta T$  = Temperature difference between the fluid and the cylinder

$\beta$  = Fluid thermal expansion coefficient

The Grashof number,  $Gr$ , is a dimensionless number defined as the ratio of the buoyant forces, which causes the motion, to a viscous force, which resist the motion (Equation [3.5](#)). The Grashof number is an indicator which quantifies these opposing forces.

$$Gr = \frac{g \cdot \beta \cdot \rho^2 \cdot \Delta T \cdot D^3}{\mu^2} \quad (3.5)$$

### 3.1.4 Samples preparation

These numerical simulations helped to determine the size and the shape of the sample to have a thermal cycle as short as possible. It was decided avoid as much as possible geometries that can induce stress concentrations (corners, etc.). This choice was made in order to observe if the potential cracks due to thermal cycling could only be caused by the microstructure or thermal gradient, that is to say by the difference in the coefficient of thermal expansion between the different phases of the material or the difference of thermal dilatation between the surface and the center of the sample. Indeed, if these two mechanisms alone explain the appearance of thermal fracturing, this would imply that this phenomenon could occur in any rock present on the surface of the asteroid, unlike cracks due to geometric factors.

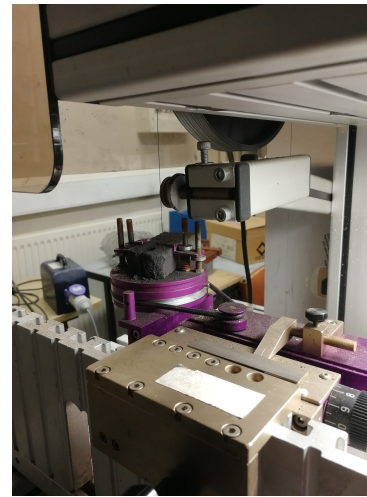
Taking this into account, the geometry allowing this constraint to be best respected would have been a sphere. However, the material being very weak and difficult to machine, it was decided to use a cylindrical specimen. in order to have a good scale separation between the microstructure and the sample while limiting as much as possible the time of the thermal cycles and therefore the size of the sample, a diameter of 10 mm for a height of 20 mm was chosen. Simulations performed for a sample of this size indicated a total cycle time of approximately 17 minutes with a homogeneous temperature within the sample in liquid nitrogen after 2 minutes and homogeneous in ambient air after 15 minutes.



These samples were machined from the blocks of simulant material produced by the Exolith Lab. These blocks were cut into 20 mm thick slices again using the wire saw (Figure 3.4a). In order to make the cylinders, a specific rotating plate was mounted on the wire saw (Figure 3.4b). This device (purple parts in Figure 3.4b) allowed to set the desired diameter and to rotate the slice of simulant material automatically until the cylinder is obtained.



(a) Cutting 20 mm thick slices with a wire saw

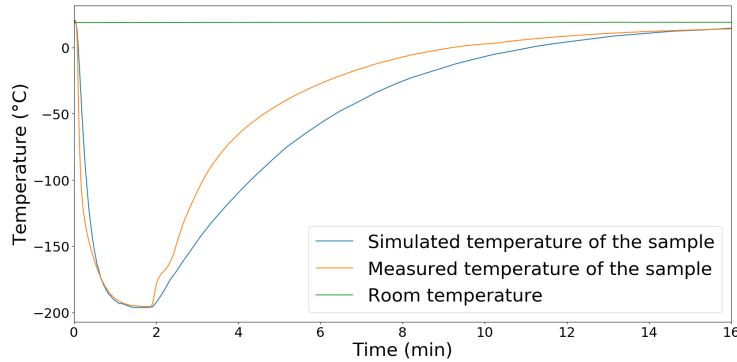


(b) Realization of the cylinders with a wire saw using an automatic rotation system

Figure 3.4: Machining of a sample for a thermal cycling test using a wire saw

In order to verify the results obtained by numerical simulation, tests were carried out by placing a thermocouple in the heart of the sample, as well as a second on its surface. This allowed to monitor the evolution of the temperature of the sample at the surface and in the core during its cycling. This setup also allowed to estimate thermal effect of different parameters such as the addition of the copper tube and the aluminum foil on the heating and cooling time. Although the numerical simulation did not take into account the layer of gaseous nitrogen formed around the sample after immersion and the presence of frost, the experimental results were shown to be consistent with the numerical results (Figure 3.5).

Figure 3.5: Monitoring sample temperature during a thermal cycle



### 3.1.5 Image analysis

Once the sample was finalized, a first scan was carried out with an X-ray CT-scanner in order to know the initial state of the microstructure. This first scan was then used as a reference point throughout the test. During each scan (reference or intermediate scan), after the reconstruction, a three-dimensional gray-scale image of the specimen was obtained with a resolution of approximately  $8\ \mu\text{m}$  per pixel. The sample having a height of 2 cm, it was cut into approximately 2900 gray-scale 2D-images of  $1500 \times 1500$  pixels called slices. These slices were then converted into a three-dimensional image in .TIFF format so as not to lose any information. From these images, the complete volume of the sample could be reconstructed (Figure 3.6). This step was performed using ImageJ software (Fiji).

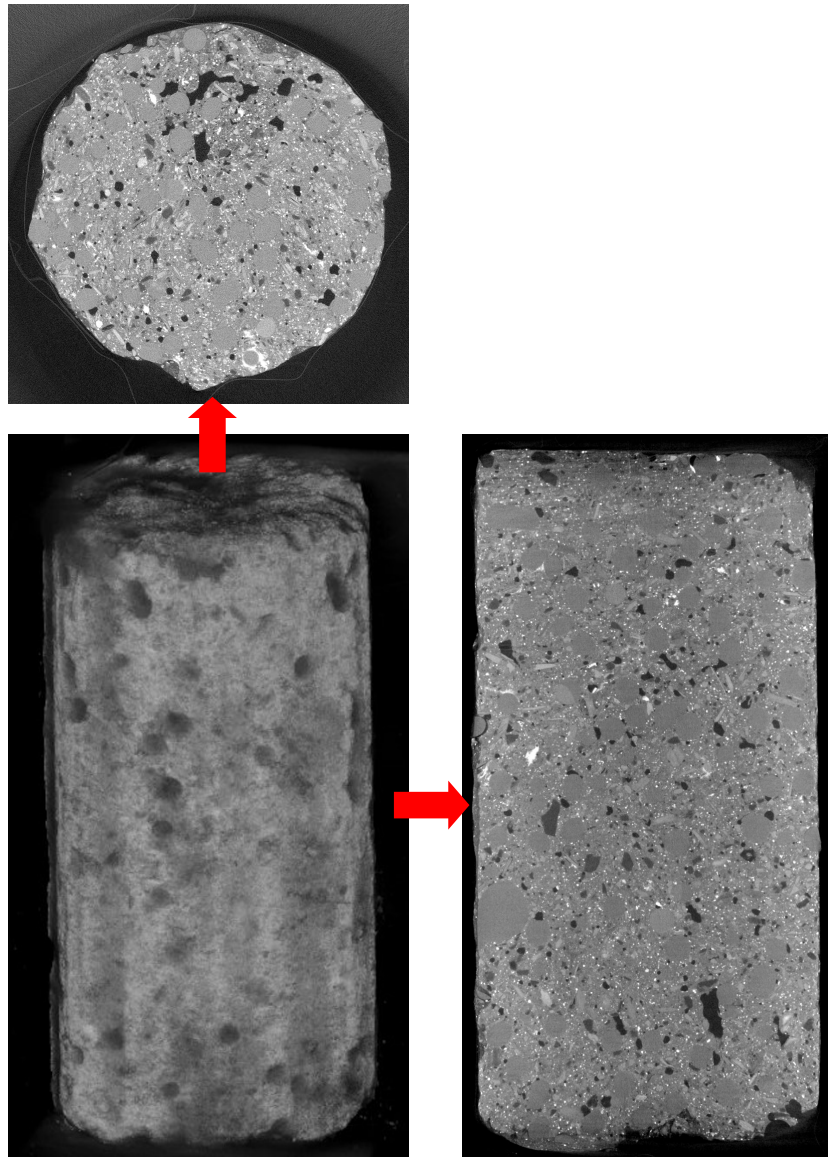


Figure 3.6: Volume reconstruction and cross-section views of a sample scanned by X-ray tomography

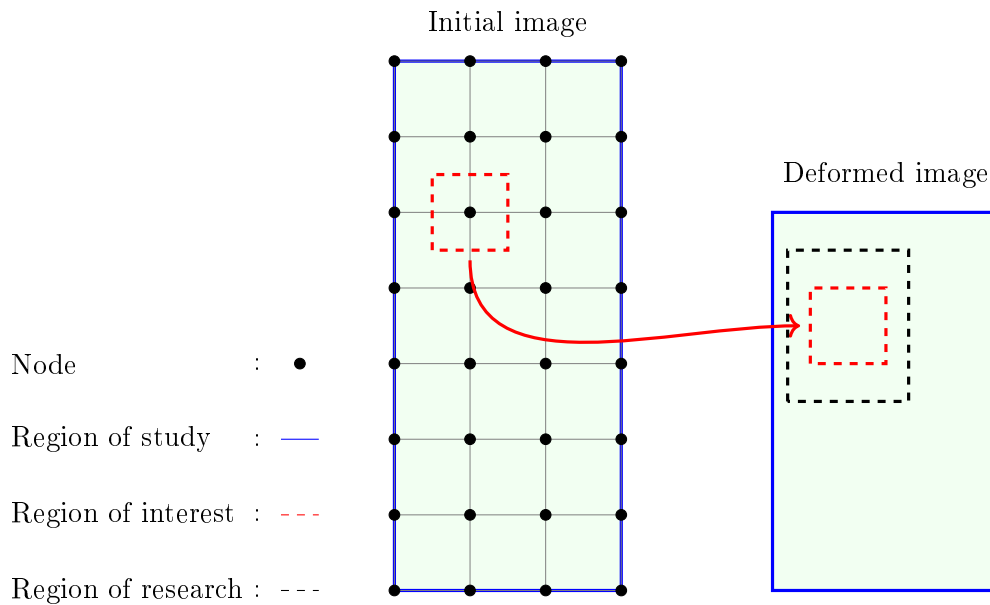
The samples were then subjected to thermal cycling and scanned after a certain amount of cycles as detailed in Table [3.1](#). These scans were then compared in order to observe deformations or cracks.

To be able to compare these different scans, the rigid-body motion was computed. Indeed,

the samples being placed by hand in the X-ray CT-scanner, they could not be placed exactly at the same location from one scan to another. This realignment of the images, called registration was done with the help of the SPAM code developed at the 3SR laboratory in Grenoble by Stamati et al. (2020).

The displacement and strain fields were calculated using the local digital image correlation (DIC) code SPAM (Stamati et al., 2020). For this, a reduction by half of the number of voxels in each direction called a "bin 2" was applied to the 3D images of the sample. This had the advantage of greatly reducing the computation time and of reducing the noise present induced by the scan in the images, which allowed the algorithm to converge more easily.

Figure 3.7: Schematization of local digital image correlation



To carry out these analyses, the region of study (ROS) of the image was meshed (Figure 3.7). The mesh used by SPAM was cubic with the ability to vary the distance between nodes in each direction. A mesh size of 20 voxels, identical in the 3 directions (x,y,z) was determined empirically. This allowed a fine mesh, while allowing convergence over the entire sample, which was not the case for a finer mesh which had difficulty converging at the level of inclusions due

to the lack of texture of these.

Each of these nodes was associated with a region of interest (ROI) which was a small part of the initial image and whose center was the node of the mesh (Figure 3.7). The dimensions of these ROI's were configurable. The algorithm then searched for this same ROI in the region of research in the deformed image (Figure 3.7).

To do this, an affine transformation following equation 3.6 was assumed. Solving equation 3.6 implies finding the linear transform tensor  $\mathbf{F}$  and the translation vector  $\mathbf{T}$  such that the difference between the deformed ROI ( $\mathbf{X}'$ ) and the initial ROI ( $\mathbf{X}$ ) was minimum. In order to facilitate its resolution, it was possible to express the equation in the form presented in equation 3.7. This allowed to display the transformation matrix  $\boldsymbol{\theta}$  built from the transformation gradient tensor  $\mathbf{F}$  which took rotations into account and the translation vector  $\mathbf{T}$ . It was this transformation matrix  $\boldsymbol{\theta}$  which was sought by the algorithm.

$$\mathbf{X}' = \mathbf{F}\mathbf{X} + \mathbf{T} \quad (3.6)$$

$$\begin{pmatrix} X'_z \\ X'_y \\ X'_x \\ 1 \end{pmatrix} = \underbrace{\begin{pmatrix} F_{zz} & F_{zy} & F_{zx} & T_z \\ F_{yz} & F_{yy} & F_{yx} & T_y \\ F_{xz} & F_{xy} & F_{xx} & T_x \\ 0 & 0 & 0 & 1 \end{pmatrix}}_{\boldsymbol{\theta}} \begin{pmatrix} X_z \\ X_y \\ X_x \\ 1 \end{pmatrix} \quad (3.7)$$

These matrices  $\boldsymbol{\theta}$  were sought to minimize the error function defined as being the differences for each ROI's between the average gray level  $\bar{G}$  of the initial image and the deformed image (Equation 3.8).

$$\tau(\boldsymbol{\theta}) = \sum_{x \in ROI} (\bar{G}_{Initial}(x) - \bar{G}_{Deformed}(\boldsymbol{\theta}.x))^2 \quad (3.8)$$

with  $x$  a position vector

In the SPAM calculation code, this step was carried out by iteration using Newton's method.

In order to facilitate the convergence of the algorithm, a visual correction of the rigid body motion (which will be mentioned below as "registration" to be consistent with SPAM's documentation) was performed by performing rigid displacements (translation and rotation) of our scan along the x, y and z axes in order to superimpose it as well as possible with the reference scan. This allowed to obtain a single transformation matrix  $\theta$  for the whole image. This matrix was then used as an initial guess to make a second registration, this time calculated with the DIC method presented previously with a single node and a region of interest equal to the study region. This second registration allowed to carry out an off-plane adjustment and also includes a first estimation of the deformation of a sample through the determination of a linear transform matrix  $\theta$  covering the whole 3D image and thus to improve the registration carried out visually.

Once the registration determined, it was possible to apply these transformations to the scan and therefore to compare the images. The comparison of the images after registration allowed to highlight the most obvious transformations easily for a relatively low calculation time.

After running the DIC calculation (providing the displacement field  $\mathbf{U}$ ) and the registration (fast DIC calculation with an ROI covering the whole ROS providing the displacement field  $\mathbf{U}_{Registration}$  corresponding to the rigid body motion) it is possible to compute a displacement  $\mathbf{U}_{Filtered}$  based on equation [3.9](#) with  $\mathbf{U}$  the displacement between the initial position  $\mathbf{X}$  and the deformed position  $\mathbf{X}'$  (Equation [3.10](#)).  $\mathbf{U}_{Filtered}$  corresponds solely to the deformation of the sample at zero stress between two cycles. It is small (on the order of 0.5 voxel).

$$\mathbf{U}_{Filtered} = \mathbf{U} - \mathbf{U}_{Registration} \quad (3.9)$$

$$\mathbf{U} = \mathbf{X}' - \mathbf{X} \quad (3.10)$$

$\mathbf{U}_{Filtered}$  being small, the strain field was calculated using the infinitesimal strain tensor defined by equation [3.11](#) was used.

$$\mathbf{E} = \frac{1}{2}[\mathbf{Grad}(\mathbf{U}) + (\mathbf{Grad}(\mathbf{U}))^T] \quad (3.11)$$

The first two invariants of the strain tensor which are the volumetric strain and the deviatoric strain were also calculated. The first makes it possible to highlight the variations of the volume while the second quantifies the shear strain of the material. The volumetric strain is the trace of the strain tensor (Equation [3.12](#)).

$$\mathbf{E}_{vol} = tr(\mathbf{E}) = E_{xx} + E_{yy} + E_{zz} \quad (3.12)$$

In order to determine the deviatoric strain, it is initially necessary to calculate the deviatoric strain tensor which is defined by Equation [3.13](#).

$$\mathbf{E}_{dev} = \mathbf{E} - \mathbf{E}_{Hydro} = \mathbf{E} - (E_{vol}/3)\mathbf{I} \quad (3.13)$$

with  $\mathbf{I}$  the identity matrix

The deviatoric strain is then the norm of the deviatoric tensor.

$$\|\mathbf{E}_{dev}\| = \sqrt{\sum a_{ij}^2} \quad (3.14)$$

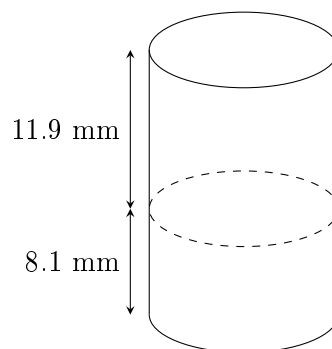
with  $a_{ij}$  the components of the deviatoric strain tensor  $\mathbf{E}_{dev}$ .

By applying the calculated displacement field to the initial image, it was possible to compare it to the deformed image and thus obtain a residual field. This residual field allowed, thanks to a finer adjustment, to observe phenomena that were difficult to see after a simple registration. However, obtaining this residual field was much more computationally heavy. For this reason, the residual field was not calculated for all the images but only the ones which were considered the most relevant. For other images, the subtraction between the original and registered image was used.

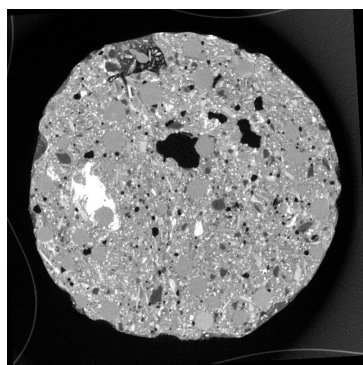
## 3.2 Results

In a first step, the more obvious differences were observed by subtracting the registered image from the original image. This technique being very fast, it allowed to identify the zones mostly affected by thermal cycling in a quick and efficient manner. In order to compare the images, ImageJ software was used. By analyzing the images of the different tests, several phenomena have been observed.

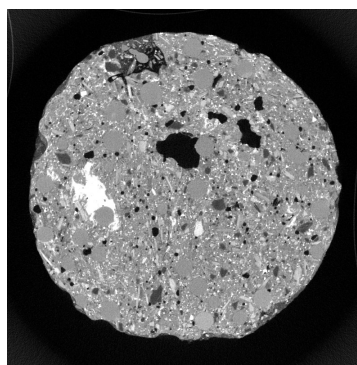
On the first of the two samples tested, there was a large pore located close to the surface. We see in the images below (Figure 3.8), a motion of the particles filling up the surface porosity during the first thermal cycles. Gradually this area has eroded until it opens completely after 400 cycles.



(a) Position of the slice 860



(b) 70 cycles



(c) 0 cycles



(d) Differences after 70 cycles



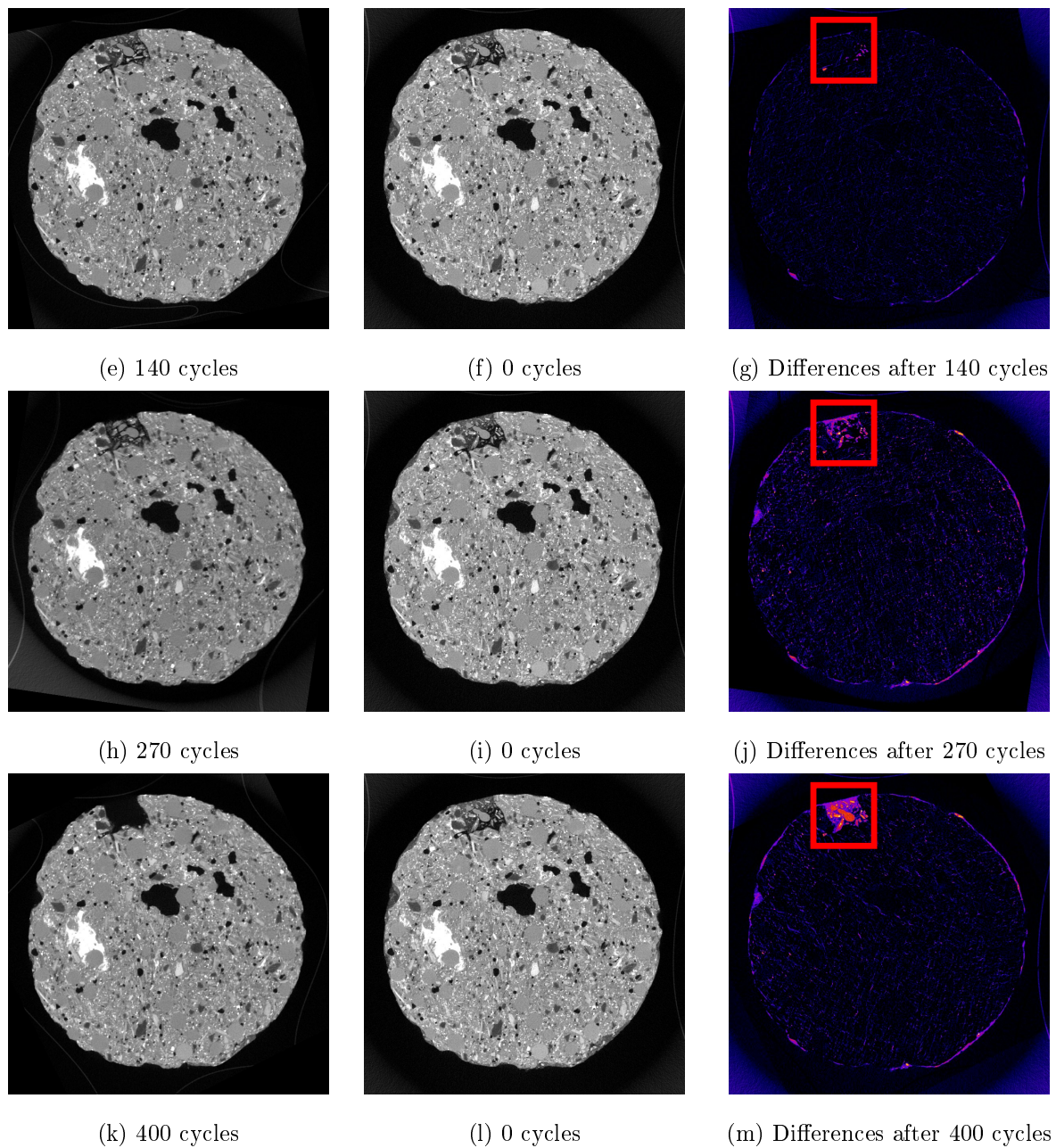
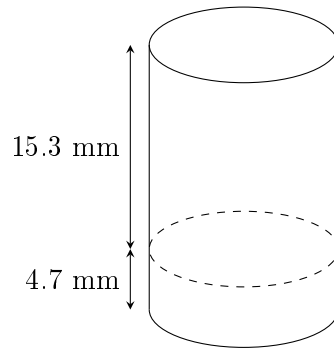


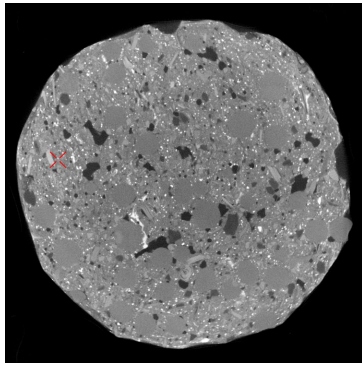
Figure 3.8: View of slice 860 of sample No.1: Evolution of the opening of an inclusion through thermal cycling

A more general erosion (I) over the entire surface was also observed on both samples. This erosion was coupled with a detachment of certain surface inclusions (II) as well. It was found

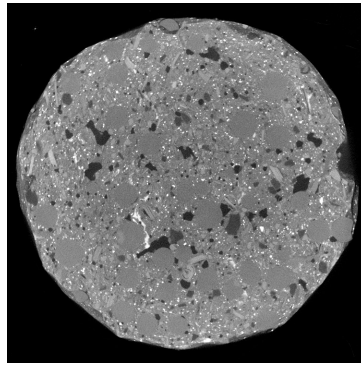
that these phenomena increased with the number of cycles (Figure 3.9).



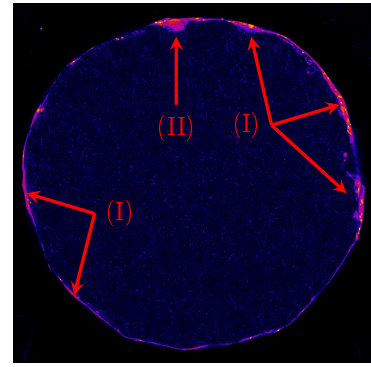
(a) Position of the slice 1110



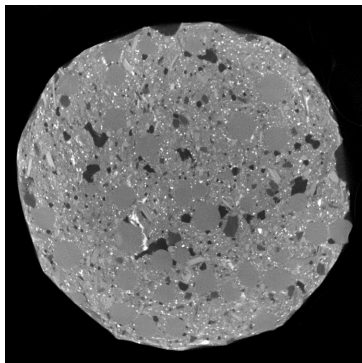
(b) 97 cycles



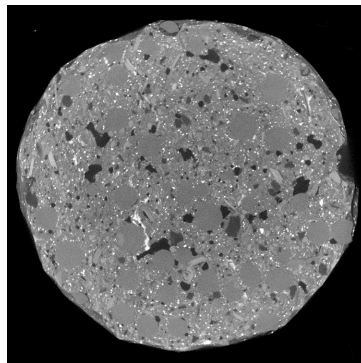
(c) 0 cycles



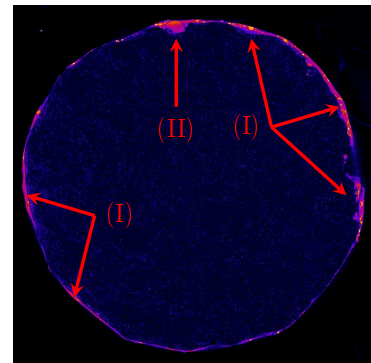
(d) Differences after 97 cycles



(e) 215 cycles



(f) 0 cycles



(g) Differences after 215 cycles

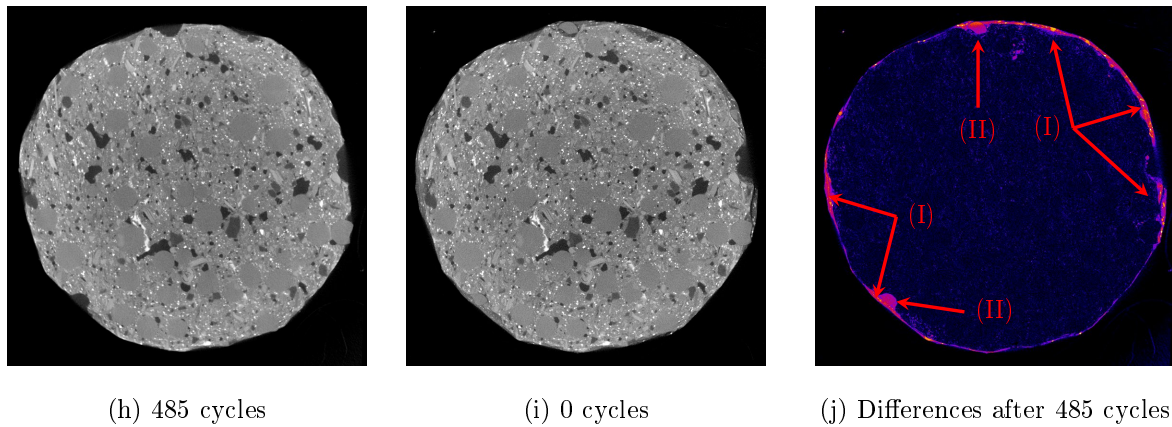
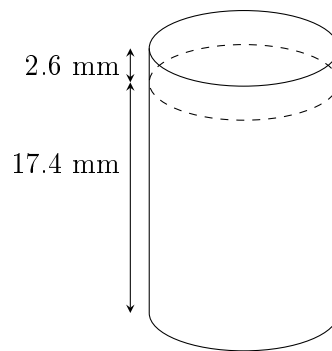


Figure 3.9: View of slice 1110 of sample No.2: Evolution of erosion and inclusion shedding through thermal cycling

When the number of thermal cycles increased, an other phenomenon appeared. Cracks were visible on the images of the second sample after 485 cycles. As Figure [3.10](#) showed, these cracks were present in the center of the material, unlike the previous phenomena which were mainly concentrated on the surface. On these images, the detachment of inclusions (I), a phenomenon already mentioned previously, was also visible but this time in the core of the sample.



(a) Position of the slice 185

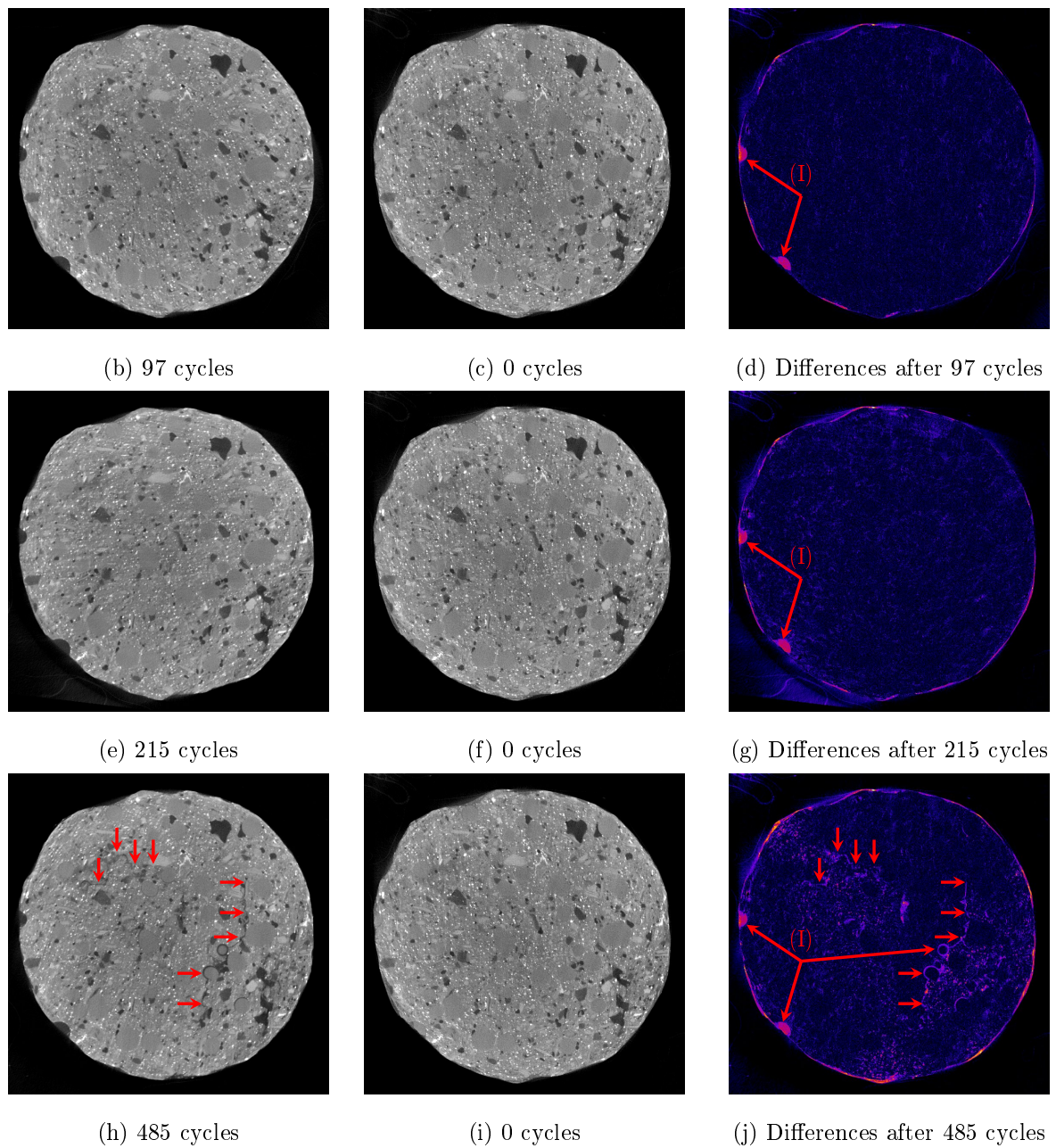


Figure 3.10: View of slice 185 of sample No.2: Evolution of cracking through thermal cycling

In a vertical diametral cross-section, it can be seen that the crack spreads over almost the whole width of the sample in Figure [3.11f](#). In addition, a large part of the material was also detached from the rest of the first sample after 270 cycles (Figure [3.11c](#)).

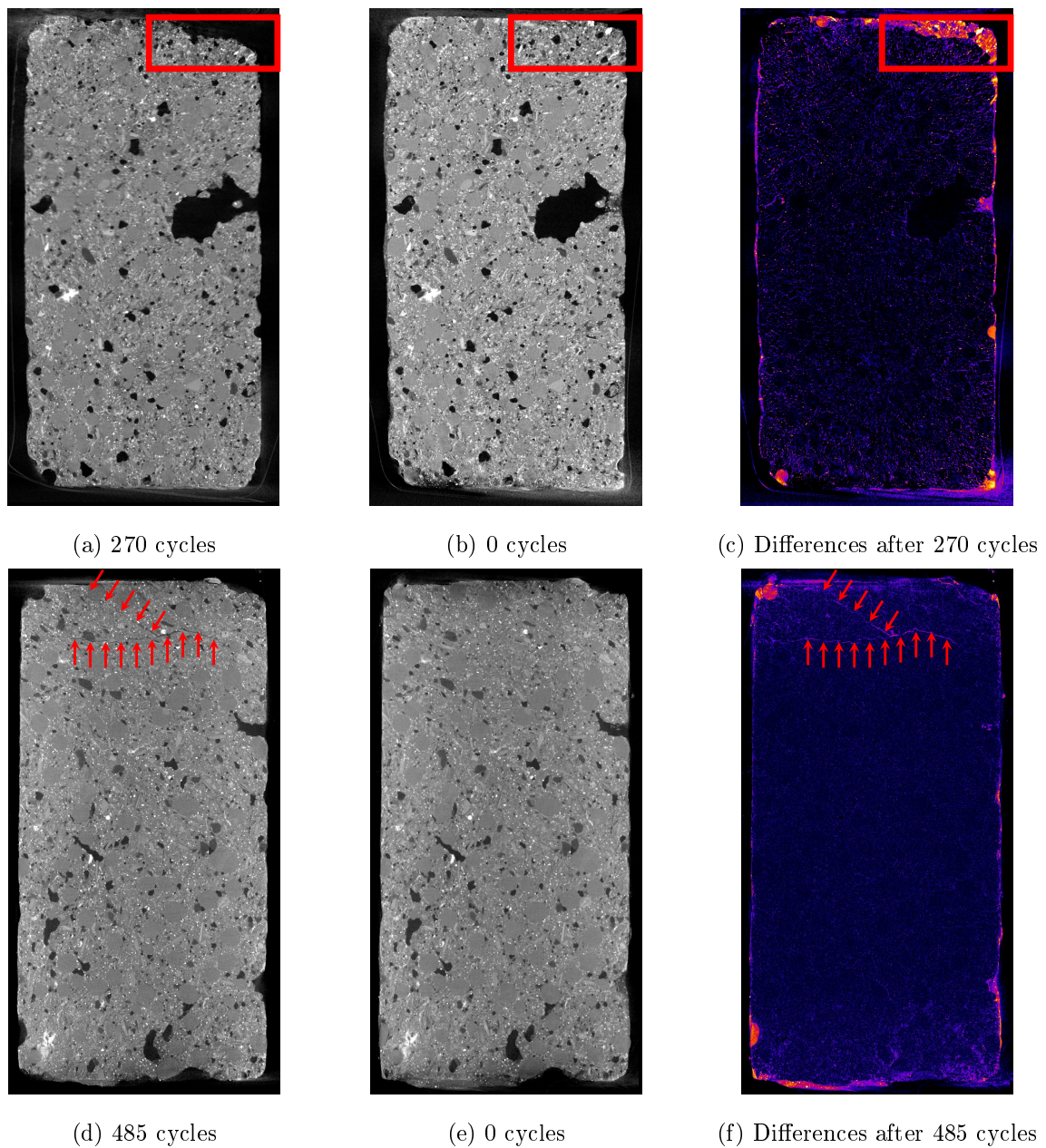
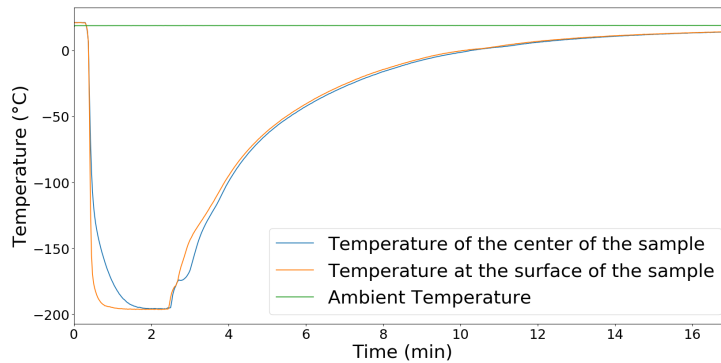


Figure 3.11: Vertical section views of samples: observation of cracking

Note that after a small number of thermal cycles (the first 200 cycles), the damage to the sample was mainly concentrated on the outer boundary and around the inclusions. This could be explained for several reasons. First, it is possible that the thermal gradient undergone by

the sample during the transitory periods of the cycles favored the appearance of cracks in these zones. Indeed, we can see in Figure 3.12 that the temperature difference between the center and the surface of the sample when entering the nitrogen could exceed 100 K.

Figure 3.12: Monitoring sample temperature during a thermal cycle



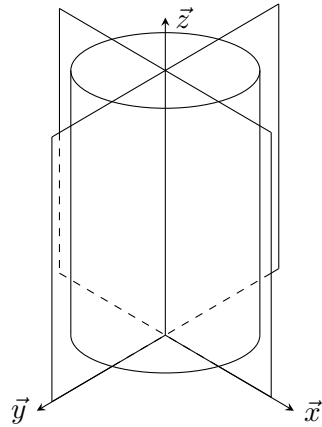
Secondly, the surface may have been damaged during the manipulation or the machining process, which would have facilitated the propagation of cracks in this zone and therefore its erosion. Finally, the detachment of certain inclusions could be explained by a difference in the coefficient of thermal expansion between the matrix of the sample mainly composed of serpentine (in our case of antigorite) and the glass inclusions.

After a greater number of cycles, one noticed the appearance of cracks crossing the sample. These cracks did not cross the inclusions and seemed to circumvent the different phases present within the material and have led to the breakage of a part of the sample as seen in figure 3.11.

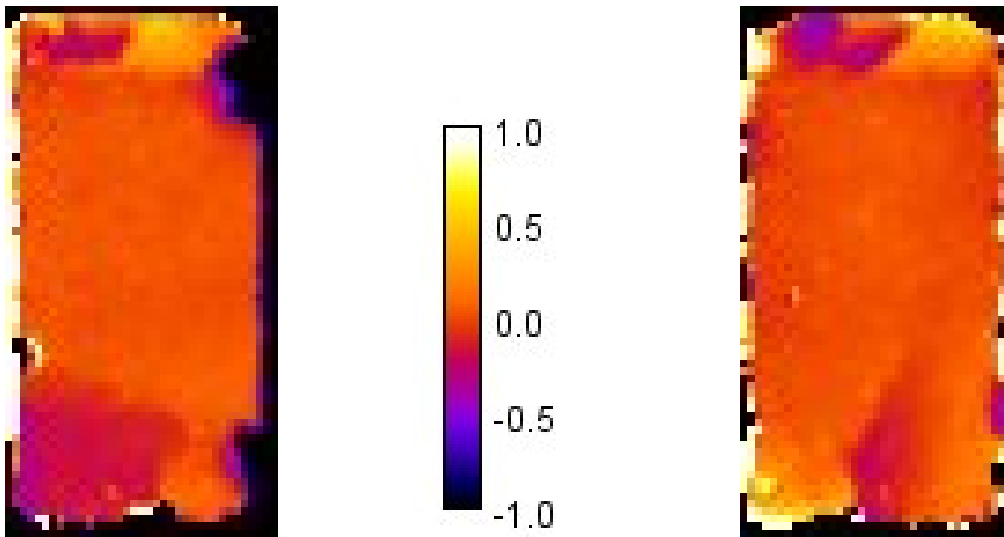
This first analysis underlined different processes undergone by the material during thermal cycling. This tended to show that the thermal fracturing process indeed existed in this type of material and could therefore be partly responsible for the creation of the regolith on the surface of CM-type asteroids.

Despite highlighting different phenomena, the study by image comparison carried out previously only allows observing clear and open cracks. In order to detect other cracks, a second study was carried out.

In Figure 3.13, the displacement field subtracted from the rigid body displacement is shown. We see that the displacements were particularly small within the material, with values rarely exceeding 1 pixel, which was equivalent to  $16\mu\text{m}$ . A large discontinuity in the displacement field was observed at the top of the sample. This discontinuity was the indication of a crack at this location, which was consistent with what has been observed before (Figure 3.11f). It can also be noted that a second discontinuity on the cross-section view normal to the Y axis, this time less obvious, crossed the bottom of the sample. The discontinuities in the displacement field indicated the development of cracks, as will be shown below. The same phenomenon was observed on the cross-section view normal to the X axis where a discontinuity was also visible at the bottom of the sample. This discontinuity seemed to divide into two distinct branches.



(a) Position of the orthonormal frame

(b) Displacement along the  $\vec{z}$  axis on the cross-section view normal to the Y axis

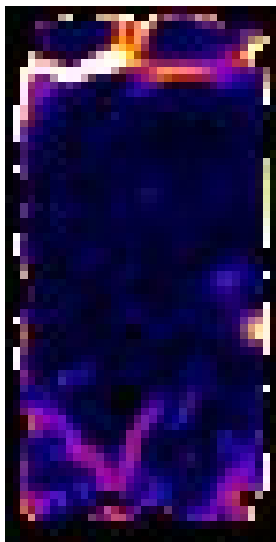
(c) Displacement scale in pixels

(d) Displacement along the  $\vec{z}$  axis on the cross-section view normal to the X axis

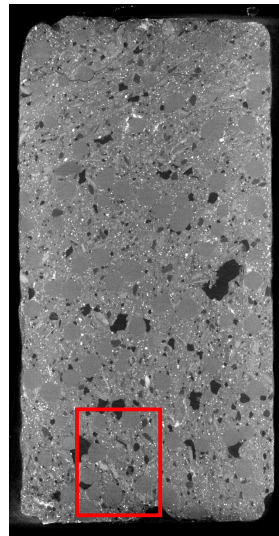
Figure 3.13: Displacement field of the sample No.2 after 485 cycles

Comparing Figure 3.13d with Figure 3.14a and Figure 3.13b with Figure 3.14d, it was possible to observe that the localization of the deviatoric strain corresponds to the discontinuities in the displacement field.

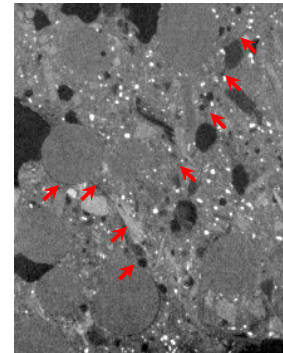




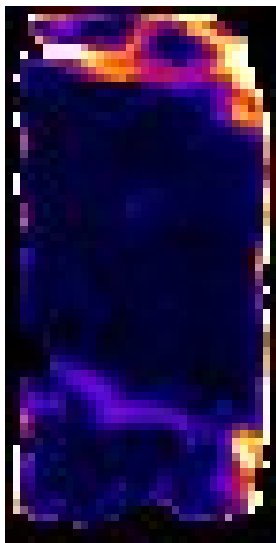
(a) Deviatoric strain on the cross-section view normal to the X axis



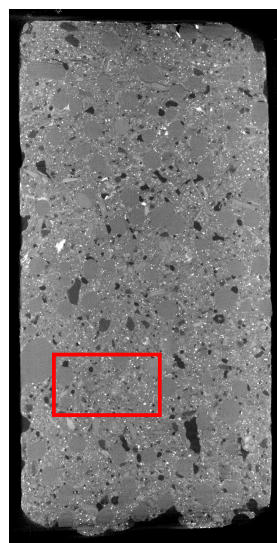
(b) Cross-section view normal to the X axis of the sample after 485 cycles



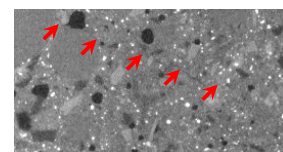
(c) Zoom of the cracks on the framed area



(d) Deviatoric strain on the cross-section view normal to the Y axis



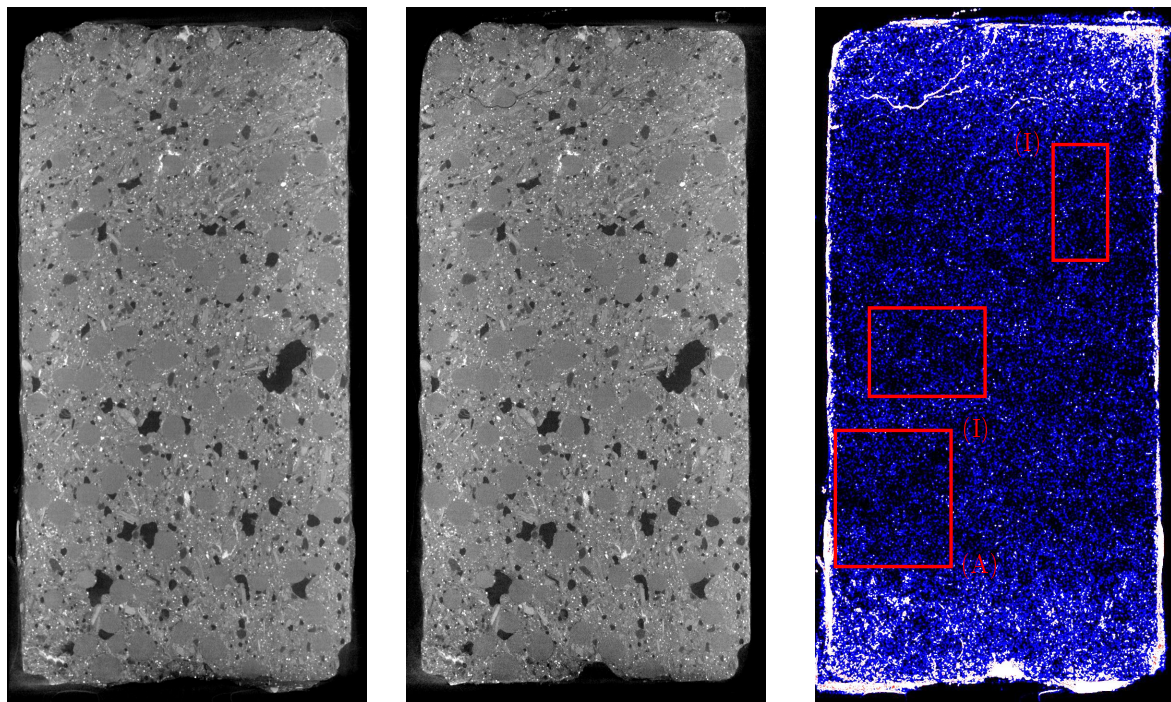
(e) Cross-section view normal to the Y axis of the sample after 485 cycles



(f) Zoom of the cracks on the framed area

Figure 3.14: Demonstration of thermal crack using strain fields

Looking at the images of the samples after 485 cycles in these areas, some small cracks can be seen (Figure 3.14b, 3.14c and 3.14e, 3.14f) at the places where the discontinuities were observed. The detection of these cracks on a single image was difficult because of their small aperture. However, they became more obvious when sweeping across multiple slices.



(a) Initial state

(b) 485 cycles

(c) Gray level residual field on the cross-section view normal to the X axis

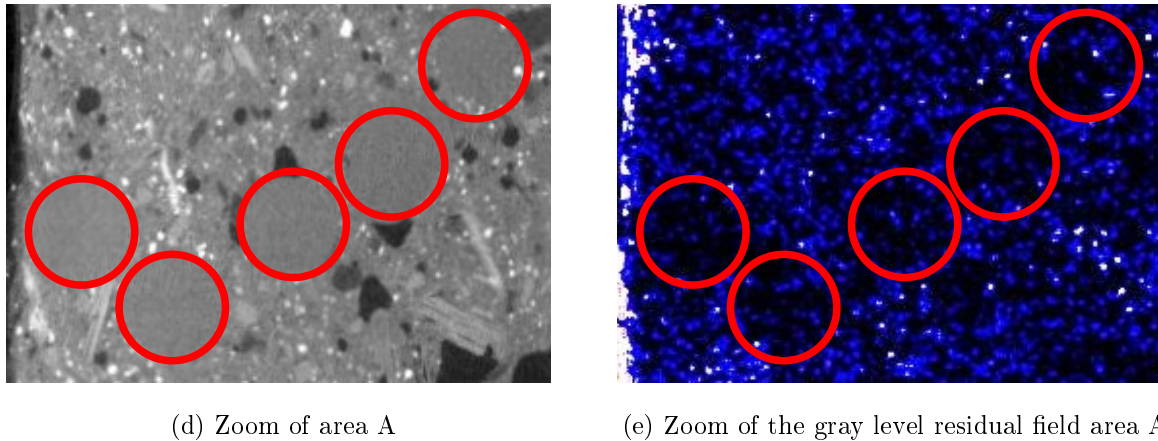


Figure 3.15: Gray level residual field after 485 cycles (test n°2)

An image of the sample in its initial state has been deformed according to the homogenized displacement field at the ROI scale calculated previously in order to compare it with the image of the real deformed sample after 485 cycles and thus to obtain a residual gray level field. This allowed to highlight the local singularities of the displacement at a lower scale than the resolution of the DIC.

The detection of the least open cracks was not obvious on the Figure 3.15. However we noticed that the residual field was significantly larger in the lower and upper parts of the sample, which seemed to indicate an area in which damage at a lower scale than the resolution of the image would be concentrated. This could be caused by the thermal gradient experienced during transient periods of thermal cycling. Although, a change in the gray scale residual field around the inclusions (I) was observed which shows that the difference in coefficient of thermal expansion could also have played a role in the thermal cracking of the material. However, these images did not provide information on the kinetics of crack growth and on crack initiation zones. To this purpose, a much more ambitious study with many more scans is required, which was not possible in the present work.

### 3.3 Conclusion

The study of the images from the X-ray tomography showed surface erosion of the samples over the first 200 cycles, probably favored by a weakening of this zone during machining. The detachment of some inclusions and the opening of the largest porosities were also observed. After 400 cycles, thermal cracks are observed in several places. A more in-depth study of these images by digital image correlation (DIC) allowed to discover new cracks in formation but also to identify zones in which the damage concentration is greater. It is in these zones that all the cracks observed were created. These areas are found in the upper and lower boundary regions of the samples.

These results tend to prove the possibility for the regolith to have originated partly from thermal fracturing. However, these results should be interpreted with caution. Indeed, asteroids are airless bodies. In this study, the tests were carried out under terrestrial atmospheric conditions. Although great efforts have been made to limit the role of humidity as much as possible, tests carried out in close-to-vacuum conditions would be more realistic and would eliminate this doubt.

Moreover, it has been shown in Section [1.5](#) that a large part of the material's porosity is found at a scale lower than the resolution of the images produced. It is likely that nano-cracking phenomena occur at these scales. However, the means at our disposal do not allow us to verify this hypothesis.

## Chapter 4

# General conclusion

The study of primitive asteroids and the regolith present on their surface represents a challenge for the scientific community. Learning more about the mechanical characteristics of the surface rocks of these asteroids and the phenomena involved in the creation of the regolith could not only allow us to learn more about the first moments of our solar system, but also have a large number of applications for future space missions.

Unfortunately, there is little material available on Earth to carry out these studies. Indeed, the majority of CM-type asteroids, studied in this document, are pulverized during their entry into the atmosphere. The samples brought back to Earth by space missions such as Hayabusa 2 are mainly made up of dust and small rocks that do not provide samples which are large enough to carry out mechanical tests which require samples of the order of cm. Furthermore, the fragments being small, it is probable that they are not large enough in relation to the microstructure to be considered as being a representative elementary volume. It is possible to carry out tests on meteorites, thanks to which the literature provide a wealth of information about, such as on the composition or the microstructure of asteroids.

However, observations have highlighted large differences between the results of mechanical tests obtained on meteorites and the estimates observed on asteroids (Popova et al., 2011). These estimates suggest that asteroidal rock is probably much weaker than meteorites found on Earth.

---

This can be explained by their travel through the Earth's atmosphere, during which the weakest elements disappear and the remnants have suffered a severe heat-treatment.

It is in this context that the Exolith Lab has UCF developed a simulant material, based mainly on the petrological composition.

The mineral composition of this material is well controlled but its thermomechanical properties and their relation to the process remain largely unknown. Therefore, it was necessary to carry out a large number of preliminary tests, both for mechanical tests and thermal cycling tests, in order to converge towards experimental processes allowing the realization of the tests presented in this document.

According to the results obtained during the tensile and compression tests the 27% porosity simulant has a Young's modulus of 1 GPA and a tensile strength of 250 kPa. These results are consistent with observations and estimates found in the literature (Popova et al., 2011). Tests on the 50% porosity simulant have highlighted the influence of porosity on the mechanical characteristics of this material and the importance of controlling it precisely during the manufacturing process. With regard to the thermal cycling test, the use of X-ray  $\mu$ CT scans allowed to follow the evolution of the microstructure of the material throughout the test. It was possible to observe surface erosion of the samples during the first 200 cycles before observing the formation of thermal cracks after approximately 400 cycles. These results are consistent with the study conducted by Delbo et al. (2014). However, the study by Delbo et al. (2014) was based on a meteorite already presenting cracks. Propagation of pre-existing cracks was observed after a certain number of cycles. Also, the detachment of some fragments located close to the outer boundary was noticed close to corners or geometrical singularities which usually favor stress concentrations. This new study revealed the appearance of thermal fracturing on a material cracks induced by thermal cycling in the core of samples of a material which was initially intact without prior damage or geometry facilitating the appearance of this phenomenon.

# Recommendations

This study has made it possible to learn more about this exotic material. However, many questions still remain unanswered and there is still a lot to discover.

Regarding the mechanical characterization, it would be interesting to carry out tests in conditions closer to reality in order to limit the influence of ambient humidity for example. The material being manufactured, the study of the repeatability of the process and the possible dispersion of the results would allow to have more hindsight and certainties. In addition, the surface of asteroids being subject to strong temperature variations, studying the influence of this temperature on the mechanical behavior of the material by carrying out tests on different temperature ranges seems to be important. Finally, the study of the phenomenon observed during bonding via creep tests, for example, could also prove to be very useful for a better understanding of the material.

For the thermal tests humidity could also play a role and it would be interesting to be able to carry out these tests in a controlled humidity environment or even in conditions close to vacuum. Performing more regular scans with an X-ray CT-scanner could also allow cracks to be monitored and thus give the possibility of estimating the rate of advancement of the cracks. Finally, the thermal cycling experiment could be improved by developing a system to limit or even completely avoid damage caused by the handling of the sample by carrying out the tests directly within an X-ray tomograph or by placing the sample in a removable cell allowing the scanning of the sample directly in the cell.





# Bibliography

- Amelin et al. (2002). “Lead isotopic ages of chondrules and calcium-aluminum-rich inclusions”.  
In: *Science* 297(5587), pp. 1678–1683.
- Ashworth (1978). “Lunar and planetary impact erosion.” In: *Cosmic Dust*, pp. 427–526.
- Avdellidou et al. (2019a). “Hypervelocity impacts on carbonaceous asteroids analogue materials”.  
In: *EPSC-DPS joint Meeting 2019*.
- Avdellidou et al. (2019b). “Mechanical properties of very weak carbonaceous asteroid analogues and response to hypervelocity impacts”. In: *Icarus*.
- Avdellidou et al. (2020). “Very weak carbonaceous asteroid simulants I: Mechanical properties and response to hypervelocity impacts”. In: *Icarus* 341, p. 113648.
- Battandier (2018). “Etude d’une série de micrométéorites antarctiques: caractérisation multi-analytique et comparaison à des chondrites carbonées”. PhD thesis. Université Grenoble Alpes (ComUE).
- Blum and Wurm (2000). “Experiments on sticking, restructuring, and fragmentation of preplanetary dust aggregates”. In: *Icarus* 143(1), pp. 138–146.
- Blum et al. (2006). “The physics of protoplanetary dust agglomerates. I. Mechanical properties and relations to primitive bodies in the solar system”. In: *The Astrophysical Journal* 652(2), p. 1768.
- Bottke Jr, William F et al. (1994). “Velocity distributions among colliding asteroids”. In: *Icarus* 107(2), pp. 255–268.

- Bouvier and Wadhwa (2010). “The age of the Solar System redefined by the oldest Pb–Pb age of a meteoritic inclusion”. In: *Nature geoscience* 3(9), pp. 637–641.
- Britt and Consolmagno (2000). “The porosity of dark meteorites and the structure of low-albedo asteroids”. In: *Icarus* 146(1), pp. 213–219.
- Britt, R Macke, and G Consolmagno (2010). “The Density, Porosity, and Structure of Very Small Bodies”. In: *European Planetary Science Congress*, pp. 863–863.
- Britt et al. (2019). “Simulated asteroid materials based on carbonaceous chondrite mineralogies”. In: *Meteoritics & Planetary Science* 54(9), pp. 2067–2082.
- Brownlee et al. (2006). “Comet 81P/Wild 2 under a microscope”. In: *science* 314(5806), pp. 1711–1716.
- Caffe et al. (1987). “Evidence in meteorites for an active early sun”. In: *The Astrophysical Journal* 313, pp. L31–L35.
- Cameron (1962). “Formation of the solar nebula”. In: *Icarus* 1(1-6), pp. 339–342.
- Cameron and Truran (1977). “The supernova trigger for formation of the solar system”. In: *Icarus* 30(3), pp. 447–461.
- Campbell-Brown (2019). “Meteoroid structure and fragmentation”. In: *Planetary and Space Science* 169, pp. 1–7.
- Dallas et al. (2020). “Mining beyond earth for sustainable development: Will humanity benefit from resource extraction in outer space?” In: *Acta Astronautica* 167, pp. 181–188.
- Delbo et al. (2014). “Thermal fatigue as the origin of regolith on small asteroids”. In: *Nature* 508(7495), pp. 233–236.
- Delbo et al. (2015). *Asteroid thermophysical modeling*. University of Arizona Press Tucson, Arizona.
- Grott et al. (2019). “Low thermal conductivity boulder with high porosity identified on C-type asteroid (162173) Ryugu”. In: *Nature Astronomy* 3(11), pp. 971–976.
- Hazeli et al. (2018). “The origins of Asteroidal rock disaggregation: Interplay of thermal fatigue and microstructure”. In: *Icarus* 304, pp. 172–182.

- Hérique et al. (2018). “Direct observations of asteroid interior and regolith structure: science measurement requirements”. In: *Advances in Space Research* 62(8), pp. 2141–2162.
- Hiramatsu and Oka (1966). “Determination of the tensile strength of rock by a compression test of an irregular test piece”. In: *International Journal of Rock Mechanics and Mining Sciences & Geomechanics Abstracts*. Vol. 3. 2. Elsevier, pp. 89–90.
- Hogan et al. (2015). “Dynamic brittle fragmentation: Probing the byproducts of hypervelocity impact in space”. In: *Procedia Engineering* 103, pp. 205–212.
- Ibrahim (2012). “The elastic properties of carbonaceous chondrites”. MA thesis. Graduate Studies.
- Jones and Scott (1996). *Chondrules and the Protoplanetary Disk*. Cambridge University Press.
- Jones et al. (2000). “Formation of chondrules and CAIs: Theory vs. observation”. In: *Protostars and planets IV* 927, p. 962.
- Kita et al. (2005). *Constraints on the origin of chondrules and CAIs from short-lived and long-lived radionuclides*. Tech. rep. Lawrence Livermore National Lab.(LLNL), Livermore, CA (United States).
- Krot et al. (2005). “Evolution of oxygen isotopic composition in the inner solar nebula”. In: *The Astrophysical Journal* 622(2), p. 1333.
- Lauretta et al. (2019). “Episodes of particle ejection from the surface of the active asteroid (101955) Bennu”. In: *Science* 366(6470).
- Lifeng (2021). *The condensation theory*. <https://lifeng.lamost.org/courses/astrotoday/CHAISSON/AT315/HTML/AT31502.HTM>, Last accessed on the 2021-10-25.
- Macke, Daniel T Britt, and Guy J Consolmagno SJ (2010). “Analysis of systematic error in “bead method” measurements of meteorite bulk volume and density”. In: *Planetary and Space Science* 58(3), pp. 421–426.
- Macke, Guy J Consolmagno, and Daniel T Britt (2011). “Density, porosity, and magnetic susceptibility of carbonaceous chondrites”. In: *Meteoritics & Planetary Science* 46(12), pp. 1842–1862.

- MacPherson (2003). “Calcium-aluminum-rich inclusions in chondritic meteorites”. In: *Treatise on Geochemistry* 1, p. 711.
- MacPherson and Russell (1997). “Origin of aluminum-rich chondrules: constraints from major-element chemistry”. In: *Meteoritics and Planetary Science Supplement* 32.
- Marcus (1973). “Production of lunar fragmental material by meteoroid impact”. In: *Icarus* 18(4), pp. 621–633.
- McSween Jr and Patchen (1989). “Pyroxene thermobarometry in LL-group chondrites and implications for parent body metamorphism”. In: *Meteoritics* 24(4), pp. 219–226.
- Meurisse et al. (2018). “Solar 3D printing of lunar regolith”. In: *Acta Astronautica* 152, pp. 800–810.
- Mir, El, KT Ramesh, and Marco Delbo (2019). “The efficiency of thermal fatigue in regolith generation on small airless bodies”. In: *Icarus* 333, pp. 356–370.
- Miura et al. (2008). “Compressive strength measurements of meteorites and terrestrial rocks: implications for physical properties of asteroidal surfaces”. In: *Proceedings of the Japan Geoscience Union Meeting, (P168-P002)*.
- Molaro et al. (2020). “In situ evidence of thermally induced rock breakdown widespread on Bennu’s surface”. In: *Nature Communications* 11(1), pp. 1–11.
- Moyano-Cambero et al. (2017). *Physico-chemical properties of chondritic meteorites. Clues on the origin and evolution of their parent bodies*. Universitat Autònoma de Barcelona.
- NASA (2021). *Meteorite Classification Chart*. <https://curator.jsc.nasa.gov/education/classification.cfm>, Last accessed on the 2021-10-25.
- Ogliore et al. (2012). “Incorporation of a late-forming chondrule into Comet Wild 2”. In: *The Astrophysical Journal Letters* 745(2), p. L19.
- Opeil, GJ Consolmagno, and DT Britt (2010). “The thermal conductivity of meteorites: New measurements and analysis”. In: *Icarus* 208(1), pp. 449–454.
- Opeil et al. (2020). “The surprising thermal properties of CM carbonaceous chondrites”. In: *Meteoritics & Planetary Science* 55(8).

- Popova et al. (2011). “Very low strengths of interplanetary meteoroids and small asteroids”. In: *Meteoritics & Planetary Science* 46(10), pp. 1525–1550.
- Schmus, Van and Wood (1967). “A chemical-petrologic classification for the chondritic meteorites”. In: *Geochimica et Cosmochimica Acta* 31(5), pp. 747–765.
- Scott and Krot (2003). “Chondrites and their components”. In: *TrGeo* 1, p. 711.
- Stamati et al. (2020). “Spam: software for practical analysis of materials”. In: *Journal of Open Source Software* 5(51), p. 2286.
- Taylor (2011). “Wet, Carbonaceous Asteroids: Altering Minerals, Changing Amino Acids”. In: *Planetary Science Research Discoveries Report*, p. 154.
- Tsuchiyama et al. (2008). “Strength measurements of carbonaceous chondrites and cosmic dust analogs using micro compression testing machine”. In: *Japan Geosciences Union Meeting, Abstracts of Papers*.
- Ursul and Ursul (2019). “From planetary to space mining: prospects for sustainable development”. In: *MATEC Web of Conferences*. Vol. 265. EDP Sciences, p. 06015.
- Walsh (2018). “Rubble pile asteroids”. In: *Annual Review of Astronomy and Astrophysics* 56, pp. 593–624.
- Weidenschilling (1993). “Protostars and Planets III”. In: *Formation of Planetesimals in the solar nebula* 1031.
- Williams and Cieza (2011). “Protoplanetary disks and their evolution”. In: *Annual Review of Astronomy and Astrophysics* 49, pp. 67–117.
- Woolfson (2000). *The origin and evolution of the solar system*. CRC Press.
- Yamada et al. (2016). “Timescale of asteroid resurfacing by regolith convection resulting from the impact-induced global seismic shaking”. In: *Icarus* 272, pp. 165–177.
- Yin and Dai (2021). “Petrology and mineralogy of the Viñales meteorite, the latest fall in Cuba”. In: *Science Progress* 104(2), p. 00368504211019859.
- Zolensky and McSween Jr (1988). “Aqueous alteration, Meteorites and the Early Solar System JF Kerridge, MS Matthews, 114–143, Univ. of Ariz”. In: *Press, Tucson*.




# Appendices

---


## 4.1 Appendix to Chapter 2

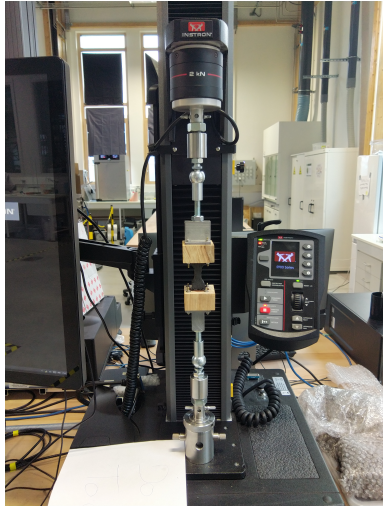
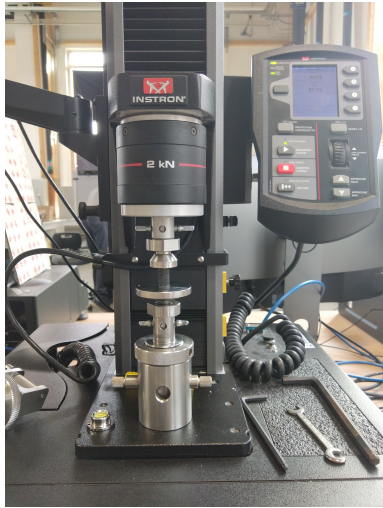
### 4.1.1 Drawing of the different molds used

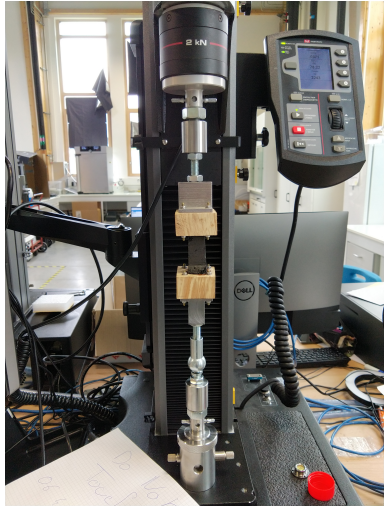
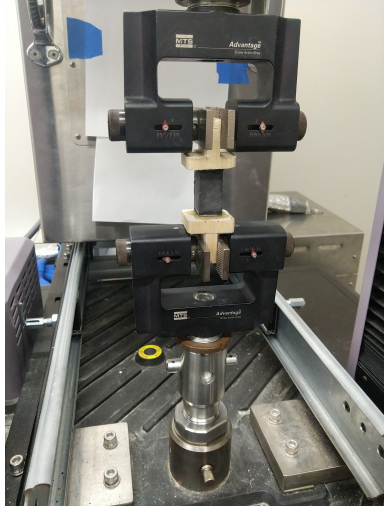
### 4.1.2 History of the various tests carried out


Test n°	Image	Description	Observations
1		The sample is placed directly on the tensile jaws	Breakage when clamping the sample
2		The sample is rectangular. it is stuck on a piece of wood on each side. These pieces of wood are then connected to a steel cable which is taken directly in the traction jaws. in order to know the Young's modulus, photos are taken using a fast camera throughout the test to carry out an image correlation.	The deformations are too weak to be detected by the camera (deformation below the size of the pixel). Modulus of elasticity not found, impossibility of compression, tensile rupture close to glue, results difficult to interpret.



<p>3</p>		<p>The sample is rectangular. It is glued to a piece of wood on each side. These pieces of wood are then bolted to a set of metal parts to make a rigid link with the traction machine.</p>	<p>The sample breaks when bolting the wood/sample assembly into the machine</p>
<p>4</p>	<p>Same as test n°3</p>	<p>The system remains the same as before. This time, the sample is glued directly into the machine, which monopolizes the machine for 24 hours for each test.</p>	<p>The results seem to vary depending on the degree of prestressing induced by the drying of the glue.</p>
<p>5</p>	<p>Same as test n°3</p>	<p>The same system is reused, with the same type of sample. This time, a compression of 1N is imposed throughout the drying of the glue. Traction/-compression cycles are carried out.</p>	<p>These tests make it possible to determine the Young's modulus of the material. The Tensile strength, on the other hand, is difficult to assess because of the rupture close to the bonded surface.</p>

6		The same test method is used, this time with samples having a thinner center section.	These tests make it possible to determine the tensile strength
7	Same as test n°3	Performing the same tests with samples at 50% porosity	Obtaining the tensile strength modulus of elasticity
8		Compression tests between two plates	Poor sample/compression platters interface

<p>9</p>		<p>Compression tests using the same system as during the tensile tests</p>	<p>Determination of compression modulus and compression strength</p>
<p>10</p>		<p>The samples are glued to pieces of wood on each side. These pieces of wood are then placed in the traction jaws</p>	<p>The sample breaks when tightening the jaws</p>

11		<p>The ends of the samples are sealed in a box filled with epoxy. the alignment of these boxes is guaranteed by two interlocking pieces on each side connecting them. These parts, in addition to guaranteeing alignment, make it possible to manipulate the assembly without inducing force in the sample. this therefore makes it possible to attach the assembly in the machine without breaking the sample. Once the assembly is attached, the two parts are detached and the tests can begin.</p>	<p>The blocking of the boxes during the drying of the epoxy causes the same problems as in test number 4.</p>
12	Same as test n°10	<p>Two pieces of wood are taken directly from the jaws of the machine. The sample is then glued directly in the machine with a constant compression of 1N.</p>	<p>Obtaining compression strength values</p>

## 4.2 Appendix to Chapter 3

### 4.2.1 Thermal simulation parameters

In order to calculate the temperature variations on the surface of Near Earth Asteroids (NEA). The script below was used. You must first download and install the Thermophysical and thermal models codes present on the site: <https://www-n.oica.eu/delbo/>. In our case, the asteroid 101955 Bennu was taken as an example.

The script requires the use of a 3-dimensional model of the asteroid, Bennu.obj, which can be found on the site <https://www.asteroidmission.org/updated-bennu-shape-model-3d-files/>. ephBennu.txt is the file containing the ephemeris of the asteroid studied, which is its position over time. Then come the physical characteristics. In order, the emissivity, the thermal inertia, the albedo, the semi aperture angle of the craters and the crater surface density. In our case, these last two factors have been neglected.

```
1 echo Bennu_Radar.obj ephBennu.txt 0.9 350 0.045 0 0 | runtpm
```

### 4.2.2 SPAM code and parameters

The script presented below was used in a spam environment in a terminal. It allows to perform a digital image correlation from two images. In the case of the study carried out, these are 3D images obtained by X-ray tomography. This script requires the installation of the SPAM calculation code as described on their website <https://ttk.gricad-pages.univ-grenoble-alpes.fr/spam/installation.html>. The output files are indicated as an indication in the comments.

```
1 spam-ereg /path/to/my/data/im1-bin2.tif /path/to/my/data/im2-bin2.tif
2 # OUTPUT: im1-bin2-im2-bin2-PhiEye.tsv
3
4 spam-reg /path/to/my/data/im1.tif /path/to/my/data/im2.tif -pf im1-im2-PhiEye.
   tsv -pfb 2 -def
5 # OUTPUT: im1-im2-Registration.tsv
6 # OUTPUT: im1-def.tif
```

```
7
8 spam-ldic /path/to/my/data/im1.tif /path/to/my/data/im2.tif -pf im1-im2-PhiEye.
   tsv -ns 20 -hws 20 -glt 9000 -tif
9   # OUTPUT: im1-im2-ldic.tsv
10  # OUTPUT: im1-im2-DeltaPhiNorm.tif
11  # OUTPUT: im1-im2-error.tif
12  # OUTPUT: im1-im2-iterations.tif
13  # OUTPUT: im1-im2-returnStatus.tif
14  # OUTPUT: im1-im2-Xdisp.tif
15  # OUTPUT: im1-im2-Ydisp.tif
16  # OUTPUT: im1-im2-Zdisp.tif
17
18 spam-regularStrain /path/to/my/data/m1-im2-ldic.tsv -cub -comp vol dev U e -tif
19  # OUTPUT: im1-im2-ldic-strain-Q8.tsv
20  # OUTPUT: im1-im2-ldic-vol-Q8.tif
21  # OUTPUT: im1-im2-ldic-dev-Q8.tif
22  # OUTPUT: im1-im2-ldic-Uxx-Q8.tif
23  # OUTPUT: im1-im2-ldic-Uyx-Q8.tif
24  # OUTPUT: im1-im2-ldic-Uyy-Q8.tif
25  # OUTPUT: im1-im2-ldic-Uzx-Q8.tif
26  # OUTPUT: im1-im2-ldic-Uzy-Q8.tif
27  # OUTPUT: im1-im2-ldic-Uzz-Q8.tif
28  # OUTPUT: im1-im2-ldic-exx-Q8.tif
29  # OUTPUT: im1-im2-ldic-eyx-Q8.tif
30  # OUTPUT: im1-im2-ldic-eyy-Q8.tif
31  # OUTPUT: im1-im2-ldic-ezx-Q8.tif
32  # OUTPUT: im1-im2-ldic-ezy-Q8.tif
33  # OUTPUT: im1-im2-ldic-ezz-Q8.tif
34
35 spam-deformalImage /path/to/my/data/im1.tif -pf im1-im2-ldic.tsv
36  # OUTPUT: im1-def.tif
```

**Effect of thermal cycling on the regolith formation.** S.Cohoner<sup>1</sup>, D.Britt<sup>2</sup>, B.Harthong<sup>1</sup>, A.DiDonna<sup>1</sup> and R.Peyroux<sup>1</sup>

<sup>1</sup>Univ. Grenoble Alpes (CNRS, Grenoble INP, 3SR, F-38000 Grenoble, France), <sup>2</sup>University of Central Florida (4000 Central Florida Blvd., Orlando FL 32816, USA)

The Hayabusa2 space mission recently returned asteroid regolith samples from the carbonaceous asteroid 162173 Ryugu to Earth. Other samples from the asteroid 101955 Bennu which is also a carbonaceous asteroid are on their way to Earth with the OSIRIS-REx mission. Micrometeorite bombardment [1–3] and thermal cracking [4–7] are thought to be the two main processes responsible for the formation of regolith.

In this study we focus on the formation of regolith due to thermal fracturing. Surface temperature can vary significantly during day/night cycles. In fact, the temperature variation of a type C near earth asteroid (NEA) is of the order of 200K [4]. An analogue to carbonaceous meteorites with a CM-like composition, following the preliminary compositional results for 101955 Bennu and 162173 Ryugu was developed in collaboration with the University of Central Florida (UCF) and Deep Space Industries (DSI) [8]. It is now produced by UCF's Exolith Lab will be used to investigate this phenomena.

Water and sodium metasilicate were added to the simulant to act as a binder to form blocks with strength properties similar to CM meteorites. Glass beads of 400–600 $\mu$ m were added to simulate chondrite inclusions (chondrules, CAIs). A wire saw was used to machine the samples into the appropriate experimental shape. The experiment consists in subjecting the samples to thermal cycles and regularly scan them with X-ray tomography in order to follow the thermal induced crack propagation. We chose a cylindrical shape to have a temperature propagation as homogeneous as possible. The size of the sample has been chosen to be big enough to be a representative volume element and as small as possible to reduce the time of the thermal cycles (11mm of diameter and 20mm height).

The samples were subjected to temperature variations of  $\Delta T=200$ K. To do so, liquid nitrogen was used to cool down the sample to 77K while the ambient temperature will warm it up. In order to avoid the formation of frost on the sample, which would deteriorate it, the sample was put inside a thin copper tube. In order to fill the empty space between the wall of the tube and the sample and avoid the thermal barrier of the air, aluminum foil was used to wrap the sample and ensure thermal contact between the copper tube and the simulant. This set up protected the sample against the ambient humidity without significantly extending the time required for the thermal cycling. To assure the hermeti-

city, the tube has been made long enough for the cap to be always outside the liquid nitrogen tank.

Numerical simulations were run to assess the time needed to perform one cycle. Even though these simulations did not take into account all physical phenomena such as the evaporation of the liquid nitrogen in contact with the sample, the results are in agreement with those of the preliminary tests. Sensors linked with an Arduino card were used automatically track the thermal cycles and a Python interface enabled us to see the evolution of the temperature of inside the tube in real time.

X-ray tomography scans have been performed at the initial state and after different amount of cycles in order to follow the formation and the propagation of cracks inside the material. The images were then processed using SPAM, a Python numerical code developed by the 3SR laboratory in Grenoble, France [9].

The first results show the appearance of cracks from the first 70 cycles. These cracks occur in areas close to the sample surface and are localized around inclusions. During the first 140 cycles, there are detachments of inclusion on the surface as well as the propagation of certain large voids which can go as far as opening on the surface (See in Figure 1). After 270 cycles, the propagation of the cracks significantly damaged the material, making it weaker, which led to the rupture of the lower part of our sample (See in Figure 2).

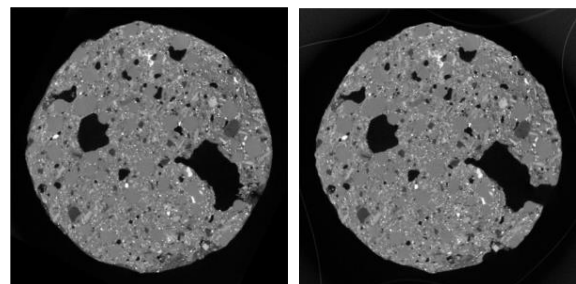


Figure 1 : X-ray tomography image of the sample at the initial state (on the left) and after 140 cycles.(on the right)

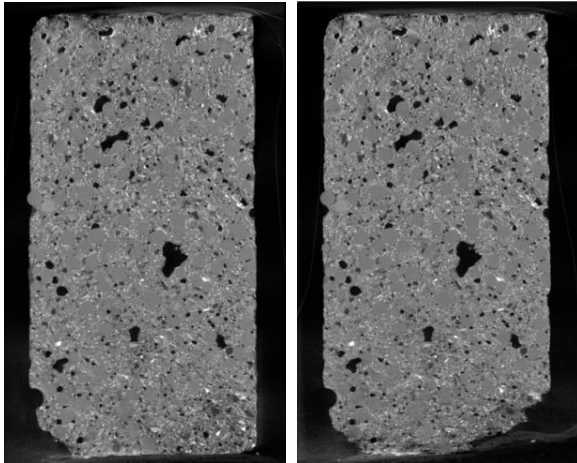


Figure 2 : X-ray tomography image of the sample at the initial state (on the left) and after 400 cycles.(on the right)

#### References:

- [1] J. D. Hogan, C. El Mir, J. B. Plescia, and K. Ramesh, (2015), *Dynamic brittle fragmentation: probing the byproducts of hypervelocity impact in space*, *Procedia Engineering* 103, 205–212.
- [2] T. M. Yamada, K. Ando, T. Morota, and H. Katsuragi, (2016), “*Timescale of asteroid resurfacing by regolith convection resulting from the impact-induced global seismic shaking*”, *Icarus* 272, 165–177.
- [3] C. Avdellidou, C. Schultz, M. Price, M. Cole, A. DiDonna, B. Harthong, M. Delbo, D. Britt, and R. Peyroux, (2019), “*Mechanical properties of very weak carbonaceous asteroid analogues and response to hypervelocity impacts.*”, *Icarus*.
- [4] M. Delbo, G. Libourel, J. Wilkerson, N. Murdoch, P. Michel, K. Ramesh, C. Ganino, C. Verati, and S. Marchi, (2014), “*Thermal fatigue as the origin of regolith on small asteroids*”, *Nature* 508, 233–236.
- [5] K. Hazeli, C. El Mir, S. Papanikolaou, M. Delbo, and K. Ramesh, (2018), “*The origins of asteroidal rock disaggregation: interplay of thermal fatigue and microstructure*”, *Icarus* 304, 172–182.
- [6] C. El Mir, K. Ramesh, and M. Delbo, (2019), “*The efficiency of thermal fatigue in regolith generation on small airless bodies*”, *Icarus* 333, 356–370.
- [7] J. Molaro, K. Walsh, E. Jawin, R.-L. Ballouz, C. Bennett, D. DellaGiustina, D. Golish, C. D. d’Aubigny, B. Rizk, S. Schwartz, et al., (2020), “*In situ evidence of thermally induced rock breakdown widespread on bennu’s surface*”, *Nature Communications* 11, 1–11.
- [8] D. T. Britt, K. M. Cannon, K. Donaldson Hanna, J. Hogancamp, O. Poch, P. Beck, D. Martin, J. Escrig, L. Bonal, and P. T. Metzger, (2019), “*Simulated asteroid materials based on carbonaceous chon-*

*drite mineralogies*”, *Meteoritics & Planetary Science* 54, 2067–2082.



### 4.3 Abstract

The OSIRIS-REx space mission from the NASA recently returned asteroid regolith samples from the carbonaceous asteroid Bennu to Earth. Micrometeorite bombardment (Hogan et al., 2015; Yamada et al., 2016; Avdellidou et al., 2019a) and thermal cracking (Delbo et al., 2014; Hazeli et al., 2018; Mir et al., 2019; Molaro et al., 2020) are the two main processes responsible for the formation of regolith on the surface of asteroids. The materials that constitute most of the near-Earth asteroids are believed to be very weak, common in space but almost nonexistent on earth (Walsh, 2018; Grott et al., 2019; Popova et al., 2011). In this study we focus on the mechanical characterization and the study of fracturing by thermal cycling of this material. An analogue to carbonaceous meteorites with a CM-like composition, following the preliminary compositional results for Bennu and Ryugu developed in collaboration with the University of Central Florida (UCF) and Deep Space Industries (DSI) (Britt et al., 2019) and is now produced by UCF's Exolith Lab will be used to investigate this phenomena. Water and sodium metasilicate were added to the simulant to act like a binder and form blocks as well as glass beads of 400-600 $\mu$ m to simulate chondrite inclusions (chondrules, CAIs). Then a wire saw has been used to machine the samples for both mechanical tests and for thermal cycling. Tensile and compression tests were performed on different samples to in order to determine the modulus of elasticity of 1GPa and the tensile strength of 250kPa. For the thermal cycling, we chose to make them have a cylindrical shape to have a temperature propagation as homogeneous as possible. The size of the sample has been chosen to be big enough to be considered as a representative volume element and as small as possible to reduce the time of the thermal cycles (11mm of diameter and 20mm height). We chose the temperatures to have a  $\Delta T=200$ K. To do so, liquid nitrogen has been chosen to cool down the sample at 77K while the ambient temperature will warm it up. X-ray tomography scans have been performed at the initial state and after different amount of cycles in order to follow the formation and the propagation of cracks inside the material. The images were then processed using SPAM, which is a numerical code on Python developed by the 3SR laboratory in Grenoble

in France. The results show the appearance of cracks from the first 70 cycles. These cracks occur in areas close to the sample surface and are localized around inclusions. During the first 140 cycles, there are detachments of inclusion on the surface as well as the propagation of certain large voids which can go as far as opening on the surface. After 270 cycles, the propagation of the cracks significantly damaged the material, making it weaker, which led to the rupture of the lower part of our sample.